PROBING GRAVITY ON DISPARATE SCALES

A DISSERTATION
SUBMITTED TO THE DEPARTMENT OF PHYSICS
AND THE COMMITTEE ON GRADUATE STUDIES
OF STANFORD UNIVERSITY
IN PARTIAL FULFILLMENT OF THE REQUIREMENTS
FOR THE DEGREE OF
DOCTOR OF PHILOSOPHY

Mustafa Abdulkader Amin
September 2008

I certify that I have read this dissertation and that, in my opinion, it is fully adequate in scope and quality as a dissertation for the degree of Doctor of Philosophy.

(Roger D. Blandford) Principal Adviser

I certify that I have read this dissertation and that, in my opinion, it is fully adequate in scope and quality as a dissertation for the degree of Doctor of Philosophy.

(Robert V. Wagoner)

I certify that I have read this dissertation and that, in my opinion, it is fully adequate in scope and quality as a dissertation for the degree of Doctor of Philosophy.

(Steven W. Allen)

I certify that I have read this dissertation and that, in my opinion, it is fully adequate in scope and quality as a dissertation for the degree of Doctor of Philosophy.

(Shamit S. Kachru)

Approved for the University Committee on Graduate Studies.

Abstract

This thesis is about probing gravity on cosmological and astrophysical scales. It also includes a discussion of an indirect probe of dark matter. It is a collection of projects that are fairly independent. However, gravitational physics plays an important role in each one of them.

In the first half of the thesis, we concentrate on cosmological scales. We provide a kinematic prescription for constraining the accelerated expansion of space. Then, as a more detailed investigation into the cause of this accelerated expansion, we provide a scale-dependent framework for probing the dynamics of gravitational and matter perturbations on linear, sub-horizon scales.

In the second half, we move to smaller, astrophysical scales. This half includes two independent projects. First, we investigate the effects of relativistic dark matter on the dark matter density profile and the self-annihilation flux from the Galactic center. Second, we propose the existence of quasi-stationary, spiral density patterns in accretion discs around black holes.

Preface

Our understanding of gravitation has come a long way since the proverbial apple fell close to Newton. From Newton's force laws to a description of gravity in terms of spacetime curvature, our understanding of gravity has repeatedly challenged our view of the cosmos. We have moved on from pondering the perfect shapes of planetary orbits to questions about the past, present and future dynamics of the entire universe. That we have a theory, Einstein's general relativity (GR), that allows us to sensibly ask these questions is remarkable.

Within GR, spacetime becomes a malleable, swirling, fluttering entity with all forms of energy democratically controlling and responding to its variations. Based on the Principle of Equivalence, GR, with its geometric description of gravity is both powerful and elegant. Yet, it is this very description that puts it at odds with what we currently understand of the the rest of fundamental physics. The strong, weak and electromagnetic interactions take place in the arena of spacetime. Gravity is this arena itself. All known fundamental interactions find a description and a (likely) unification in terms of quantum fields. Gravity, as yet, does not. With our current understanding, besides gravity, none of the interactions care about the absolute energy scales in the problem. This difference is leading us to another paradigm shift in our view of the physical world.

Our understanding of gravity has led us to triumphant solutions of long-standing problems in the weak-field limit ($GM/Lc^2 \sim 10^{-5}$, where M and L are the characteristic mass and length scales and G is Newtons gravitational constant). The perihelion shift of Mercury was one such solution. It has also led to some unnerving predictions, such as the existence of black holes in the strong field limit. It has enabled us to weigh the universe without seeing it, leading us to infer the existence of large amounts of dark matter on astrophysical and cosmological scales. Viewing our universe on the grandest of scales, GR is providing us a glimpse into the nature of nothingness.

In the weak-field limit, GR has been tested against a wealth of observations on solar system scales. However, it is more poorly constrained on astrophysical and cosmological scales. This thesis is about probing gravity on cosmological and astrophysical scales. It also includes a discussion of a probe into the nature of dark matter. It is a collection of projects which are fairly independent; however, gravitational physics plays an important role in each one of them. The two chapters following the Introduction (Chapter 1) are about probing gravity on cosmological scales. Chapter 2 deals with the background, homogeneous universe. It provides a kinematic prescription for constraining the expansion history of the universe. Chapter 3 provides a framework for probing the relationship between the cosmological metric and matter fluctuations. In Chapters 4 and 5, we leave the realm of cosmology and move to more astrophysical phenomenon. In Chapter 4, we investigate the effects of relativistic dark matter at the Galactic center on the density profile of dark matter and the self-annihilation flux. In Chapter 5, we propose the existence of quasi-stationary spiral density patterns in accretion discs around black holes.

The bulk of the thesis (each chapter) is composed of already published (or accepted for publication) work. The published papers were written in collaboration with various co-authors. None of the papers would have been possible without their guidance, insight, effort and enthusiasm. In addition to these papers, I have added a number of appendices at the end of each chapter. These are not yet published. Some serve a pedagogical purpose, some provide a collection of results that might be of future use, and some provide a concentrated effort in a particular direction that would have otherwise taken us too far from the main body of the chapter. They do, however, form an integral part of this thesis.

Acknowledgments

It is my pleasure to acknowledge the unwavering support and encouragement of my advisor, Prof. Roger Blandford. In spite of his busy schedule, he always had time to listen to my ideas, share his own and provide guidance at every stage of my graduate career. It is difficult not to enjoy learning in his presence. Along with Roger, Prof. Bob Wagoner has been my teacher and mentor. I have yet to walk out of his office feeling disappointed. Without their enthusiasm, patience and persistence, this thesis would not have been possible.

A large fraction of this thesis consists of projects undertaken in collaboration with the faculty, postdoctoral fellows and graduate students at Stanford. In this respect, I would like to thank Roger, Bob, Prof. Steve Allen, David Rapetti, Prof. Andrei Frolov, Phil Marshall, Edward Baltz and Tommer Wizansky. From the conception of ideas, through the meandering ups and downs of research, to publication, working with them has been a exciting, humbling and fun.

Most of what I have learned has come from everyday interactions with my fellow graduate students. Navin Sivanandam has been a sounding board for almost every idea I have had. I have benefited immensely from his ability to give a concrete form to many of my often fuzzy notions. For most questions I asked, David Starr had inevitably thought more about it than I had. His thoroughness has been inspirational. It was an absolute pleasure to learn and collaborate with Tommer Wizansky on everything, from grading homework sets to working on research projects. Without John Conley's help, I would have barely survived my first year of graduate school. With many discussions over coffee, Matt Pyle has provided his own unique insights into problems, which have helped in solidifying my understanding. My taste (or lack

thereof) in movies has been heavily influenced by Ryan Lampe, and without Paul Oreto, I would never have appreciated a bird's eye view of the Monterey Bay. Daniel Green and Surjeet Rajendran were the go to people for getting a high energy physics perspective, and especially with Surjeet, good Indian food buffets. I have enjoyed many conversations, research and otherwise, with My Phuong Le, Prajwal Kulkarni, Jeremy Verkaik, Yorgos Sofianatos, Eugene Motayama, Tim Larson, Joey Sulpizio, Jamie Gainer, Ann Erickson and Naoko Kurahashi.

From the astrophysics group, I would like to thank a close friend and colleague, Steve Healey for careful reading and editing of most of my written work. Also, without his distractions, every day in the office would have been bleak. I appreciate the friendship and patience of Chen Zheng, Eric Morganson and Jane Dai, my fellow graduate students under Roger. Having entered the field of astrophysics with almost no background knowledge, a number of students have helped me along the way. I have used and abused Matt Turk's wizardry with all things computational. Fen Zhao, Ji-Hoon Kim, Ed Wu, Peng Wang, Heidi Wu, Kyle Watters, Conrad Hutcheson, Mike Shaw, Paul Simeon and Douglas Applegate have all been wonderful friends and colleagues. I would especially like to thank my current office mates, Adam Mantz and Evan Million, for their patience and help on many a problem. My previous office mates, Michael Dorris and Yanwei Jiang, also have my gratitude for the same reasons.

A number of postdoctoral fellows have played an integral part in my education at Stanford. Apart from my collaborators, I would like to thank Marusa Bradac, Steven Fuerst, Teddy Cheung, Anja Von Linden, Mark Allen, Michael Busha and Brian Gerke for many fruitful conversations about research and ins and outs of academia.

Starting with the moment I submitted my application to the Stanford until this date, the administrative staff from the Department of Physics at Stanford, the Stanford Linear Accelerator Center (SLAC) and the Kavli Institute of Particle Astrophysics and Cosmology (KIPAC) have been helpful in every way possible. I wish to thank Ziba Mahdavi, Martha Siegal, Jennifer Formicelli, Elva Carbajal, and especially Christine Aguilar and Maria Frank for their wonderful support.

I very much appreciated the financial support provided by a Stanford Graduate Fellowship (SGF) for the last two years of my graduate career. Part of the final

organization of this thesis was done at the Astro-Particle and Cosmology (APC) Institute in Paris, France. I thank them for their gracious hospitality.

My decision to pursue a career in academia has been heavily influenced by some incredible teachers. I want to thank my teachers back home in India, at the University of Texas at Arlington (UTA) and here at Stanford. From my undergraduate years at the UTA, I wish to especially thank professors Kaushik De, Zdislaw Museilak and Barbara Shipman, who, more often than not, went out of their way to facilitate my education and research experience. Of my teachers back home, Murtaza Chasmai has my special gratitude. I also want to thank my close friend, Rishiraj Pravahan, without whom I would probably not have pursued a career in physics. To my friends at UTA and back home, thank you for making my life richer than I could have ever imagined.

From my family, I want to thank Saifee Mamu for helping me come to the United States. Ammi Maasi and Shabbit Khalu have my gratitude for their gracious hospitality and support during my undergraduate years. Lastly, dear Zainy Maasi, Mummy, Daddy and Bhai: without your support and sacrifices, my education and this thesis would never have been possible. Thank you.

For all my teachers

Contents

Abstract **v**

Preface **vii**

Acknowledgments **ix**

xiii

1 Introduction **1**

1.1 Probing gravity on cosmological scales 1

1.2 Relativistic dark matter at the Galactic center 5

1.3 Probing strong field gravity on astrophysical scales 7

Bibliography 1 11

2 A kinematical approach to dark energy studies **15**

2.1 Introduction 16

2.2 The kinematical and dynamical frameworks for late time cosmic acceleration 19

2.2.1 Previous work 19

2.2.2 A new kinematical framework 22

2.2.3 Standard dynamical framework 24

2.3 Evolving jerk models 24

2.4 Data and analysis methods 26

2.4.1 Type Ia supernovae data 26

2.4.2 X-ray cluster data 28

2.4.3 Markov Chain Monte Carlo analysis 30

2.4.4 Hypothesis testing in the kinematical analysis: how many model parameters are required? 30

2.5 Results 34

2.5.1 Comparison of constant jerk and constant w models 34

2.5.2 More complicated kinematical models 36

2.5.3 Comparison of distance measurements 37

2.5.4 Comparison with Riess et al. (2004) 37

2.6 The distance to the last-scattering surface 37

2.7 Conclusions 42

2.A Analysis in the kinematic plane 46

2.B Cosmology with a constant ratio 51

2.C Cosmokinematics 55

2.C.1 Introduction 55

2.C.2 Kinematic flows 56

2.C.3 Step-kinematics 60

2.C.4 Reconstruction 62

Bibliography 2 65

3 A framework for probing gravity on cosmological scales 75

3.1 Introduction 77

3.2 Our ansatz and associated assumptions 82

3.3 Application of the framework with examples 90

3.3.1 General relativity with cold dark matter and the cosmological constant 91

3.3.2 Scalar-tensor theory with cold dark matter (matter representation) 93

3.3.3 General relativity with cold dark matter and quintessence . . 97

3.3.4 $f(R)$ gravity with cold dark matter 98

3.3.5 Brane world models: DGP Gravity 100

3.4 Observational implications 105
3.5 Discussion 108
3.6 Acknowledgments 109
3.A Aspects of cosmological perturbation theory 110
  3.A.1 Gauge transformations and invariance 110
  3.A.2 Classifying perturbations 114
  3.A.3 Scalar metric perturbations 115
  3.A.4 Newtonian gauge: useful formulae 117
3.B Braneworld perturbations 121
  3.B.1 Braneworld electrostatics: An analogy 121
  3.B.2 Braneworld perturbations: Details 123
Bibliography 3 137

4 Relativistic dark matter at the Galactic center 145
4.1 Introduction 146
4.2 Supersymmetric dark matter 147
4.3 Astrophysics 150
  4.3.1 Density profile 151
  4.3.2 Annihilation flux 154
4.4 Discussion 155
Bibliography 4 159

5 Persistent geometric patterns in accretion discs 163
5.1 Introduction 164
5.2 Accretion disk kinematics 165
5.3 Persistent patterns in the disk 167
5.4 Discussion 170
Bibliography 5 175

List of Tables

2.1 A statistical comparison of the goodness of fit of different kinematic models. 31
2.2 A statistical comparison of the goodness of fit of the constant j and constant w models 34

List of Figures

2.1 68.3 and 95.4 per cent confidence limits in the (q_0,j) and the (Ω_{m},w) plane using three data sets: SNIa data sets (Riess et al. 2004; Astier et al. 2005) and the cluster f_{gas} data of Allen et al. (2006) 32

2.2 The 68.3 and 95.4 per cent confidence variations about the median values for $j(a)$ as a function of the scale factor a, over the range where we have data (0.36,1). 38

2.3 The 68.3 and 95.4 per cent confidence limits on the offset in distance as a function of scale factor, relative to the reference ΛCDM cosmology, for both the kinematical (constant j) and dynamical (constant w) analyses. 39

2.4 The 68.3 and 95.4 per cent confidence limits in the (q_0,dq/dz) plane obtained using the SNIa data from the first year of the SNLS (Astier et al. 2005), the 'gold' sample of Riess et al. (2004) , the cluster f_{gas} data of Allen et al. (2006) and the combination of all three data sets. 40

2.5 1σ and 2σ constraints on $j(a)$ over the range (including the distance to the last scattering surface) of the data (0.0009,1). 43

2.6 Physical boundaries in the $q_0 - j$ plane. 48

2.7 Qualitative behavior of $a(t)$ using the effective potential 50

2.8 Distance measurements with clusters of galaxies 51

2.9 Expansion history of the universe in the qj plane. 59

2.10 The "step-like" evolution of kinematic variables as a function of scale factor a for a spatially flat universe with radiation, matter and a cosmological constant. 61

3.1 The ratio of out expansion parameter (aH/k), as a function of a from last scattering to the present for the concordance model. 87
3.2 The dimensionless coefficient functions characterizing the relationship between the metric perturbations and matter distribution for ΛCDM and the scalar-tensor theory. 95
3.3 The dimensionless coefficient functions characterizing growth of structure for ΛCDM and the scalar-tensor theory. 96
3.4 The dimensionless coefficient functions characterizing the relationship between the metric perturbations and matter distribution for ΛCDM and DGP braneworld model. 102
3.5 The dimensionless coefficient functions characterizing growth of structure for ΛCDM and DGP braneworld model 103

4.1 A typical set of Feynman diagrams contributing to the self annihilations of a neutralino into Standard Model particles. 148
4.2 The annihilation cross-section σv as a function of (v/c) for sample models from the $\tilde{\tau}$ coannihilation region. 149
4.3 (a) The variation of the core radius with $(\sigma v)_0$ and $(\sigma v)_1$. (b) Spike profile for $\gamma_c = 1 - 1.5$. 153
4.4 (a) The annihilation flux as a function of $(\sigma v)_0$ and $(\sigma v)_1$. (b) The ratio of annihilation fluxes Φ/Φ_0 where '0' refers to the flux calculated by setting $(\sigma v)_1 = 0$. 155
4.5 Annihilation flux as a function of slope profile γ_c. 156

5.1 Orbital frequency Ω, radial epicyclic frequency κ, and precession frequency $\omega = \Omega - 2\kappa$ of a 2:1 orbit in an accretion disk around a Kerr black hole with $M = 10\,M_\odot$ and $a = 1/2$. 166
5.2 Sample closed orbits. 1:2 orbit corresponds to 2 epicycles per 1 rotation around a central body, while 2:1 orbit corresponds to 1 epicycle per 2 rotations. 167
5.3 Evolution of density patterns obtained by distributing particles on stacked 1:2 and 2:1 orbits 168

5.4 Persistent pattern frequencies of three lowest-order radial modes (2:1, 3:1, and 3:2) for a $10M_\odot$-mass black hole as a function of black hole spin parameter a. 171
5.5 Persistent pattern frequencies of three lowest-order transverse modes (2:1, 3:1, and 3:2) for a $10M_\odot$-mass black hole as a function of black hole spin parameter a. 171

Chapter 1

Introduction

This introduction is meant to provide context, motivation and a brief historical background for the chapters to follow. A more detailed introduction to the ideas relevant for the chapters, including a survey of related works in the literature can be found at the beginning of each chapter. Below, we provide a combined introduction for Chapters 2 and 3 and individual ones for Chapters 4 and 5.

1.1 Probing gravity on cosmological scales

Modern cosmology began in 1915 with Einstein's general theory of relativity [1]. Within general relativity, it became possible to address the questions of the dynamics of the entire universe and its dependence on the universe's constituents. From 1915 to 1929, Friedmann, Lemaître, Einstein, de Sitter (amongst others) all played their part in cosmological model building. The cosmological constant was introduced, discarded and reintroduced.[1] Models that were static, collapsing, expanding, bouncing and

---

[1] Einstein introduced it for two reasons. First, based on Mach's ideas, Einstein considered it an unwanted characteristic that his field equations should admit a solution without matter. He (erroneously) believed that his field equations with a cosmological constant would not admit a solution without matter. The second reason was the desire to have a static universe (consistent with observations at the time). After Einsteins initial introduction of the cosmological constant, it was reintroduced for different reasons by other cosmologists. Lemaître, investigated the effects of the cosmological constant on the expansion history [2]. He even suggested its connections to vacuum energy [3]. Eddington, strongly supported its inclusion on grounds that it represented a necessary length scale for cosmology. Initial measurements of the contemporary rate of expansion

accelerating were proposed and investigated. With Hubble's characterization of the distance-redshift relation of receding nebulae in 1929 [5], an expanding universe came to be accepted. Yet the detailed description of the expansion history would have to wait more than six decades. Open, closed, and flat universes were all possible. Our understanding of the various components that make up our universe was shaky at best. As early as 1933, based on the large velocity dispersion in clusters, Fritz Zwicky had pointed at the missing mass problem [6]. Assuming a universe that started in a hot, dense and singular state (the big bang), big bang nucleosynthesis (BBN) was able to correctly predict relative abundances of the light elements in our universe [7, 8]. However, it was not until the cosmic microwave background (CMB) was measured by Penzias and Wilson [9] that we gave up on the notion of a steady state universe where matter was constantly regenerated. This was the status of cosmology before the 1980s.

Today, we are in a rather different position. In the last two decades cosmology has undergone a revolution. The journey from a speculative science to an observationally driven field has been nothing short of spectacular. With the discovery of the cosmic microwave background, a universe with a hot, dense and homogeneous past has come to be accepted. We have not only measured an almost perfect black-body spectrum of this radiation but have mapped out fluctuations in its temperature at the level of one part in 10^5 [10, 26]. The contemporary expansion rate has been measured to a few percent level accuracy [3].

Despite this incredible progress, the last two decades have also brought forth some unexpected challenges. The uniformity of the cosmic microwave background has led to questions about acausal correlations in the sky (the horizon problem). We need a mechanism for explaining the almost scale-invariant fluctuations in the cosmic microwave background. Observations of the rotation curves of galaxies, the temperature of the gas in galaxy clusters, the galaxy velocities in clusters and gravitational lensing are forcing us to introduce a new, non-standard model component (dark matter) that interacts with the rest of the universe mainly through its gravity. In addition, the

---

of the universe pointed towards a universe that was younger than the stars in it. The cosmological constant also helped in alleviating this problem. A more detailed historical account can be found in [4].

observed amount of structure in our universe requires dark matter to aid gravitational instability. Finally, there is the unexpected discovery (1998) that the expansion of our universe is accelerating [2, 1].

From a theoretical perspective, the above challenges have been addressed with varying levels of success. The inflationary paradigm [15] that arose in the 1980s out of a desire to solve the monopole problem, ended up providing an explanation for the horizon problem, explained spatial flatness and also provided a mechanism for generating (almost) scale invariant density fluctuations. Despite its success, connecting the cause of inflation to the rest of particle physics has yet to be fully accomplished. The requirement of a non-baryonic component is satisfied by WIMPs (weakly interacting massive particles) arising naturally in super-symmetric (SUSY) extensions of the standard model (see [16] for a review). One should keep in mind though, that we have yet to detect any SUSY particles. Finally, cosmic acceleration can be explained by once again introducing a cosmological constant into the Einstein field equations, but its connection to particle physics is far from clear (see [18] for a review).

The inflationary paradigm for the very early universe and a contemporary universe dominated by dark matter and cosmological constant has become the standard model of cosmology. It is consistent with all observational data. However, one should also bear in mind that none of these components (inflaton, dark matter, and cosmological constant) has been probed by non-gravitational means. Given the profound implications of this standard cosmological model, one should be cautious in claiming it as a unique physical description of our universe. It is natural to consider whether alternatives to the standard model could explain the observations equally well.

At the present, no alternatives provide a significant advantage over the standard model (which we will refer to as ΛCDM from now on and concentrate on late times, $z \lesssim 1000$). In particular, all attempts at removing dark matter from the standard model have met with very limited success. Usually, additional clustering fields need to be reintroduced, which essentially introduce dark matter. Thus, for the purpose of this thesis, we will assume the existence of dark matter. For explaining cosmic acceleration, a number of alternatives to the cosmological constant (for example, quintessence, extra dimensions, etc.) have been proposed. A few words of caution regarding these alternatives are in order. None of the models that try to explain cosmic acceleration are “better” than the cosmological constant in the sense that they all need a fine tuned parameter (a Hubble length scale) and usually introduce additional complications. Nevertheless, in our view, the benefit of studying models beyond the standard model is that they teach us a lot about why GR with a cosmological constant is special. These models and their respective phenomenology allow us to gain an insight into the solution space of theories (and their consequences) close to ΛCDM. They help us understand the features that are specific to the standard cosmological model, thus allowing us to concentrate our experiments and observational efforts to look for departures from these features.

The difficulty of coming up with a good alternative to ΛCDM should not deter us from testing this standard model of cosmology. To do this one can take two approaches. The first is to assume that ΛCDM with GR is correct and simply compare the consequences with observations. However, this approach cannot tell us anything about the uniqueness of ΛCDM as a physical model for our universe. To gain confidence in ΛCDM, one must explore the solution space around this model. For this purpose, a parameterized approach is beneficial. A parameterized approach (the Parameterized Post-Newtonian framework or PPN framework in short) was undertaken to explore the solution space around GR on solar system scales over the last century. The PPN framework began with Eddington in 1922 but was restricted to the vacuum spacetime around a spherically symmetric central body. Its current version is mainly due to Nordtvedt and Will (see [15, 19] for a more detailed history). The essential idea is to start with Newtonian gravity and include relativistic effects in a systematic manner. The metric is constructed out of moments of stresses, densities, etc, systematically arranged as an expansion in v/c and the gravitational potential Φ/c^2. The relativistic contributions are preceded by coefficients that can be calculated for any given theory. Within certain physical limitations on its applicability, the PPN framework includes ten PPN coefficients which can be used to test GR and rule out alternatives (see [15]).

A similar theoretical framework that will allow for a classification of the existing and upcoming models is required on cosmological scales. Such a framework should allow us to zero in on the common and distinguishing features of different models. It should also provide a common language for theorists to compare and contrast the observational consequences of different models. On the observational front, it should allow for a smarter choice of observational projects that are best suited to reveal departures from the standard or are able to eliminate a large class of alternatives. The provision of such a framework is the goal of the first part of this thesis. We leave the detailed introduction to our framework and a review of the current literature on this subject to the introduction provided at the beginning of Chapters 2 and 3.

1.2 Relativistic dark matter at the Galactic center

In 1933, based on the high velocity dispersion in galaxy clusters, Fritz Zwicky started our quest for some unseen matter that made its presence felt through its gravitational effects. Its existence on the scale of galaxies was first suggested by the high velocities of stars and gas in the outskirts of the Andromeda galaxy (1939) [20]. Four decades later, Rubin and Ford obtained similar results (with much improved observations) for a number of galaxies [21]. On the theoretical front, in 1973, Ostriker and Peebles argued that a halo of dark matter was necessary for the stability of disc galaxies [22]. Although astronomers were convinced that the missing matter was present in cosmologically significant amounts, whether it was baryonic matter, black holes or an indication of physics beyond the standard model was unclear. The idea of cold dark matter, as it is used in the modern cosmological context, can be credited R. Bond (1983) [23].

It is difficult to overstate the importance of dark matter in our contemporary view of the cosmos. It provides the missing matter that aids gravitational instability, it explains the depth of the gravitational potential wells in galaxy clusters, and it also explains the rotation curves of galaxies. Today, detailed observations of the power spectrum of CMB fluctuations and the distribution of galaxies and gravitational lensing measurements are all consistent with the cold dark matter paradigm. Merging clusters (for example, the Bullet cluster [24]) with physically separated mass and light concentrations provide, arguably, the most striking blow to models without dark matter. From a particle physics perspective, it provides strong evidence for physics beyond the standard model. It could perhaps be the most striking evidence for supersymmetry. Given its importance, it is imperative that we probe dark matter though all possible means.

Probing dark matter through its gravitational interactions is now a mature field. For the purposes of structure formation, galaxy clusters, lensing and galaxy rotation curves, all that is required is that dark matter is reasonably massive, that it clumps gravitationally and that it is otherwise weakly interacting. Consequently, it is difficult to obtain detailed information about interaction cross sections, masses, etc. from these observations (unless one goes to small enough scales where the free streaming becomes important). However, when one starts looking at the total dark matter abundance, its possible decay channels, its (non-gravitational) self-interaction and interactions with baryons a more detailed picture emerges.

Experiments that probe the nature of dark matter particles beyond their gravitational interactions can be divided roughly into two classes: direct and indirect detection experiments. Direct detection experiments like Cryogenic Dark Matter Search (CDMS) [25] essentially measure the recoil energy from the interaction of the incoming dark matter particle and the nucleus of a chosen target material. The measured recoil energy provides a strong constraint on the cross section and a weaker one on the mass of the particle. The Large Hadron Collider (LHC) [26] will provide a controlled way of probing the properties of dark matter. However, in the case of the LHC, it will be difficult to be certain whether the new particles produced are the dark matter candidates required by astrophysical observations.

The idea behind indirect detection is to look for the annihilation (or decay) products of dark matter. Since the rate of such annihilations is dependent on the number density, it is best to look for regions where the density of dark matter particles is expected to be high. Apart from the early universe, such high density regions are expected to arise naturally in the centre of dark matter haloes, its clumpy substructure and in the vicinity of compact objects. The earliest ideas on indirect detection of dark matter surfaced in the early 1980s. Since then, a number of experiments have turned their eyes towards the heavens in search of the ashes of dark matter particles. At the time of this writing, the latest of such efforts, the Gamma-ray Large Area Space Telescope (*GLAST*), is about to launch [1].

Most of the signal of dark matter annihilation is expected to come from our Galactic center. There is strong evidence that gravitational dynamics in the subparsec region at our galactic center is governed by a $\sim 10^6$ solar mass black hole [16]. It is plausible that the vicinity of the black hole contains a large density of dark matter particles moving at sub-relativistic velocities. Could these sub-relativistic velocities have an effect on the expected annihilation signal? In Chapter 5, we discuss a new relativistic effect on the self annihilation cross section of dark matter particles, that might be relevant for future indirect detection experiments. Although the presence of a black hole plays an important role in our problem, this part of the thesis is not about probing strong field gravity. This part is about the observational consequences of dark matter particles moving at relativistic velocities near the black hole at our Galactic center. We investigate how the annihilation cross section, density profile and annihilation signal of dark matter near our Galactic center are influenced by the presence of the central black hole.

1.3 Probing strong field gravity on astrophysical scales

Compared to weak-field gravity, strong-field gravity is far less constrained by observations. Yet it is in this regime where the most dramatic departures from Newtonian gravity occur. Apart from cosmology, the vicinities of black holes and neutron stars are the only other laboratories for probing strong-field gravity. There are a number of reasons for the dearth of constraints in this regime, the obvious one being that the masses and length scales required are impossible to achieve in terrestrial laboratories. Typically, probing the vicinities of black holes and neutron stars is difficult due to the small sizes of these systems and/or their large distances from us. Moreover, such regions are rarely devoid of matter, whose often complicated fluid dynamics and electromagnetic interactions makes the extraction of information about gravitational aspects a tall order.

Currently, some of the best tests for gravity come from binary pulsars. By measuring the advance in the periastron, time dilation and rate of change of the orbital period, stringent constrains on gravity can be obtained [29]. Other tests include the use of electromagnetic signatures from matter accreting in the vicinity of the compact objects. In some cases, black hole horizons or the last stable orbit can leave unique signatures in these observations (see for example [16]). A careful study of the relativistic broadening of the iron lines from these regions also yields a (limited) map of the distorted space-time close to the horizon (see for example [16]). Another exciting and puzzling class of astrophysical objects that have a potential for probing strong-field gravity is the so-called quasi-periodic oscillators (QPOs), particularly in the high frequency (40-450 Hz) regime. When observed in X-rays, their time variability is quasi-periodic. Remarkably, in a number of black hole systems, the time variability contains two characteristic frequencies with an almost constant ratio of 3:2 (see, for example, the review article [1]).

Our initial motivation for the work presented in Chapter 5 was providing a dynamical mechanism to explain the remarkably stable ratio (3:2) of frequencies associated with these QPOs. Our idea is similar to that of density waves, which was put forth as an explanation of the spiral structure of galaxies. The crucial requirement for the existence of these density waves is a non-Keplerian potential. Such potentials are present in galaxies due to the disc-like distribution of matter whereas in the vicinity of black-holes they arise due to the relativistic corrections to Newtonian gravity.

In our investigation, we find that a remarkably persistent (~ 50 orbital periods), counter-rotating geometric pattern exists in thin cold accretion discs at a radius of $r \sim 10 r_g$ with a width of $\Delta r \sim 4 r_g$ ($r_g \equiv GM/c^2$). A single disc can support more than one such pattern, each with its own characteristic frequency. Although the excitation mechanism is unknown, once excited, these patterns can persist for a long time. We do not provide any mechanism to convert these density patterns into X-rays, but there is the tantalizing possibility of a connection of the frequencies of the longest-lived patterns with those seen in QPOs.

Given the likely complexity of the magneto-fluid dynamics and emission mechanism for X-rays, our work is far from providing a complete physical description. Nevertheless, it provides a starting point, and perhaps a motivation, for more detailed numerical investigations.

The mechanism we suggest depends crucially on the general relativistic corrections to the orbital motion of the particles. If the central object is a black hole, the frequency associated with this rotating pattern depends on the black hole spin and mass. It scales inversely with mass and increases with spin. Thus, in principle, these patterns can be used to probe gravity in the strong field regime.

Bibliography 1

[1] A. Einstein. Die Feldgleichungen der Gravitation. *Sitzungsberichte der Königlich Preußischen Akademie der Wissenschaften (Berlin), Seite 844-847.*, pages 844–847, 1915.

[2] G. Lemaître. Expansion of the universe, A homogeneous universe of constant mass and increasing radius accounting for the radial velocity of extra-galactic nebulae. *MNRAS*, 91:483–490, March 1931.

[3] G. Lemaître. Evolution of the Expanding Universe. *Proceedings of the National Academy of Science*, 20:12–17, January 1934.

[4] H. Bondi. *Cosmology.* Cambridge [Eng.] University Press, 1952., 1952.

[5] E. Hubble. A Relation between Distance and Radial Velocity among Extra-Galactic Nebulae. *Proceedings of the National Academy of Science*, 15:168–173, March 1929.

[6] F. Zwicky. Die Rotverschiebung von extragalaktischen Nebeln. *Helvetica Physica Acta*, 6:110–127, 1933.

[7] R. A. Alpher, H. Bethe, and G. Gamow. The origin of chemical elements. *Phys. Rev.*, 73(7):803–804, Apr 1948.

[8] R. V. Wagoner, W. A. Fowler, and F. Hoyle. On the Synthesis of Elements at Very High Temperatures. *ApJ*, 148:3–+, April 1967.

[9] A. A. Penzias and R. W. Wilson. A Measurement of Excess Antenna Temperature at 4080 Mc/s. *ApJ*, 142:419–421, July 1965.

[10] G. F. Smoot, C. L. Bennett, A. Kogut, E. L. Wright, J. Aymon, N. W. Boggess, E. S. Cheng, G. de Amici, S. Gulkis, M. G. Hauser, G. Hinshaw, P. D. Jackson, M. Janssen, E. Kaita, T. Kelsall, P. Keegstra, C. Lineweaver, K. Loewenstein, P. Lubin, J. Mather, S. S. Meyer, S. H. Moseley, T. Murdock, L. Rokke, R. F. Silverberg, L. Tenorio, R. Weiss, and D. T. Wilkinson. Structure in the COBE differential microwave radiometer first-year maps. *ApJ Lett.*, 396:L1–L5, September 1992.

[11] D. N. Spergel et al. Wilkinson microwave anisotropy probe (wmap) three year results: Implications for cosmology. *Astrophys. J. Suppl.*, 170:377, 2007.

[12] W. L. Freedman et al. Final results from the hubble space telescope key project to measure the hubble constant. *Astrophys. J.*, 553:47–72, 2001.

[13] S. Perlmutter et al. Measurements of omega and lambda from 42 high-redshift supernovae. *Astrophys. J.*, 517:565–586, 1999.

[14] Adam G. Riess et al. Observational evidence from supernovae for an accelerating universe and a cosmological constant. *Astron. J.*, 116:1009–1038, 1998.

[15] A. H. Guth. Inflationary universe: A possible solution to the horizon and flatness problems. *Phys. Rev.D*, 23:347–356, January 1981.

[16] Gianfranco Bertone, Dan Hooper, and Joseph Silk. Particle dark matter: Evidence, candidates and constraints. *Phys. Rept.*, 405:279–390, 2005.

[17] Sean M. Carroll. The cosmological constant. *Living Rev. Rel.*, 4:1, 2001.

[18] Clifford M. Will. The confrontation between general relativity and experiment. *Living Reviews in Relativity*, 4(4), 2001.

[19] C.M. Will. *Theory and experiment in gravitational physics*. Cambridge University Press, Cambridge, U.K.; New York, U.S.A., 2nd edition, 1993.

[20] H. W. Babcock. The rotation of the Andromeda Nebula. *Lick Observatory Bulletin*, 19:41–51, 1939.

[21] V. C. Rubin and W. K. J. Ford. Rotation of the Andromeda Nebula from a Spectroscopic Survey of Emission Regions. *ApJ*, 159:379–+, February 1970.

[22] J. P. Ostriker and P. J. E. Peebles. A Numerical Study of the Stability of Flattened Galaxies: or, can Cold Galaxies Survive? *ApJ*, 186:467–480, December 1973.

[23] J. R. Bond, J. Centrella, A. S. Szalay, and J. R. Wilson. Dark matter and shocked pancakes. In J. Audouze and J. Tran Thanh van, editors, *NATO ASIC Proc. 117: Formation and Evolution of Galaxies and Large Structures in the Universe*, pages 87–99, 1984.

[24] D. Clowe, M. Bradač, A. H. Gonzalez, M. Markevitch, S. W. Randall, C. Jones, and D. Zaritsky. A Direct Empirical Proof of the Existence of Dark Matter. *ApJ Lett.*, 648:L109–L113, September 2006.

[25] CDMS Collaboration. A Search for WIMPs with the First Five-Tower Data from CDMS. *ArXiv e-prints*, 802, February 2008.

[26] *http://lhc.web.cern.ch/lhc/*, 2007.

[27] *http: // www-glast.stanford.edu/*, 2007.

[28] R. Schodel et al. Stellar dynamics in the central arcsecond of our galaxy. *Astrophys. J.*, 596:1015–1034, 2003.

[29] I. H. Stairs. Testing General Relativity with Pulsar Timing. *Living Reviews in Relativity*, 6:5–+, September 2003.

[30] A. T. Okazaki, S. Kato, and J. Fukue. Global trapped oscillations of relativistic accretion disks. *Publ. Astron. Soc. Japan*, 39:457–473, 1987.

[31] J. E. McClintock and R. A. Remillard. Black Hole Binaries. *ArXiv Astrophysics e-prints*, June 2003.

Chapter 2

A kinematical approach to dark energy studies

David Rapetti, Steve Allen, Mustafa A. Amin, Roger Blandford

KIPAC/Department of Physics, Stanford University, CA 94305, USA

Mon. Not. Roy. Astron. Soc., 375:1510-1520, 2007 [arXiv:0708.1793v2].

Abstract We present and employ a new kinematical approach to cosmological 'dark energy' studies. We construct models in terms of the dimensionless second and third derivatives of the scale factor $a(t)$ with respect to cosmic time t, namely the present-day value of the deceleration parameter q_0 and the cosmic jerk parameter, $j(t)$. An elegant feature of this parameterization is that all ΛCDM models have $j(t) = 1$ (constant), which facilitates simple tests for departures from the ΛCDM paradigm. Applying our model to the three best available sets of redshift-independent distance measurements, from type Ia supernovae and X-ray cluster gas mass fraction measurements, we obtain clear statistical evidence for a late time transition from a decelerating to an accelerating phase. For a flat model with constant jerk, $j(t) = j$, we measure $q_0 = -0.81 \pm 0.14$ and $j = 2.16^{+0.81}_{-0.75}$, results that are consistent with ΛCDM at about the 1σ confidence level. A standard 'dynamical' analysis of the same data, employing the Friedmann equations and modeling the dark energy as a fluid with an equation of state parameter, w (constant), gives $\Omega_{\rm m} = 0.306^{+0.042}_{-0.040}$ and $w = -1.15^{+0.14}_{-0.18}$, also consistent with ΛCDM at about the 1σ level. In comparison to dynamical analyses, the kinematical approach uses a different model set and employs a minimum of prior information, being independent of any particular

gravity theory. The results obtained with this new approach therefore provide important additional information and we argue that both kinematical and dynamical techniques should be employed in future dark energy studies, where possible. Our results provide further interesting support for the concordance ΛCDM paradigm.

Note

In this paper, my main contribution was in the theoretical aspects of the kinematic formalism (based on [1]). The appendices at the end of this chapter are new, and were not included in the published paper.

2.1 Introduction

The field of cosmology has made unprecedented progress during the past decade. This has largely been driven by new observations, including precise measurements of the spectrum of cosmic microwave background (CMB) anisotropies([2, 3] and references therein), the distance-redshift relation to type Ia supernovae [4, 5, 6, 7, 8], the distance-redshift relation to X-ray galaxy clusters [9, 10, 11], measurements of the mean matter density and amplitude of matter fluctuations from X-ray clusters [12, 13, 14, 15, 16], measurements of the matter power spectrum from galaxy redshift surveys [17, 18, 19], Lyman-α forest studies [20, 21, 22] and weak lensing surveys [23, 24, 25, 26], and measurements of the Integrated Sachs-Wolfe effect [27, 28].

These and other experiments have lead to the definition of the so-called concordance ΛCDM cosmology. In this model, the Universe is geometrically flat with only $\sim$4 per cent of the current mass-energy budget consisting of normal baryonic matter. Approximately 23 per cent is cold dark matter, which interacts only weakly with normal baryonic matter but which clusters under the action of gravity. The remaining $\sim$ 73 per cent consists of smoothly distributed quantum vacuum energy (the cosmological constant), which pushes the Universe apart. This combination of matter and vacuum energy leads to the expectation that the Universe should undergo a late time transition from a decelerating to an accelerating phase of expansion. Late-time acceleration of the Universe is now an observed fact [7, 10, 8]. A transition from a decelerating phase to a late-time accelerating phase is required to explain both these late-time acceleration measurements and the observed growth of structure.

Despite the observational success of the concordance ΛCDM model, significant fine tuning problems exist. In particular, difficulties arise in adjusting the density of the vacuum energy to be a non-zero but tiny number, when compared with the value predicted by standard theoretical calculations, and with explaining why the current matter and vacuum energy densities are so similar (the 'cosmic coincidence' problem). For these reasons, amongst others, a large number of alternative cosmological models have been proposed. These include models that introduce new energy components to the Universe - so called 'dark energy' models e.g. scalar 'quintessence' fields [29, 30, 31, 32, 33], K-essence [34, 35, 36], tachyon fields [37, 38] and Chaplygin gas models [39, 40]. Other possibilities include modified gravity theories, motivated by e.g. the existence of extra dimensions [41, 42, 43, 44, 45] or other modifications of General Relativity [46, 47, 48, 49, 50, 51, 52], which can also lead to late-time cosmic acceleration. The simplicity of the concordance ΛCDM model, however, makes it highly attractive. A central goal of modern observational cosmology is to test whether this model continues to provide an adequate description of rapidly improving data.

Most current analyses of cosmological data assume General Relativity and employ the mean matter density of the Universe, $\Omega_{\rm m}$, and the dark energy equation of state w as model parameters. Such analyses are often referred to as 'dynamical studies', employing as they do the Friedmann equations. Other dynamical analyses employ modified Friedmann equations for a particular gravity model. However, a purely kinematical approach is also possible that does not assume any particular gravity theory. Kinematical models provide important, complementary information when seeking to understand the origin of the observed late-time accelerated expansion.

In a pioneering study, [7] measured a transition from a decelerating to accelerating phase using a simple linear parameterization of the deceleration parameter $q(z)$, where $q(z)$ is the dimensionless second derivative of the scale factor, $a(t)$, with respect to cosmic time. Recently, [53], [54] and [55] have employed a variety of other parameterizations, constructed in terms of $q(z)$, to study this transition. However, since the underlying physics of the transition are unknown, the choice of a particular parameterization for $q(z)$ is quite arbitrary. [53] applied a principal component analysis of $q(z)$ to the supernovae data of [7] and found strong evidence for recent, changing acceleration but weak evidence for a decelerated phase in the past (i.e. weak evidence for a transition between the two phases). [55] employed a Bayesian analysis to the [7] data and the more recent SNLS supernovae sample of [8], obtaining a similar result.

In this paper we develop an improved method for studying the kinematical history of the Universe. Instead of using parameterizations constructed in terms of $q(z)$, we follow [1] and introduce the cosmic jerk, $j(a)$, the dimensionless third derivative of the scale factor with respect to cosmic time. (Here a is the cosmic scale factor, with $a = 1/1 + z$.) The use of the cosmic jerk formalism provides a more natural parameter space for kinematical studies. Our results are presented in terms of current deceleration parameter q_0 and $j(a)$, where the latter can be either constant or evolving. We apply our method to the three best current kinematical data sets: the'gold' sample of type Ia supernovae (hereafter SNIa) measurements of [7], the SNIa data from the first year of the Supernova Legacy Survey (SNLS) project [8], and the X-ray galaxy cluster distance measurements of [56]. This latter data set is derived from measurements of the baryonic mass fraction in the largest relaxed galaxy clusters, which is assumed to be a standard quantity for such systems [10].

In General Relativity $j(a)$ depends in a non-trivial way on both $\Omega_{\rm m}$ and $w(a)$ [1]. In general, there is no one-to-one mapping between models with constant j and models with constant w. A powerful feature of the standard dynamical approach is that all ΛCDM models have $w = -1$ which make it easy to search for departures from ΛCDM. Likewise, the use of the jerk formalism imbues the kinematical analysis with a similar important feature in that all ΛCDM models are represented by a single value of $j = 1$. The use of the jerk formalism thus enables us to constrain and explore departures from ΛCDM in the kinematical framework in an equally effective manner. Moreover, by employing both the dynamical and kinematical approaches to the analysis of a single data set, we explore a wider set of questions than with a single approach. We note that [57] and [58] also drew attention to the importance of the jerk parameter for discriminating models of dark energy and/or modified gravity. [59] and [60] also showed its relevance for probing the spatial curvature of the Universe.

Using the three kinematical data sets mentioned above, we find clear evidence for a negative value of q_0 (current acceleration) and a positive cosmic jerk, assuming j constant. The concordance ΛCDM model provides a reasonable description of the data, using both the new kinematical and standard dynamical approaches. We also search for more complicated deviations from ΛCDM, allowing $j(a)$ to evolve as the Universe expands, in an analogous manner to dynamical studies which allow from time-variation of the dark energy equation of state $w(a)$. Our analysis employs a Chebyshev polynomial expansion and a Markov Chain Monte Carlo approach to explore parameter spaces. We find no evidence for a time-varying jerk.

This paper is structured as follows: in section 2.2 we describe our new kinematical approach. In section 2.3 we describe the scheme adopted for polynomial expansions of $j(a)$. Section 2.4 includes details of the data analysis. The results from the application of our method to the supernovae and X-ray cluster data are presented in section 2.5. Finally, our main conclusions are summarized in section 2.7. Throughout this paper, we assume that the Universe is geometrically flat.

2.2 The kinematical and dynamical frameworks for late time cosmic acceleration

2.2.1 Previous work

The expansion rate of the Universe can be written in terms of the Hubble parameter, $H = \dot{a}/a$, where a is the scale factor and $\dot{a}$ is its first derivative with respect to time. The current value of the Hubble parameter is the Hubble Constant, usually written as H_0. Under the action of gravity, and for negligible vacuum energy, the expansion of the Universe is expected to decelerate at late times. Contrary to this expectation, in the late 1990s, type Ia supernovae experiments [4, 5] provided the first direct evidence for a late time accelerated expansion of the Universe. In particular, the present value of the deceleration parameter, q_0, measured from the supernova data was found to be negative. In detail, the deceleration parameter q is defined as the dimensionless second derivative of the scale factor

$$q(t) = -\frac{1}{H^2}\left(\frac{\ddot{a}}{a}\right) , \tag{2.1}$$

and in terms of the scale factor,

$$q(a) = -\frac{1}{H}(aH)' \tag{2.2}$$

where the 'dots' and 'primes' denote derivatives with respect to cosmic time and scale factor, respectively.

The current 'concordance' cosmological model, ΛCDM, has been successful in explaining the SNIa results and all other precision cosmology measurements to date. Together with it's theoretical simplicity, this makes the ΛCDM model very attractive. However, as discussed in the introduction, the concordance model does face significant theoretical challenges and a wide-range of other possible models also provide adequate descriptions of the current data (see for an extensive review [61]).

An excellent way to distinguish between models is to obtain precise measurements of the time evolution of the expansion of the Universe. Given such data, a number of different analysis approaches are possible. In searching for time evolution in the deceleration parameter, as measured by current SNIa data, [7] assumed a linear parameterization of $q(z)$,

$$q(z) = q_0 + \frac{dq}{dz}z. \tag{2.3}$$

These authors measured a change in sign of the deceleration parameter, from postive to negative approaching the present day, at a redshift $z_{\rm t} = 0.46 \pm 0.13$. Using this parameterization for $q(z)$, the definition of the deceleration parameter given by equation (2.1), and integrating over the redshift, we obtain that for this model the evolution of the Hubble parameter is given in the form

$$E(z) = H(z)/H_0 = (1+z)^{(1+q_0-q')} e^{q'z}, \tag{2.4}$$

where $q' = dq/dz$.

However, since the origin of cosmic acceleration is unknown, it is important to recognize that the choice of any particular parameterized expansion for $q(z)$ is essentially arbitrary. Indeed, when (or if) a transition between decelerated and accelerated phases if inferred to occur can depend on the parameterization used. [55] showed that using the linear parameterization described by equation (2.3) and fitting to the SNIa data set of [8] a transition redshift $z_{\rm t} \sim 2.0$ is obtained which, uncomfortably, lies beyond the range of the data used.

Transitions between phases of different cosmic acceleration are more naturally described by models incorporating a cosmic 'jerk'. The jerk parameter, $j(a)$, is defined as the dimensionless third derivative of the scale factor with respect to cosmic time [1]

$$j(t) = \frac{1}{H^3}\left(\frac{\dddot{a}}{a}\right), \tag{2.5}$$

and in terms of the scale factor

$$j(a) = \frac{(a^2H^2)''}{2H^2} \tag{2.6}$$

where again the 'dots' and 'primes' denote derivatives with respect to cosmic time and scale factor, respectively.

In such models, a transition from a decelerating phase at early times to an accelerating phase at late times occurs for all models with $q_0 < 0$ and a positive cosmic jerk. Note that a Taylor expansion of the Hubble parameter around small redshifts [62, 7] contains the present value of both the deceleration and jerk parameters, q_0 and j_0. Such Taylor expansions are inappropriate for fitting high-redshift objects [1, 63], such as those included in the data sets used here.

[1] describe how the jerk parameterization provides a convenient, alternative method to describe models close to ΛCDM. In this parameterization, flat ΛCDM models have

a constant jerk with $j(a) = 1$ (note that this neglects the effects of radiation over the redshift range of interest, which is also usually the case when modeling within the dynamic framework). Thus, any deviation from $j = 1$ measures a departure from ΛCDM, just as deviations from $w = -1$ do in more standard dynamical analyses. Importantly, in comparison to dynamical approaches, however, the kinematical approach presented here both explores a different set of models and imposes fewer assumptions. The dynamical approach has other strengths, however, and can be applied to a wider range of data (e.g. CMB and growth of structure studies), making the kinematical and dynamical approaches highly complementary.

It is interesting to note that, in principle, any particular dynamical parameter space will have its own physical limits. For instance, within the dynamical $(\Omega_{\rm m}, w)$ plane, models with $w < -1$, known as 'phantom' dark energy models, violate the dominant energy condition [64, 65] and present serious problems relating to the treatment of dark energy perturbations [66, 67, 68, 69] when $w(z)$ crosses the boundary $w = -1$. Current data allow models with $w < -1$ [70, 7, 10, 8, 3, 71] and models in which $w(z)$ crosses the boundary $w = -1$ [72, 73, 22, 74, 75, 76]. However, another dynamical parameter space, coming e.g. from a different gravity theory, might not pathologically suffer from such boundaries around the models allowed for current data.

Since the (q_0, j) plane (see below) is purely kinematical, i.e. no particular gravity theory is assumed, we are not forced to interpret $j = 1$, or any locus in this plane, as a barrier. Note, however, that caution is required in extending the results from the kinematical analysis beyond the range of the observed data (for details see [77]). For example, inappropriately extending a jerk model to very high redshifts could imply an unphysical Hubble parameter at early times, i.e., these models do not have a Big Bang in the past.

2.2.2 A new kinematical framework

For our kinematical analysis, we first calculate $H(a)$ given $j(a; \mathcal{C})$ where $\mathcal{C} = (c_0, c_1, ..., c_{\rm N})$ is the selected vector of parameters used to describe the evolution of $j(a)$ (see below). Following [1] we rewrite the defining equation for the jerk parameter (2.6) in a more convenient form

$$a^2 V''(a) - 2j(a)V(a) = 0 \tag{2.7}$$

where $'$ denotes derivative with respect to a and $V(a)$ is defined as

$$V(a) = -\frac{a^2 H^2}{2H_0^2}\,. \tag{2.8}$$

We specify the two constants of integration required by (2.7) in terms of the present Hubble parameter H_0 and the present deceleration parameter q_0 as follows

$$V(1) = -\frac{1}{2}\,, \qquad V'(1) = q_0\,, \tag{2.9}$$

where $a(t_0) = 1$ at the present time t_0. Here the first condition comes from $H(1) = H_0$ and the second from

$$V'(1) = -\frac{H_0'}{H_0} - 1 = q_0\,. \tag{2.10}$$

The Hubble parameter, $H(a)$, obtained from equations (2.7), (2.8) and (2.9) is used to calculate the angular diameter (d_{A}) and luminosity (d_{L}) distances for a flat Friedmann-Robertson-Walker-Lemaître (FRWL) metric

$$d_{\mathrm{A}}(a) = a^2\, d_{\mathrm{L}}(a) = \frac{c}{H_0}\, a \int_a^1 \frac{1}{a^2 E(a)}\, da, \tag{2.11}$$

where c is the speed of light. These theoretical distances $d_{\mathrm{L}}(a)$ and $d_{\mathrm{A}}(a)$ are then used in the data analysis (see section 2.4).

Our framework provides a simple and intuitive approach for kinematical studies. For models with $q_0 < 0$ (> 0), the Universe is currently accelerating (decelerating). Models with $q_0 < 0$ and $j(a) = 1$ (constant) are currently accelerating and have the expansion evolving in a manner consistent with ΛCDM. Any significant departure from $j = 1$ indicates that some other mechanism is responsible for the acceleration.

2.2.3 Standard dynamical framework

For comparison purposes, we have also carried out a standard dynamical analysis of the data in which we employ a dark energy model with a constant dark energy equation of state, w. From energy conservation of the dark energy fluid and the Friedmann equation, we obtain the evolution of the Hubble parameter, $H(z) = H_0\,E(z)$,

$$E(z) = [\Omega_{\rm m}(1+z)^3 + (1-\Omega_{\rm m})(1+z)^{3(1+w)}]^{1/2}, \tag{2.12}$$

where $\Omega_{\rm m}$ is the mean matter density in units of the critical density. As with the kinematical analysis, we assume flatness and neglect the effects of radiation density. In this framework, models with a cosmological constant have $w = -1$ at all times.

2.3 Evolving jerk models

Our analysis allows for the possibility the cosmic jerk parameter, $j(a)$ may evolve with the scale factor. We have restricted our analysis to the range of a where we have data, $[a_{\rm min} = 0.36, a_{\rm max} = 1]$. In searching for possible evolution, our approach is to adopt ΛCDM as a base model and search for progressively more complicated deviations from this. We begin by allowing a constant deviation Δj from ΛCDM ($j = 1$). For this model, it is possible to solve the jerk equation (2.7) analytically. Using the initial conditions listed in (2.9), we obtain

$$V(a) = -\frac{\sqrt{a}}{2}\left[\left(\frac{p-u}{2p}\right)a^{p} + \left(\frac{p+u}{2p}\right)a^{-p}\right] \tag{2.13}$$

where $p \equiv (1/2)\sqrt{(1+8j)}$ and $u \equiv 2(q_0 + 1/4)$. Note that in the (q_0,j) plane for

$$j < \left\{ \begin{array}{ll} q_0 + 2q_0^2 & q_0 < -1/4 \\ -1/8 & q_0 > -1/4 \end{array} \right\} \tag{2.14}$$

there is no Big Bang in the past [1] The models allowed by our combined data sets do not cross this boundary.

---

[1] Allowed (q_0,j) values are those for which the equation $V(a) = 0$ has no solution in the past ($a < 1$) [77].

For the next most complicated possible deviation from ΛCDM, we have $j(a;\mathcal{C}) = j^{\Lambda\mathrm{CDM}} + \Delta j(a;\mathcal{C})$. Here $j^{\Lambda\mathrm{CDM}} = 1$ and $j(a;\mathcal{C})$ is the cosmic jerk for the cosmology in question. In order to meaningfully increase the number of parameters in the vector $\mathcal{C}$, we employ a framework constructed from Chebyshev polynomials. The Chebyshev polynomials form a basis set of polynomials that can be used to approximate a given function over the interval $[-1,1]$. We rescale this interval to locate our function $\Delta j(a;\mathcal{C})$ in the range of scale factor where we have data:

$$a_c \equiv \frac{a - (1/2)(a_{\min} + a_{\max})}{(1/2)(a_{\max} - a_{\min})}\,, \tag{2.15}$$

where a is the scale factor in the range of interest and a_{c} is Chebyshev variable. The trigonometric expression for a Chebyshev polynomial of degree n is given by

$$T_{\mathrm{n}}(a_{\mathrm{c}}) = \cos(n \arccos a_{\mathrm{c}}). \tag{2.16}$$

These polynomials can also be calculated using the recurrent formula

$$T_{\mathrm{n+1}}(a_{\mathrm{c}}) = 2a_{\mathrm{c}}T_{\mathrm{n}}(a_{\mathrm{c}}) - T_{\mathrm{n-1}}(a_{\mathrm{c}}), \qquad n \geq 1\,, \tag{2.17}$$

where $T_0(a_{\mathrm{c}}) = 1$ and, for example, the next three orders are $T_1(a_{\mathrm{c}}) = a_{\mathrm{c}}$, $T_2(a_{\mathrm{c}}) = 2{a_{\mathrm{c}}}^2 - 1$, $T_3(a_{\mathrm{c}}) = 4{a_{\mathrm{c}}}^3 - 3a_{\mathrm{c}}$, etc. Using a weighted combination of these components, any arbitrary function can be approximately reconstructed. The underlying deviation from ΛCDM can be expressed as

$$\Delta j(a;\mathcal{C}) \simeq \sum_{\mathrm{n}=0}^{\mathrm{N}} c_{\mathrm{n}} T_{\mathrm{n}}(a_{\mathrm{c}}) \tag{2.18}$$

where the weighting coefficients form our vector of parameters, $\mathcal{C} = (c_0, c_1, ..., c_{\mathrm{N}})$. Thus, using equation (2.18) we produce different parameterizations for increasing N. With higher N's we allow a more precise exploration of the $[q_0, j(a;\mathcal{C})]$ parameter space. However, it is clear that this process will be limited by the ability of the current data to distinguish between such models. In order to judge how many orders of polynomials to include, we quantify the improvements to the fits obtained from the inclusion of progressively higher orders in a variety of ways (see below). In general, we find that models with a degree of complexity beyond a constant jerk are not required by current data.

We note that approches other than expanding Δj in Chebyshev polynomials are possible, e.g. one could include the dimensionless fourth derivative of the scale factor as a model parameter. However, since ΛCDM does not make any special prediction for the value of this derivative, we prefer to use our general expansion in Δj here.

2.4 Data and analysis methods

2.4.1 Type Ia supernovae data

For the analysis of SNIa data, we use both the 'gold' sample of [7] and the first year SNLS sample of [8]. The former data set contains 157 [2] SNIa, where a subset of 37 low-redshift objects are in common with the data of [8]. [8] contains 115 [3] objects. We use the measurements of [8] for objects in common between the studies. Thus, combining both data sets we have 120 SNIa from the [7] gold sample (157 minus the 37 low-redshift objects in common) and 115 SNIa from [8].

The two SNIa studies use different light-curve fitting methods. In order to compare and combine the data, we fit the observed distance moduli $\mu^{\rm obs}(z_{\rm i}) = m^{\rm obs}(z_{\rm i}) - M$, where m is the apparent magnitude at maximum light after applying galactic extinction, K-correction and light curve width-luminosity corrections, and M is the absolute magnitude, with the theoretical predictions, $\mu^{\rm th}(z_{\rm i}) = m^{\rm th}(z_{\rm i}) - M = 5\log_{10} D_{\rm L}(z_{\rm i};\theta) + \mu_0$, where $D_{\rm L} = H_0\, d_{\rm L}$ is the H_0-free luminosity distance, $\mu_0 = 25 - 5log_{10}H_0$ and $m_0 \equiv M + \mu_0$ is a "nuisance parameter" which contains both the absolute magnitude and H_0.

For the $[q_0, j(a;\mathcal{C})]$ parameter space, the luminosity distance $d_{\rm L}(z;\theta)$ is directly obtained integrating the solution of the differential equation (2.7) with the definition (2.11) as presented in subsection 2.2.2. For models using linear parameterization

---

[2] [7] presented 16 new Hubble Space Telescope (HST) SNIa, combined with 170 previously reported SNIa from ground-based data. They identified a widely used "high-confidence" subset, usually referred to as the *gold sample*, which includes 14 HST SNIa.

[3] 71 SNLS objects, plus 44 previously reported nearby objects.

of $q(z)$ and/or dynamical models with Ω_m and w, we plug the equations (2.4) and (2.12), respectively, into the equation describing the luminosity distance for a flat FRWL metric, in units of megaparsecs

$$d_\mathrm{L}(z;\theta) = \frac{c(1+z)}{H_0}\int_0^z \frac{dz}{E(z;\theta)} \tag{2.19}$$

where the speed of light, c, is in km s^{-1} and the present Hubble parameter, H_0, in km(s Mpc)$^{-1}$. Here the vectors of parameters for each model are $\theta = (q_0, dq/dz)$ and $\theta = (\Omega_\mathrm{m}, w)$ respectively. For the gold sample data of [7], we use the extinction-corrected distance moduli, $\mu^\mathrm{obs}(z_\mathrm{i})$ and associated errors, σ_i^2. For the SNLS data of [8] we use the rest-frame-B-band magnitude at maximum light $m_\mathrm{B}^*(z_\mathrm{i})$, the stretch factor s_i and the rest-frame color c_i to obtain $\mu^\mathrm{obs}(z_\mathrm{i}) = m_\mathrm{B}^*(z_\mathrm{i}) - M + \alpha(s_\mathrm{i}-1) - \beta c_\mathrm{i}$. These values were derived from the light curves by [8], who also provide best-fitting values for $\alpha = 1.52 \pm 0.14$ and $\beta = 1.57 \pm 0.15$.

For both SNIa data sets, we have

$$\chi^2(\theta; m_0) = \sum_\mathrm{SNIa} \frac{[\mu^\mathrm{th}(z_\mathrm{i};\theta,\mu_0) - \mu^\mathrm{obs}(z_\mathrm{i};\theta,M)]^2}{\sigma_\mathrm{i}^2}, \tag{2.20}$$

where the dispersion associated with each data point, $\sigma_\mathrm{i}^2 = \sigma_{\mu_\mathrm{i,obs}}^2 + \sigma_\mathrm{int,i}^2 + \sigma_\mathrm{v,i}^2$. Here $\sigma_{\mu_\mathrm{i,obs}}^2$ accounts for flux uncertainties, $\sigma_\mathrm{int,i}^2$ accounts for intrinsic, systematic dispersion in SNIa absolute magnitudes and $\sigma_\mathrm{v,i}^2$ accounts for systematic scatter due to peculiar velocities. The SNLS analysis includes an intrinsic dispersion of 0.13104 magnitudes[4] and a peculiar velocity scatter of 300 km/s. The gold sample analysis includes 400 km/s peculiar velocity scatter, with an additional 2500 km/s added in quadrature for high redshift SNIa.

We marginalise analytically over m_0

$$\tilde{\chi}^2(\theta) = -2\ln\int_{-\infty}^{\infty} \exp\left(-\frac{1}{2}\chi^2(\theta, m_0)\right) dm_0 \tag{2.21}$$

obtaining

---

[4] http://snls.in2p3.fr/conf/papers/cosmo1/

$$\tilde{\chi}^2 = \ln\left(\frac{c}{2\pi}\right) + a - \frac{b^2}{c}, \tag{2.22}$$

where

$$a = \sum_{\mathrm{SNIa}} \frac{[5\log_{10} D_{\mathrm{L}}(z_{\mathrm{i}};\theta) - m^{\mathrm{obs}}(z_{\mathrm{i}})]^2}{\sigma_{\mathrm{i}}^2}, \tag{2.23}$$

$$b = \sum_{\mathrm{SNIa}} \frac{5\log_{10} D_{\mathrm{L}}(z_{\mathrm{i}};\theta) - m^{\mathrm{obs}}(z_{\mathrm{i}})}{\sigma_{\mathrm{i}}^2}, \qquad c = \sum_{\mathrm{SNIa}} \frac{1}{\sigma_{\mathrm{i}}^2}. \tag{2.24}$$

Note that the absolute value of $\chi^2 = a - (b^2/c)$. For the analysis in the standard dynamic framework, our results agree with those of [7] and [8], and the comparison work of [78].

2.4.2 X-ray cluster data

For the analysis of cluster X-ray gas mass fractions, we use the data of [56], which contains 41 X-ray luminous, relaxed galaxy clusters, including 26 previously studied [10]. [Some of the original 26 have since been revisited by the Chandra X-ray observatory leading to improved constraints (for details see [56]). The new X-ray data set spans a redshift interval $0.06 < z < 1.07$. Our analysis follows the method of [10], fitting the apparent redshift evolution of the cluster gas fraction with the expression

$$f_{\mathrm{gas}}^{\mathrm{ref}}(z_{\mathrm{i}}) = \mathcal{F}\, R^{\mathrm{ref}}(z_{\mathrm{i}}), \quad R^{\mathrm{ref}}(z_{\mathrm{i}}) \equiv \left[\frac{d_{\mathrm{A}}^{\mathrm{ref}}(z_{\mathrm{i}})}{D_{\mathrm{A}}(z_{\mathrm{i}})}\right]^{1.5}, \tag{2.25}$$

where $\mathcal{F} = (b\,\Omega_{\mathrm{b}} H_0^{1.5})/[(1+0.19\sqrt{h})\,\Omega_{\mathrm{m}}]$ is the normalization of the $f_{\mathrm{gas}}(z)$ curve, d_{A} and $d_{\mathrm{A}}^{\mathrm{ref}}(z)$ are the angular diameter distances ($d_A = d_L/(1+z)^2$) to the clusters for a given cosmology and for the reference ΛCDM cosmology (with $H_0 = 70$ km(s Mpc)$^{-1}$ and $\Omega_{\mathrm{m}} = 0.3$) respectively, and $D_{\mathrm{A}} = H_0\, d_{\mathrm{A}}$ is the H_0-free angular diameter distance. For the kinematical approach we treat the normalization $\mathcal{F}$ as a single 'nuisance' parameter, which we marginalize over in the MCMC chains.

For the *dynamical* analysis of the same X-ray data, we follow [10] and employ Gaussian priors on the present value of the Hubble parameter $H_0 = 72 \pm 8$ km(s

Mpc)$^{-1}$ [79], the mean baryon density $\Omega_{\rm b}h^2 = 0.0214 \pm 0.0020$ [80] and the X-ray bias factor $b = 0.824 \pm 0.089$ [determined from the hydrodynamical simulations of [81], including a 10 per cent allowance for systematic uncertainties]. The application of these priors leads to an additional constraint on $\Omega_{\rm m}$ from the normalization of the $f_{\rm gas}(z)$ curve. Since the kinematical approach does not constrain $\Omega_{\rm m}$, the kinematical analysis does not involve these priors and draws information only from the shape of the $f_{\rm gas}(z)$ curve. The dynamical analysis, in constrast, extracts information from both the shape *and* normalization.

2.4.3 Markov Chain Monte Carlo analysis

For both the kinematical and dynamical analyses, we sample the posterior probability distributions for all parameter spaces using a Markov Chain Monte Carlo (MCMC) technique. This provides a powerful tool for cosmological studies, allowing the exploration of large multi-dimensional parameter spaces. In detail, we use the Metropolis-Hastings algorithm implemented in the COSMOMC [5] code of [82] for the dynamic formalism, and a modified version of this code for the kinematic analysis.

Our analysis uses four MCMC chains for each combination of model and data. We ensure convergence by applying the Gelman-Rubin criterion [83], where the convergence is deemed acceptable if the ratio of the between-chain and mean-chain variances satisfies $R-1 < 0.1$. In general, our chains have $R-1 \ll 0.1$.

2.4.4 Hypothesis testing in the kinematical analysis: how many model parameters are required?

In the first case, we examined a kinematical model in which the deceleration parameter q_0 was included as the only interesting free parameter [see equation (2.4) with $q' = 0$]. This is hereafter referred to as the model $\mathcal{Q}$. As detailed in section 2.2, we next introduced the jerk parameter, j, as an additional free parameter, allowing it to take any constant value. We refer to this as model $\mathcal{J}$, which has the interesting free parameters, q_0 and j. Note that model $\mathcal{J}$ includes the set of possible ΛCDM models, which all have constant $j = 1$.

We next explored a series of models that allow for progressively more complicated deviations from ΛCDM. In each case, the improvement obtained with the introduction of additional model parameters, has been gauged from the MCMC chains using a variety of statistical tests. In the first case, we follow a frequentist approach and use the F-test, for which

$$F = \frac{\Delta\chi^2}{\chi^2_\nu\,\Delta m}, \tag{2.26}$$

---

[5] http://cosmologist.info/cosmomc/

Table 2.1: The marginalized median values and 68.3 per cent confidence intervals obtained analyzing each data set and all three data sets together. We show these results for two kinematical models: using only q_0 ($\mathcal{Q}$ model) and extending this parameter space with the jerk parameter j ($\mathcal{J}$ model). We quote χ^2 per degree of freedom for each model and three different statistical tests to quantify the significance of extending the parameter space from $\mathcal{Q}$ (q_0) to $\mathcal{J}$ (q_0,j). We quote the difference in $\Delta\chi^2_{\mathcal{JQ}}$, the probability given by F-test, the difference in the Bayesian Information Criterion (BIC) and $\ln B_{\mathcal{JQ}}$ (where $B_{\mathcal{JQ}}$ is the Bayes factor between the two models). Note that combining all three data sets we obtain a significant preference for the $\mathcal{J}$ model within all three tests.

	$\mathcal{Q}$ model		$\mathcal{J}$ model			Improvement			
Data set	q_0	$\chi^2_{\mathcal{Q}}/dof$	q_0	j	$\chi^2_{\mathcal{J}}/dof$	$\Delta\chi^2_{\mathcal{JQ}}$	F-test	ΔBIC	$\ln B_{\mathcal{JQ}}$
Clusters	-0.55 ± 0.14	39.6/39	$-0.61^{+0.38}_{-0.41}$	$0.51^{+2.55}_{-2.00}$	39.6/38	0.01	5.6%	-3.7	-3.2
SNLS SNIa	-0.417 ± 0.062	112.1/113	-0.65 ± 0.23	$1.32^{+1.37}_{-1.21}$	111.0/112	1.1	69.4%	-3.6	-2.5
Gold SNIa	-0.289 ± 0.062	182.8/155	-0.86 ± 0.21	$2.75^{+1.22}_{-1.10}$	174.6/154	8.2	99.1%	3.1	1.2
Gold+SNLS+Cl	-0.391 ± 0.045	300.8/272	-0.81 ± 0.14	$2.16^{+0.81}_{-0.75}$	290.1/271	10.7	99.8%	5.1	3.0

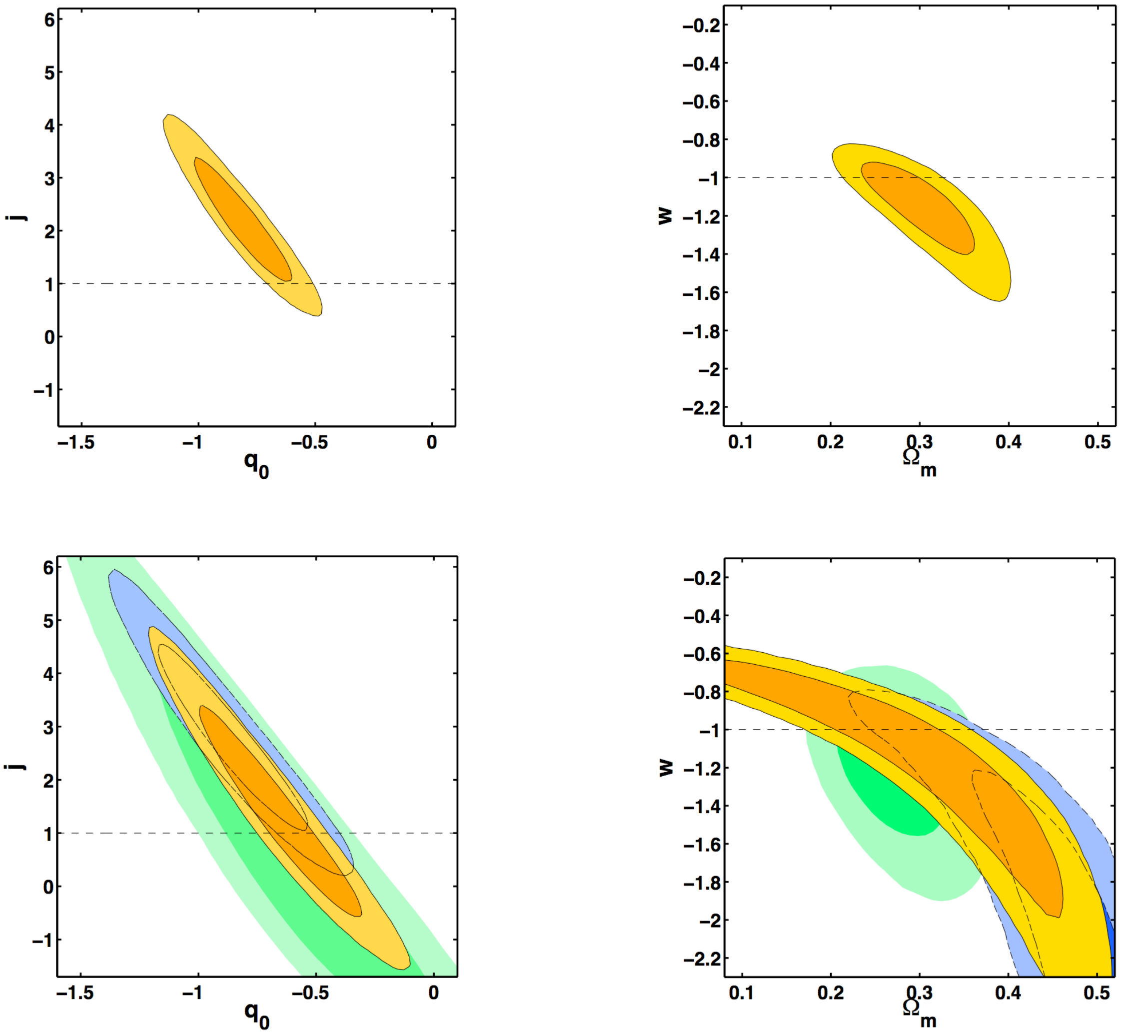

Figure 2.1: A summary of the results from the kinematical (left panels) and dynamical (right panels) analyses. The top left panel shows the 68.3 and 95.4 per cent confidence limits in the (q_0,j) plane for the kinematical model with a constant jerk, j, obtained using all three data sets: both SNIa data sets (Riess et al. 2004; Astier et al. 2005) and the cluster $f_{\rm gas}$ data of Allen et al. (2006). The top right panel shows the results in the ($\Omega_{\rm m}$,w) plane obtained using the same three data sets and assuming HST, BBNS and b priors. (Note that the kinematical analysis does not use the HST, BBNS and b priors). The dashed lines show the expectation for a cosmological constant model in both formalisms ($j = 1$, $w = -1$, respectively). The bottom panels show the confidence contours in the same planes for the individual data sets: the SNLS SNIa data (orange contours), the Riess et al. (2004) 'gold' SNIa sample (blue contours) and the cluster $f_{\rm gas}$ data (green contours). Here, the dashed lines again indicate the cosmological constant model.

where $\Delta\chi^2$ is the difference in the minimum χ^2 between the two models, χ^2_ν is the reduced χ^2 (χ^2/ν, where ν is number of degrees of freedom of the fit, dof) of the final model, and Δm is the difference in the number of free parameters in the two models. Given Δm and ν, we calculate the probability that the new model would give $\Delta\chi^2 \geq F\,\chi^2_\nu\,\Delta m$ by random chance. This allows us to quantify the significance of the model extension.

The Bayesian Information Criterion (BIC) provides a more stringent model selection criterion and is an approximation to the Bayesian Evidence [84]. The BIC is defined as

$$BIC = -2\ln\mathcal{L} + k\ln N \tag{2.27}$$

where $\mathcal{L}$ corresponds to the maximum likelihood obtained for a given model (thus, $-2\ln\mathcal{L}$ is the minimum χ^2), k is the number of free parameters in the model and N is the number of data points. Values for $\Delta BIC < 2$ between two models are typically considered to represent weak evidence for an improvement in the fit. ΔBIC between 2 and 6 indicates 'positive evidence' for an improvement, and values greater than 6 signify 'strong evidence' for the model with the higher BIC [85, 86, 87, 88].

Finally, we have compared the full posterior probability distributions for different models, using the Bayes Factor to quantify the significance of any improvement in the fit obtained. The Bayes Factor is defined as the ratio between the Bayesian evidences of the two models [86]. If $P(D|\theta, M)$ is the probability of the data D given a model M, the Bayesian evidence is defined as the integral over the parameter space, θ

$$E(M) \equiv P(D|M) = \int d\theta P(D|\theta, M)\,P(\theta|M), \tag{2.28}$$

where $P(\theta|M)$ is the prior on the set parameters θ, normalised to unity. We employ top hat priors for all parameters and evaluate the integrals using the MCMC samples:

$$E(M) \sim \frac{1}{N\Delta\theta}\sum^{\mathrm{N}} P(D|\theta_{\mathrm{n}},) \tag{2.29}$$

where $\Delta\theta$ is the volume in the parameter space selected to have probability 1 within

Table 2.2: The marginalised median values and 68.3 per cent confidence intervals obtained analysing all three data sets together. We show the results for the constant j model (kinematical) and the constant w model (dynamical) and their corresponding χ^2 per degree of freedom.

Approach	Model parameters	χ^2/dof
Kinematical	$q_0 = -0.81 \pm 0.14$, $j = 2.16^{+0.81}_{-0.75}$	290.1/271
Dynamical	$\Omega_{\rm m} = 0.306^{+0.042}_{-0.040}$, $w = -1.15^{+0.14}_{-0.18}$	291.7/272

the top hat priors, N is the number of MCMC samples and $\theta_{\rm n}$ the sampled parameter space. Note that $\sum^{\rm N} P(D|\theta_{\rm n})$ is the expected probability of the data in the posterior distribution [82]. The evidence of the model $E(M)$ can be estimated trivially from the MCMC samples as the mean likelihood of the samples divided by the volume of the prior. It is clear, though, that this volume will depend on our selection of the top hat priors. In order to be as objective as possible, within the Bayesian framework, we use the same priors for parameters in common between the two models involved in a comparison. For parameters not in common, we calculate their volumes subtracting their maximum and minimum values in the MCMC samples.

The Bayes factor between two models M_0 and M_1 is $B_{01} = E(M_0)/E(M_1)$. If $\ln B_{01}$ is positive, M_0 is 'preferred' over M_1. If $\ln B_{01}$ is negative, M_1 is preferred over M_0. Following the scale of [85], if $0 < \ln B_{01} < 1$ only a "bare mention" of the preference is considered warranted. If $1 < \ln B_{01} < 2.5$, the preference is regarded as of "substantial" significance. If $2.5 < \ln B_{01} < 5$ the significance is considered to be going from "strong" to "very strong".

2.5 Results

2.5.1 Comparison of constant jerk and constant w models

We first examine the statistical improvement obtained in moving from the simplest kinematical model $\mathcal{Q} = [q_0]$, in which q_0 is the only interesting free parameter, to model $\mathcal{J} = [q_0, j(c_0)]$, where we include constant jerk $j = 1 + c_0$ (i.e. we allow j to take values other than zero). The results obtained, using the three statistical tests described in subsection 2.4.4 applied to each data set alone and for all three data sets together are summarized in Table 2.1. We find that the 'gold' sample is the only data set that, on it's own, indicates a 'substantial' preference for model $\mathcal{J}$ over model $\mathcal{Q}$ according to the Bayes factor test. Note that this is not only due to the fact that the 'gold' sample extends to higher redshifts, thereby providing additional constraining power, but also due to the fact that the 'gold' sample hints a small tension in the ground-based 'gold' sample data to prefer $j > 1$ values [6]. Combining all three data sets, we obtain a 'strong' preference for model $\mathcal{J}$ over model $\mathcal{Q}$, from all three statistical tests. Table 2.1 shows the mean marginalised parameters for each model and the 1σ confidence levels. Combining all three data sets, we obtain tight constraints on $q_0 = -0.81 \pm 0.14$ and $j = 2.16^{+0.81}_{-0.75}$. Our result represents the first measurement of the jerk parameter from cosmological data [7].

Our dynamical analysis of the same three data sets gives $w = -1.15^{+0.14}_{-0.18}$ and $\Omega_{\rm m} = 0.306^{+0.042}_{-0.040}$ (see Table 2.2). Figure 2.1 shows the constraints for both the kinematical (q_0, j; top left panel) and dynamical ($\Omega_{\rm m}, w$; top right panel) models, using all three data sets combined. In both cases, the dashed lines indicates the expected range of results for ΛCDM models (i.e. a cosmological constant). We find that both the kinematical and dynamical analyses of the combined data are consistent with the ΛCDM model at about the 1σ level.

It is important to recognise that the results from the kinematical and dynamical analyses constrain different sets of departures from ΛCDM. We are using two simple, but very different parameterizations based on different underlying assumptions. The results presented in Figure 2.1 therefore provide interesting new support for the ΛCDM model.

The lower panels of figure 2.1 show the constraints obtained for the three data sets

---

[6] An analysis of the 'gold' sample data in which the HST supernovae are excluded leads to even stronger preference for $j > 0$: $\Delta\chi^2_{\mathcal{J}\mathcal{Q}} = 10.6$. In this case, for model $\mathcal{J}$ we obtain $q_0 = -1.17 \pm 0.28$ and $j = 4.95^{+2.05}_{-1.84}$.

[7] Note that Riess et al. (2004) measured $j_0 > 0$ at the 2σ level, where j_0 comes from a Taylor expansion of the Hubble parameter around small redshifts [62]. As noted in subsection 2.2.1 such an expansion is not appropiate when high redshift data are included, as in the 'gold' sample.

when analysed individually. It is important to note the consistent results from the independent SNIa and X-ray cluster data sets. Note that in the dynamical analysis, the X-ray data provide valuable additional constraints on $\Omega_{\rm m}$, when employing the H_0 and $\Omega_{\rm b}h^2$ priors. The overlap of all three data sets in both parameter spaces highlights the robustness of the measurements. Comparing the upper and lower panels of figure 2.1, we see how the combination of data sets significantly tightens the constraints.

2.5.2 More complicated kinematical models

For the combined data set, we have also searched for more complicated departures from ΛCDM by including extra model parameters, as described in Section 2.3. We find no significant evidence for models more complicated than a constant jerk model. In particular, we find a negligible $\Delta\chi^2$ between models with constant jerk $\mathcal{J} = [q_0, j(c_0)]$ and the next most sophisticated model $\mathcal{J}_1 = [q_0, j(a; c_0, c_1)]$, and between the latter model and the next one, $\mathcal{J}_2 = [q_0, j(a; c_0, c_1, c_2)]$.

It is, however, interesting to plot the differences between the constraints obtained for each model. Figure 2.2 shows the current 1σ and 2σ constraints around the median values of $j(a)$ at different scale factors, a, over the range where we have data $[0.36, 1]$. The green, lighter contours show the constraints for the $\mathcal{J}_1$ model and the red, darker contours for the $\mathcal{J}$ model. From this figure it is clear that current data provide the best constraints around $a \sim 0.77$, i.e. $z \sim 0.3$, and that at higher and lower redshift more data are required. For the low redshift range, the forthcoming SDSS II SNIa data will be helpful. For the high redshift range, new HST SNIa and further X-ray cluster data should be available in the near future. In the longer term, SNIa data from the Large Synaptic Survey Telescope (LSST) [8] and the Supernovae Acceleration Probe (SNAP) [9], and X-ray cluster data from Constellation-X [10] should provide tight constraints on both $j(a)$ and $w(a)$. Future galaxy redshift surveys covering a high redshift range will also help to tighten these constraints, using the baryon oscillation

---

[8] http://www.lsst.org/lsst_home.shtml

[9] http://snap.lbl.gov/

[10] http://constellation.gsfc.nasa.gov/

experiment [19, 18].

2.5.3 Comparison of distance measurements

It is interesting to compare directly the distance curves for the kinematical (constant j) and dynamical (constant w) models, as determined from the MCMC chains. Fig 2.3 shows the 68.3 and 95.4 per cent confidence limits on the offset in distance, as a function of scale factor, relative to a reference ΛCDM cosmology with $\Omega_{\rm m} = 0.27$, $\Omega_\Lambda = 0.73$. We see that the kinematical and dynamical results occupy very similar, though not identical, loci in the distance-scale factor plane. For the dynamical analysis, the addition of the extra constraint on $\Omega_{\rm m}$ from the normalization of the $f_{\rm gas}$ curve tightens the constraints and pushes the results in a direction slightly more consistent with the reference ΛCDM cosmology.

2.5.4 Comparison with Riess et al. (2004)

For comparison purposes, we also present the results obtained using the linear parameterization of $q(z)$ described by equation (2.3) and used by [7]. Figure 2.4 shows the constraints in the plane $(q_0, dq/dz)$ determined from each data set, and by combining the three data sets (solid, orange contours). It is clear that the constraints from the three independent data sets overlap and that by combining them we obtain significantly tighter results than using the 'gold' sample alone.

2.6 The distance to the last-scattering surface

Finally, we note that there is one further pseudo-distance measurement available to us - the distance to the last scattering surface from CMB data. Although this is not a purely kinematical data point, for illustration purposes we show the constraints on $j(a)$ that can be achieved if one is willing to make extra assumptions and include this measurement. The extra assumptions involved, though strong, are well-motivated. In detail, in order to use the distance to last scattering, we assume that dark matter behaves like standard cold dark matter at all redshifts, an assumption well tested

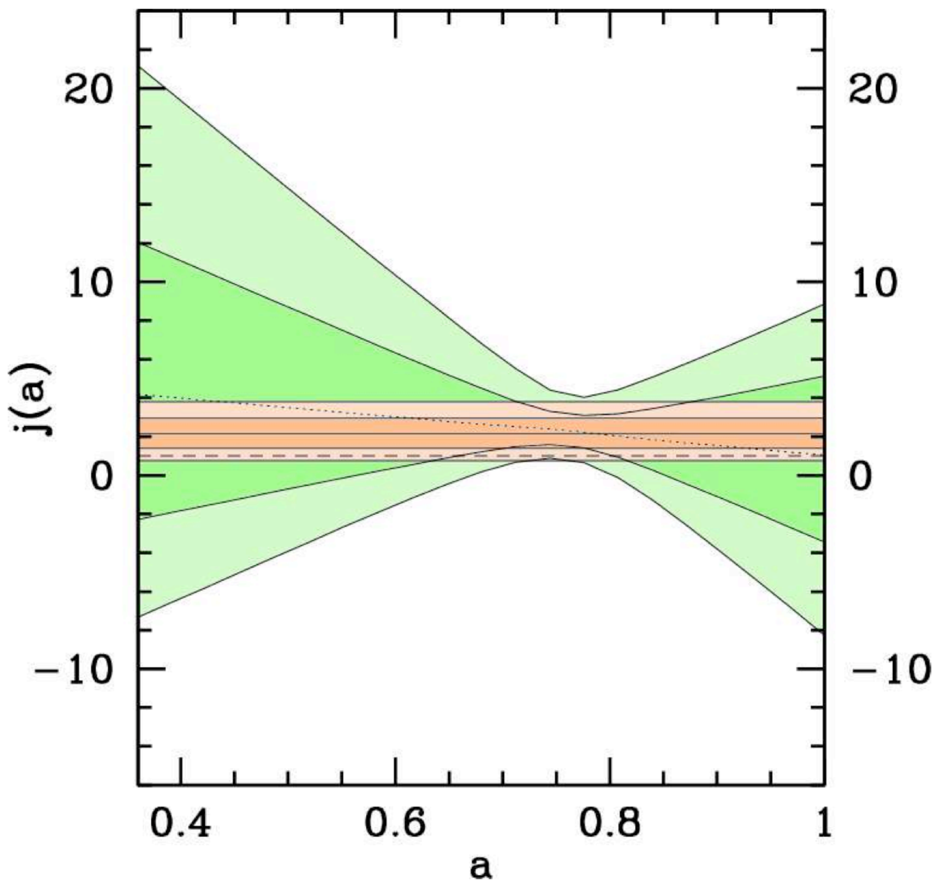

Figure 2.2: The 68.3 and 95.4 per cent confidence variations about the median values for $j(a)$ as a function of the scale factor a, over the range where we have data [0.36,1]. Results are shown for the constant jerk model (model $\mathcal{J}$) (red, darker contours) and $\mathcal{J}_1$ model (green, lighter contours). In both cases, the constraints for all three data sets have been combined. The dashed line indicates the expectation, $j = 1$ (constant) for a cosmological constant (ΛCDM) model.

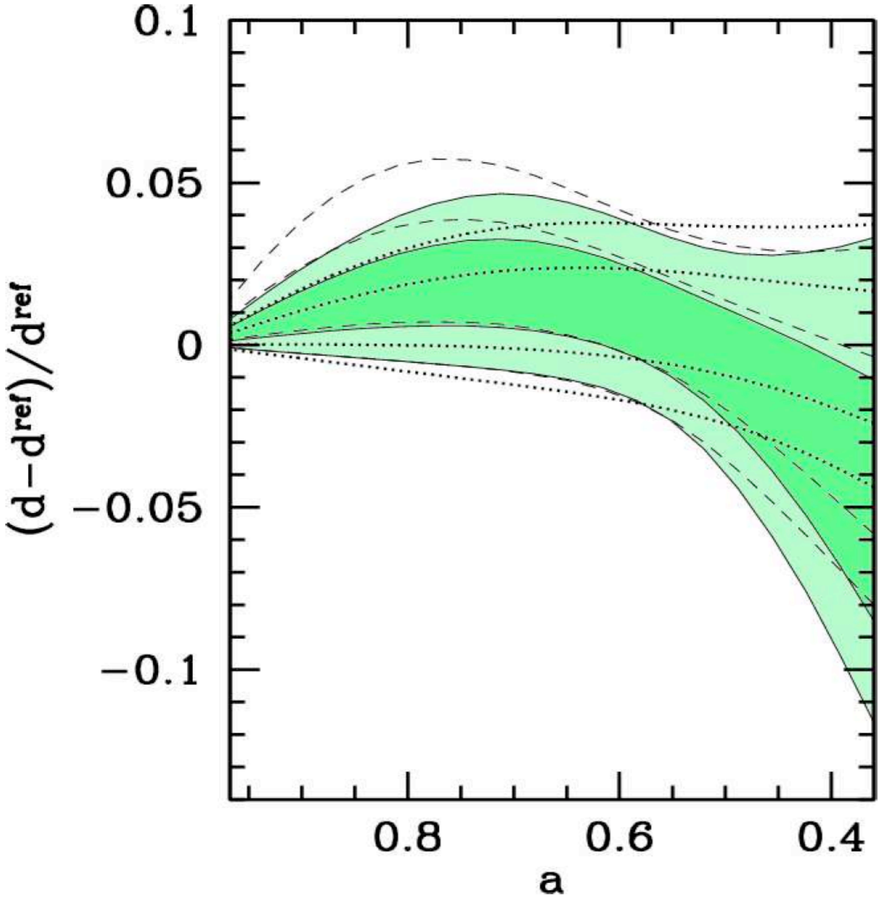

Figure 2.3: The 68.3 and 95.4 per cent confidence limits on the offset in distance as a function of scale factor, relative to the reference ΛCDM cosmology, for both the kinematical (constant j; green, shaded curves) and dynamical (constant w; dotted and dashed curves) analyses. The dotted curves show the results for the dynamical analysis in which the additional constraint on $\Omega_{\rm m}$ from the normalization of the $f_{\rm gas}$ curve is used. The dashed curve is for a dynamical analysis where this extra constraint on the normalization is ignored. The same MCMC samples used to construct Fig 2.1 have been used.

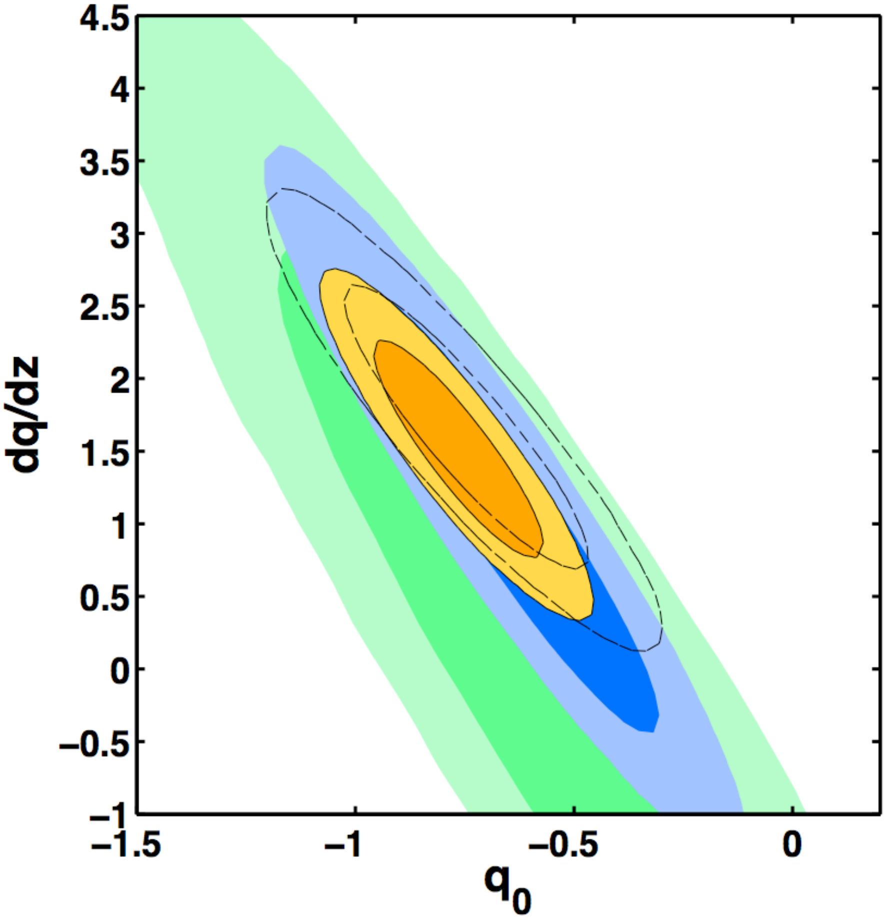

Figure 2.4: The 68.3 and 95.4 per cent confidence limits in the (q_0,dq/dz) plane obtained using the SNIa data from the first year of the SNLS (Astier et al. 2005), the 'gold' sample of Riess et al. (2004) (dashed contours), the cluster $f_{\rm gas}$ data of Allen et al. (2006) (green contours) and the combination of all three data sets (orange contours).

by e.g. galaxy cluster, weak lensing and galaxy redshift surveys at low redshifts and CMB experiments at high-z. We also assume that pre-recombination physics can be well described by a standard combination of cold dark matter, a photon-baryon fluid and neutrinos, and that any early dark energy component has a negligible affect on the dynamics. With these assumptions, one can construct the comoving angular diameter distance to the last scattering surface from $d_{\rm A} = r_{\rm s}(a_{dec})/\theta_{\rm A}$, where $r_{\rm s}(a_{rec})$ and $\theta_{\rm A}$ are the comoving sound horizon at decoupling and the characteristic angular scale of the acoustic peaks, respectively. For a geometrically flat Universe with a negligible early dark energy component, we calculate the sound horizon at decoupling as [89]

$$r_{\rm s}(a_{\rm dec}) \simeq \int_0^{a_{\rm dec}} \frac{c_{\rm s}(a)}{H_0(\Omega_{\rm m}a + \Omega_{\rm rad})^{1/2}}\, da\,, \tag{2.30}$$

where $c_{\rm s}(a) = c/[1 + (3\Omega_{\rm b}a)/(4\Omega_\gamma)]$ is the sound speed in the photon-baryon fluid, $\Omega_{\rm rad} = \Omega_\gamma + \Omega_\nu$ is the present radiation energy density, and Ω_γ and Ω_ν are the present photon and neutrino energy densities, respectively. We use our X-ray galaxy cluster data, assuming HST, BBNS and b priors, to determine $\Omega_m = 0.27 \pm 0.04$ (Allen et al. 2006; note that this constraint mainly comes from low-redshift clusters). We also use the COBE measurement of the CMB temperature $T_0 = 2.725 \pm 0.002$K [90] and a standard three neutrino species model with negligible masses to obtain $\Omega_{\rm rad}$. For these constraints, we obtain $r_{\rm s}(z_{\rm dec}) \simeq 146 \pm 10$Mpc.

From [91] we have the multipole of the first acoustic peak $l_1 = 220.7 \pm 0.7$. This is related to $l_{\rm A}$ by a shift ϕ, $l_1 = l_{\rm A}(1-\phi)$. Using the fitting formula of [92], the BBNS prior for $\Omega_{\rm b}h^2$, a scalar spectral index $n_{\rm s} = 0.95 \pm 0.02$ [3] and assuming no early dark energy, we find $\theta_{\rm A} = 0.6 \pm 0.01$ degrees. We then obtain a pseudo-model-independent distance to decoupling, $d(z_{\rm dec}) \simeq 13.8 \pm 1.1$Gpc, where $z_{\rm dec} = 1088$ [3].

Fig 2.5 shows the tightening of the constraints obtained using this "data-point-prior" at high redshift [11]. Note that figure 2.5 is plotted on the same scale as figure 2.2

---

[11] Note that extending the analysis to the decoupling redshift $z_{\rm dec} = 1088$ means that the radiation density becomes non-negligible. Although, j can still be calculated as usual, $j^{\Lambda CDM}$ will not equal 1 at these redshifts. However, the ΛCDM model can then be almost perfectly described as $j^{\Lambda CDM}(a) = 1 + 2/(1 + (a/a_{\rm eq}))$ (for details see [77]) where $a_{\rm eq}$ is the mean marginalised scale factor at equality, from WMAP data. We have explicitly verified that, within the 1σ values of $a_{\rm eq}$, systematic offsets

and shows $\mathcal{J}$ (red, darker contours) and $\mathcal{J}_1$ (green, lighter contours) models as before, plus the $\mathcal{J}_2$ model (blue contours). Note also that here the range of the data is $[a_{\rm min} = 0.0009, a_{\rm max} = 1]$. Again, using equation (2.15) we rescale the Chebyshev interval $[-1, 1]$ to locate the functions $\Delta j(a; \mathcal{C})$ in the range of scale factor spanned by the data. The prior information at high redshift, from the distance to last scattering, tightens the constraints significantly. Evidently, the constraints from the kinematic analysis are sensitive to the data quality at high redshift.

2.7 Conclusions

We have developed a new kinematical approach to study the expansion of the history of the Universe, building on the earlier work of [1]. Our technique uses the parameter space defined by the current value of the cosmic deceleration parameter q_0 and the jerk parameter j, where q and j are the dimensionless second and third derivatives of the scale factor with respect to cosmic time. The use of this (q_0, j) parameter space provides a natural framework for kinematical studies. In particular, it provides a simple prescription for searching for departures from ΛCDM, since the complete set of ΛCDM models are characterized by $j = 1$ (constant).

We have applied our technique to the three best available sets of redshift-independent distance measurements, from type Ia supernovae studies [7, 8] and measurements of the X-ray gas mass fraction in X-ray luminous, dynamically relaxed galaxy clusters [56]. Assuming geometric flatness, we measure $q_0 = -0.82 \pm 0.14$ and $j = 2.16^{+0.81}_{-0.75}$ (Figure 2.1). Note that this represents the first measurement of the cosmic jerk parameter, j. A more standard, dynamical analysis of the same data gives $w = -1.15^{+0.14}_{-0.18}$ and $\Omega_{\rm m} = 0.306^{+0.042}_{-0.040}$, also assuming flatness and HST, BBNS and b priors (Figure 2.1). Both sets of results are consistent with the standard ΛCDM paradigm, at about the 1σ level.

In comparison to standard, dynamical approaches, our kinematical framework provides a different set of simple models and involves fewer assumptions. In particular,

---

due to the affects of radiation have a negligible effect on the derived distances.

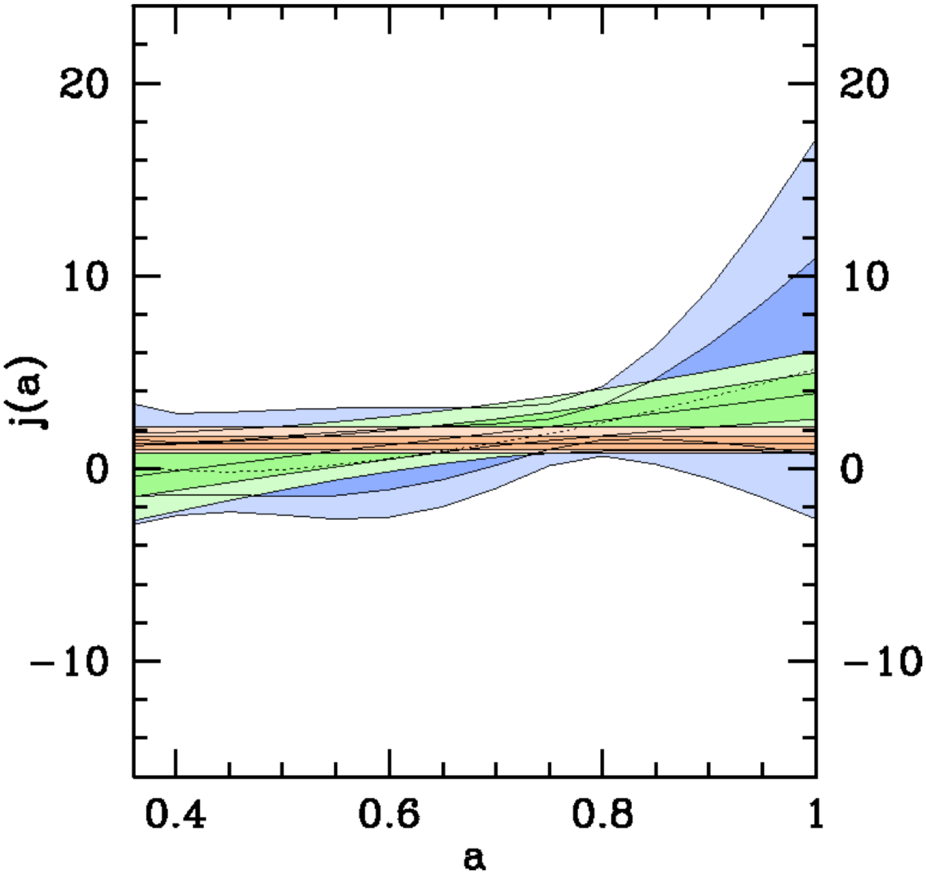

Figure 2.5: 1σ and 2σ constraints on $j(a)$ over the range (including the distance to the last scattering surface) of the data [0.0009,1]. Note that this figure and figure 2.2 are plotted on the same scale for comparison purposes. This figure shows the same models as figure 2.2 plus the $\mathcal{J}_2$ model, and uses the CMB prior as described at the text. The dotted line shows the median $j(a)$ curve for the $\mathcal{J}_1$ model.

kinematical analyses such as that presented here do not assume a particular gravity theory. The combination of the kinematical and dynamical approaches therefore provides important, complementary information for investigating late time cosmic acceleration. The fact that both the kinematical and dynamical results presented here are consistent with ΛCDM provides important additional support for that model. The fact that the two independent sets of distance measurements, from X-ray galaxy clusters and supernovae, are individually consistent with ΛCDM, is reassuring (Figure 2.1).

We have searched for departures from ΛCDM using a new scheme based on the introduction of Chebyshev polynomials. These orthonormal functions allow us to expand any deviation from ΛCDM, $\Delta j(a;\mathcal{C})$, as a linear combination of polynomials. We use the coefficients of these polynomials, $\mathcal{C}$, as fit parameters. The current data provide no evidence for a dependence of j on a more complicated than a constant value. However, higher order terms may be required to describe future data sets. In that case, our scheme has the advantage that, over a finite interval and using enough high order terms, it will provide an acceptable global approximation to the true underlying shape. Note that this scheme is also applicable to dynamical studies of the evolution of the dark energy equation of state, $w(a)$. Note also that Chebyshev polynomial expansions of the same order for $w(a)$ and $j(a)$ explore a different set of models. For example, a constant $j \neq 1$ model corresponds to an evolving $w(a)$ model and vice versa.

We suggest that future studies should endeavour to use both kinematical and dynamical approaches where possible, in order to extract the most information from the data. The two approaches have different strengths, can be applied to with a variety of data sets, and are highly complementary. The combination of techniques may be especially helpful in distinguishing an origin for cosmic acceleration that lies with dark energy (i.e. a new energy component to the Universe) from modifications to General Relativity.

Acknowledgment

We acknowledge helpful discussions with A. Frolov and technical support from G. Morris. The computational analysis was carried out using the KIPAC XOC compute cluster at SLAC. SWA acknowledges support from the National Aeronautics and Space Administration through Chandra Award Number DD5-6031X issued by the Chandra X-ray Observatory Center, which is operated by the Smithsonian Astrophysical Observatory for and on behalf of the National Aeronautics and Space Administration under contract NAS8-03060. RDB acknowledges support from National Science Foundation grant AST05-07732. This work was supported in part by the U.S. Department of Energy under contract number DE-AC02-76SF00515.

2.A Analysis in the kinematic plane

Note: In the chapter and the associated paper, an unpublished paper, [77], was cited. The parts of that paper relevant for this chapter are presented in this appendix.

In this chapter, we provided constraints on the present deceleration parameter q_0 and a constant j (along with other models) using kinematics measurements of the expansion history. We did not discuss the behavior of the scale-factor $a(t)$ corresponding to different points in the $q_0 - j$ plane. This appendix is intended to provide a global picture of the behavior of models corresponding to different points in this plane. Although we concentrate on $q_0 - j$ models, the method used is quite general and can be applied to the study of expansion history for more general cases as well.

Consider the following identity:

$$\frac{\dot{a}^2}{2H_0^2} + V(a) = 0$$

where $V(a) \equiv -a^2H^2/2H_0^2$ with $H(a) = \dot{a}/a$. $V(a)$ is usually provided by the model under consideration. For example in GR, using the Friedmann equation we get $V(a) = -4\pi G a^2\rho/3H_0^2 + k/3H+0^2$ where ρ is the total energy density and k stands for spatial curvature.

We rescale time as follows $H_0 t \rightarrow t$ to obtain

$$\frac{\dot{a}^2}{2} + V(a) = 0$$

Considering $a(t)$ as the trajectory of a particle with unit mass, $V(a)$ and $\dot{a}^2/2$ play the roles of potential energy and kinetic energy respectively of that particle. This particle has zero total energy. The classical turning points in the motion of this particle correspond to the zeroes of $V(a)$. Let us assume that at the present time t_0, $a(t_0) = 1$, $\dot{a}(t_0) > 0$ and $V(t_0) < 0$ (since the universe is expanding). If there exists $0 < a_t < 1$ such that $V(a_t) = 0$ then there exists a time t_t in the past when $a(t)$ transitions from a decreasing function of time to an increasing function of time. Similarly, if there exists $1 < a_t$ such that $V(a_t) = 0$ then there exists a time t_t in the future when $a(t)$ transitions from an increasing function of time to a decreasing function of time. Finally if $V(a_t) = 0$ has roots $a_t^{max} > 1$ and $0 < a_t^{min} < 1$ then $a(t)$ oscillates between a_t^{max} and a_t^{min}. Hence the problem of understanding this motion is reduced to determining whether $V(a) = 0$ has a solution in the the regions $0 < a < 1$ and $a > 1$. In terms of cosmology, $0 < a_t < 1$ implies a bounce in the past, $1 < a_t$ implies a contracting phase in the future (big crunch) and if a_t exist in both regions then we have an oscillating universe (We ignore cases where $V'(a_t) = 0$).

We now turn our attention to a specific form of $V(a)$. Let us consider the case where $V(a)$ is obtained by solving the jerk equation (see equation (2.7)):

$$a^2 V''(a) - 2jV(a) = 0$$

with the initial conditions $V(1) = -1/2$ and $V'(1) = q_0$. The solution, for $j =$ constant is given by

$$V(a) = -\frac{1}{2}\left(\frac{p-u}{2p}a^{p-\frac{1}{2}} + \frac{p+u}{2p}a^{-p-\frac{1}{2}}\right)$$

where

$$p = \frac{1}{2}\sqrt{1+8j}, \qquad u = 2\left(q_0 + \frac{1}{4}\right)$$

The roots of $V(a) = 0$ are given by (excluding $a = 0$)

$$a_t^{2p} = \left(\frac{u+p}{u-p}\right)$$

We first delineate different regions in the $q_0 - j$ plane based on the behavior of the roots. The relevant regions are delineated based on the following curves (see Figure 2.6):

$$j = 2q_0^2 + q_0,$$

$$j = -\frac{1}{8},$$

$$q_0 = -\frac{1}{4}.$$

- **Region I:** $j > 2q_0^2 + q_0$; $p > |u|$. No positive, real a_t. This universe has a big

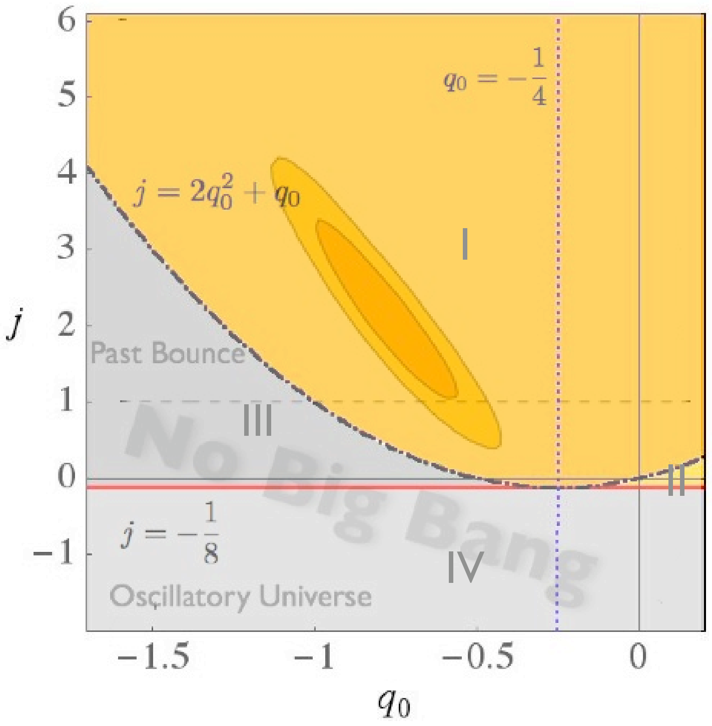

Figure 2.6: Delineated regions in the $q_0 - j$ plane. The constraints on $q_0 - j$ lie safely within the physically allowed region. Note that we only used data from the relatively low redshift universe where the constant j models can provide a good description of the expansion history.

bang singularity in the past.

- **Region II:** $-1/8 < j < 2q_0^2 + q_0$, $q_0 > -1/4$; $0 < p < |u|$; $1 < a_t$. If the universe is currently expanding, then it continues expanding untill it reaches a_t. At this point it turns around and starts its collapse to a future singularity. This universe has a big bang singularity in the past and a big crunch in the future.

- **Region III:** $-1/8 < j < 2q_0^2 + q_0$, $q_0 < -1/4$; $|u| < p$; $0 < a_t < 1$. $V(a) = 0$ has a root $a_t < 1$. If the universe is currently expanding, then it continues expanding. This region has a bounce in the past.

- **Region IV:** $j < -\frac{1}{8}$. $V(a)$ is oscillatory with roots $a_t > 1$ and $a_t < 1$.This implies that $a(t)$ is oscillatory.

The panels in Figure 2.7 show how different forms of $V(a)$ (corresponding to points in $q_0 - j$ plane) yield very different behaviors for $a(t)$. As mentioned before this technique, which is often used in classical mechanics, provides a simple yet powerful means of understanding the behavior of $a(t)$ for very general scenarios.

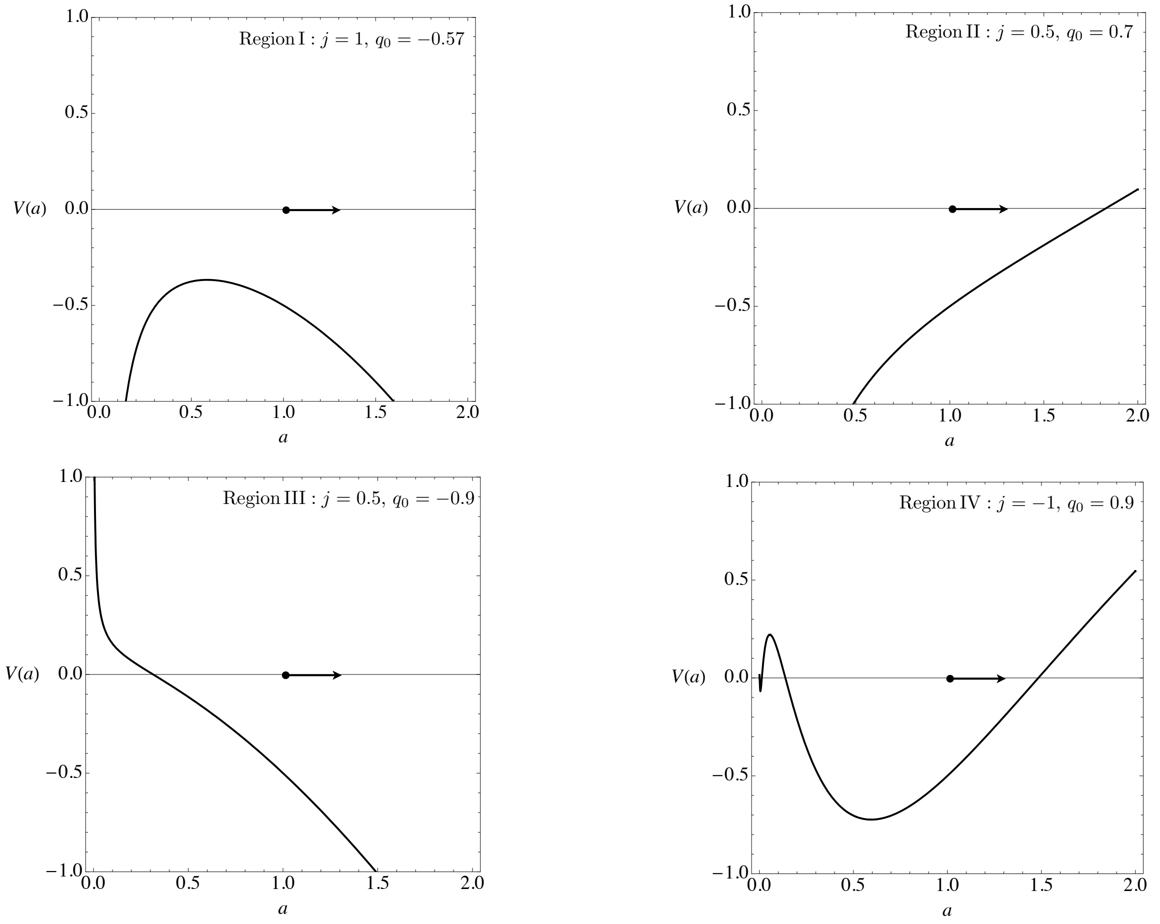

Figure 2.7: The above panel shows typical forms of $V(a)$ in regions I, II, III and IV as discussed in the text. By thinking of $V(a)$ as an effective potential, it is easy to understand the qualitative behavior of $a(t)$ in these models.

2.B Cosmology with a constant ratio

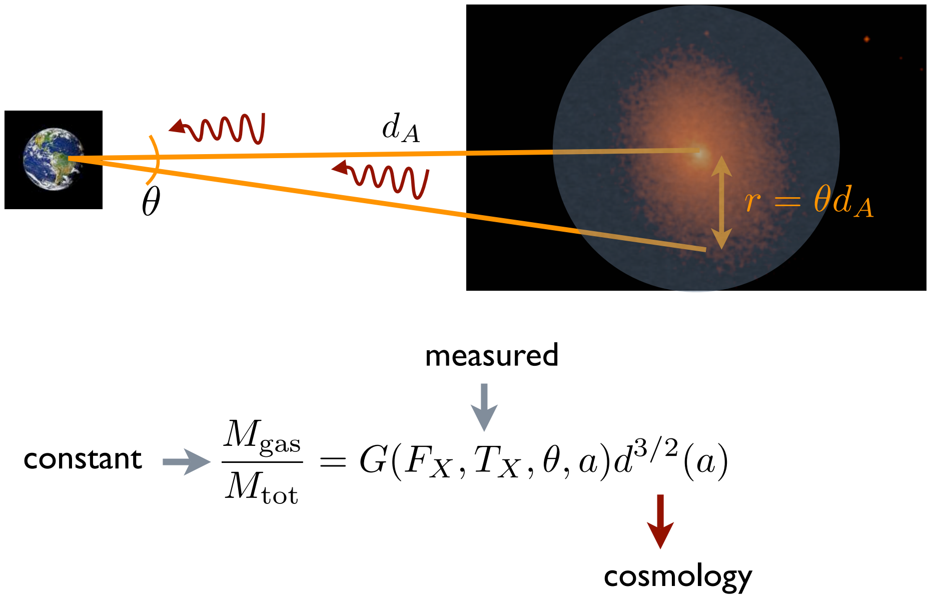

Figure 2.8: Distance measurements with clusters of galaxies

In this chapter we used $f_{\rm gas}$ (defined below) measurements for constraining the expansion history of the universe. In this short note, we describe how these measurements serve as probes of cosmology. This is meant to be a pedagogical note, where we ignore some details for the sake of simplicity. For a more in depth discussion, especially of the actual observations, see [56] and references therein.

Definition: $f_{\rm gas}$ is the fraction of X-ray emitting gas to the total mass in clusters:

$$f_{\rm gas} = \frac{M_{\rm gas}}{M_{\rm tot}}.$$

As we show in this appendix,

$$\frac{M_{\rm gas}}{M_{\rm tot}} = G(F_X(\theta), T_X(\theta), \theta, a) d^{3/2}(a), \tag{2.31}$$

where the X-ray flux F_X, temperature T_X, angular size θ and scaler-factor a are observables, G is a known function of these observables and $d(a)$ is the co-moving distance to the cluster.

Main idea: Assume $f_{\rm gas}$ is constant[12], measure $G(F_X(\theta), T_X(\theta), \theta, a)$, infer $d(a)$ which will constrain the expansion history.[13]

The rest of this appendix is devoted to providing a derivation for (2.31). We begin by deriving an expression for $M_{\rm tot}$ in terms of the observables mentioned above and cosmological distances. The main assumptions going into this part of the derivation are those of hydrostatic equilibrium ($dP/dr = GM\rho/r^2$) and the ideal gas law ($P = nk_BT$) for the X-ray emitting gas. With these assumptions we get an expression relating the temperature, number density (n_X) of the gas and the total mass within a given radius.

$$\frac{d\ln n_X(r)}{d\ln r} + \frac{d\ln T_X(r)}{d\ln r} = \frac{\mu}{k_BT_X(r)}\frac{G_N M_{\rm tot}(r)}{r}, \tag{2.32}$$

where μ is the average mass per baryon. Since we observe things in the sky as a function of the angular size θ, rather than the physical size r, we re-express the above equation in terms of the angular size to get

$$\frac{d\ln n_X(\theta)}{d\ln \theta} + \frac{d\ln T_X(\theta)}{d\ln \theta} = \frac{\mu}{k_BT_X(\theta)}\frac{G_N M_{\rm tot}(\theta)}{\theta d_A(a)}, \tag{2.33}$$

where d_A is the angular diameter distance to the cluster. For the sake of simplicity, we assume that $n_X \propto T_X^\gamma$. Then, the LHS is $(\gamma+1)d\ln T_X/d\ln\theta$. T_X can be measured as a function of θ. So, we get

$$M_{\rm tot}(\theta) = \left[(\gamma+1)\frac{k_B}{G\mu}\theta^2\frac{dT_X(\theta)}{d\theta}\right]d_A(a). \tag{2.34}$$

with everything in the square brackets being a directly measurable quantity for each cluster. Note that, instead of assuming the power law relation, one can also obtain

---

[12] See discussion at the end of this appendix.

[13] In this sense it is very similar to the way Type Ia supernovae are used to measure cosmological distances with the following identifications: SN Luminosity → $f_{\rm gas}$, flux → $G(F_X(\theta), T_X(\theta), \theta)$.

n_X from X-ray flux measurements and get temperature T_X from the spectrum.

Let us now turn to deriving an expression for $M_{\rm gas}$. As in the case of $M_{\rm tot}$, we would like to derive an expression for $M_{\rm gas}$ in terms of the X-ray observables, angular sizes and cosmological distances. The key point in this derivation is that the number density of the gas can be obtained from the measured temperature and flux. The mass of the X-ray emitting gas:

$$M_{\rm gas} = g_1 \mu \, \bar{n}_X(r) V(r) = g_1 \mu \, \bar{n}_X(\theta)(\theta d_A(a))^3, \tag{2.35}$$

where $V(r) \propto r^3 = (\theta d_A)^3$ is the volume enclosed within a physical radius r and $\bar{n}_X$ is the (volume averaged) number density of the X-ray emitting gas. The factor g_1 is a geometric factor (which arises from the volume average). Since we cannot measure $\bar{n}_X$ directly, we will express it in terms of the X-ray observables and distances as follows. The X-ray flux from a region with angular size θ is

$$F_X(\theta) = \frac{L_X(\theta)}{4\pi d_L^2(a)}.$$

In the above expression $d_L(a)$ is the luminosity distance and $L_X(\theta)$ is the X-ray luminosity. Now, $L_X \propto \bar{n}_X^2 V$. More explicitly, it is given by

$$L_X(\theta) = g_2(T_X)\bar{n}_X^2(\theta)(\theta d_A(a))^3,$$

where g_2 contains a dimensionless gaunt factor and a temperature dependence which depends upon the detailed microphysics. For this note, we will not specify its functional form. Note as in g_1, g_2 will also contain a geometric factor from volume averaging. Re-arranging the above equation, we get

$$\bar{n}_X(\theta) = g_2^{-1/2}(T_X) \left[\frac{4\pi F_X(\theta) d_L^2(a)}{(\theta d_A(a))^3}\right]^{1/2}$$

Using this expression for $\bar{n}_X$ in (2.35), we get

$$M_{\rm gas}(\theta) = g_1 g_2^{-1/2}(T_X) \mu \left[4\pi(\theta) F_X(\theta)\theta^3\right]^{1/2} d_L(a) d_A^{3/2}(a). \tag{2.36}$$

Using the expressions in (2.34) and (2.36) in (2.31) we get

$$f_{\text{gas}}(\theta) = \frac{M_{\text{gas}}(\theta)}{M_{\text{tot}}(\theta)} = g_1 g_2^{-1/2}(T_X) \left[(\gamma+1) \frac{k_B}{G\mu^2} \frac{dT_X(\theta)}{d\theta} \right]^{-1} \left[\frac{4\pi}{a} \frac{F_X(\theta)}{\theta} \right]^{1/2} d^{3/2}(a),$$

where we used $a^{-1}d_A(a) = ad_L(a) = d(a)$. Note that $F_X(\theta)$ is the flux from the entire region within θ. Also note that we get f_{gas} as a function of θ. f_{gas} is expected to be constant across a population of clusters when measured at the same over-density only (based on simulations). Now, a given over-density will correspond to a different $\theta = \theta_{2500}$ for each cluster ("2500" stands for an over-density of 2500 times the critical density). This chosen over-density (and hence θ_{2500}) is measured by using the observed temperature in the Virial relation. It is this angular size where f_{gas} is measured. For more details, see [56].

As promised, we have derived the function $G(F_X(\theta), T_X(\theta), \theta, a)$ up to the factors g_1 and g_2. The main assumptions were those of hydrostatic equilibrium, use of the ideal gas law and spherical symmetry which can all be relaxed in a more detailed study.

We end with a few statements about the main idea and some caveats. We assumed that f_{gas} is constant across clusters. Although, seemingly obvious, this statement requires some qualification. As a first approximation, since clusters are the largest collapsed objects in our universe, the ratio reflects the average baryon to matter ratio in our universe (after taking into account the fraction in stars). In reality, f_{gas} is expected to evolve slightly with redshift due to the loss of baryons from the clusters which has to be modeled using simulations (or have extra parameters that need to be marginalized over). Also, non-thermal pressure from turbulence, magnetic fields etc. is expected to play a role in determining the total mass. Again, simulations likely shed light on this in this aspect in the near future. The value of f_{gas} can be obtained from local measurements ($a \approx 1$), which is independent of cosmology. However, it is difficult to find a large enough sample of clusters at low enough redshifts. So the calibration of f_{gas} includes some information about cosmology (mainly H_0 and Ω_m). To ameliorate this problem, in practice, a ratio of the true distance and the distance in a reference cosmology is used. It is also possible to use the constancy of f_{gas} rather than its numerical value for kinematic measurements.

Acknowledgements

I would like to thank Steve Allen, David Rapetti, Adam Mantz and Evan Million for helpful discussions while writing this short note.

2.C Cosmokinematics

2.C.1 Introduction

In this appendix, we investigate the behavior of a class of dimensionless kinematic variables which allows us to extract salient features of the expansion history. When necessary, we will use the ΛCDM model as a concrete example, although most of the discussion carries over to more general models. This appendix is independent of the chapter, except that it provides additional motivation and background for using kinematic variables.

It is perhaps worth asking, why one should consider a kinematic approach. As we know, kinematic approaches have been fruitful in the past. Long before Newton came up with his laws of motion, Galileo was able to determine empirical relations between kinematic variables for describing the motion of objects at constant acceleration. In cosmology, we too are perhaps at a similar stage. We can measure the expansion history, but the law governing it is yet to be fully understood. A better understanding of the kinematics will hopefully lead us to a deeper understanding of the dynamics responsible for cosmic acceleration.

Consider an expanding, spatially flat, homogeneous and isotropic universe. In a metric theory of gravity, such universe can be described by a FRW metric of the form

$$ds^2 = -dt^2 + a^2(t)\delta_{ij}dx^i dx^j, \tag{2.37}$$

where $a(t)$ is the dimensionless "scale factor" normalized to be $a(t_0) = 1$ at the present time t_0. The scale factor is related to the the redshift z through $a = (1+z)^{-1}$. In what follows we shall assume that $a(t)$ is sufficiently smooth. Interesting features regarding the behavior of the scale factor can be gleaned from a set of dimensionless functions $u_n(t)$ constructed out of the derivatives of the scale factor. For $n = 1$ we explicitly define

$$u_1(t) \equiv \frac{1}{H_0} \frac{\dot{a}(t)}{a(t)}, \tag{2.38}$$

where H_0 is the Hubble constant. For $n \geq 2$

$$u_n(t) \equiv \frac{a^{(n)}(t) a^{n-1}(t)}{\dot{a}^n(t)}, \tag{2.39}$$

where "." $= d/dt$ and $a^{(n)}(t) = d^n a(t)/dt^n$. For example for $n = 2, 3$ we have

$$\begin{aligned} u_2(t) &= \frac{\ddot{a}(t)a(t)}{\dot{a}^2(t)} \equiv q(t), \\ u_3(t) &= \frac{\dddot{a}\ (t)a^2(t)}{\dot{a}^3(t)} \equiv j(t), \end{aligned} \tag{2.40}$$

where $q(t)$ is the acceleration parameter and $j(t)$ is the jerk parameter. Note that we define $q(t)$ as the acceleration parameter rather than the more conventional deceleration parameter which differs from our definition by a minus sign. A more familiar context where these dimensionless functions are introduced is in the Taylor expansion of the Hubble parameter around the present time t_0:

$$H(t) = H_0[1 + (1 + q_0)H_0(t - t_0) + \frac{1}{2!}(j_0 - 3q_0 + 2)H_0^2(t - t_0)^2 + ...], \tag{2.41}$$

where H_0, q_0, j_0 etc. refer to the values of the kinematic parameters evaluated at the present time t_0.

2.C.2 Kinematic flows

A useful feature of the kinematic variables is that for any power law scale factor

$$a(t) \propto t^\beta \Longrightarrow u_n(t) = \frac{(\beta - 1)(\beta - 2)...(\beta - n - 1)}{\beta^{n-1}} \tag{2.42}$$

for $n \geq 2$. For an exponetial scale factor, it is even simpler

$$a(t) \propto e^{\beta t} \Longrightarrow u_n(t) = 1 \quad n \geq 2. \tag{2.43}$$

Differentiating equation [2.39] with respect to time and changing the independent variable to "$\ln a$" with $'$ denoting $d/d\ln a$ we obtain the following recursion relation between these variables

$$u_n' = u_{n+1} + (n - 1 - nq)u_n. \tag{2.44}$$

Writing this system explicitly, we have

$$\begin{aligned} H' &= (q-1)H, \\ q' &= j + (1-2q)q, \\ j' &= s + (2-3q)j, \\ s' &= c + (3-4q)s, \\ &. \\ &. \\ &. \end{aligned} \tag{2.45}$$

When working with kinematic variables, the above identities often simplify expressions considerably. One can think about the above equations as a dynamical system with critical points

$$u_{n+1} = -(n - 1 - nq)u_n. \tag{2.46}$$

To analzse the stability of the finite critical points we consider the evolution of the a small perturbation away from the critical point

$$\delta u_n' = \delta u_{n+1} - \delta u_n - n\delta q. \tag{2.47}$$

The fixed point $u_n = 1$ with $2 \leq n \leq N$ is a stable fixed point if we truncate the series at any $N \geq 2$ setting $u_N = 1$. All the eigenvalues lie in the left half of the complex plane and we get the trajectories spiraling into the fixed point. Note that so far we have not assumed anything about $a(t)$. These identities are true for any smooth function and have nothing to do with cosmology yet. However, to solve this system, we need a closure relation which is where the law determining $a(t)$ (or some combination of kinematic variables) comes in. The physics is in the closure relations. As we shall see simple algebraic closure relations between j and q describe a very large number of cosmological models. A similar system had been investigated in the context of inflation with slow roll variables in place of kinematic variables (see for example [93] and references therein). Also see [29] for a related approach in reconstructing the quintessence potential at late times.

Having defined the kinematic variables and some of their properties we turn our attention to their importance in cosmology. The kinematic variables discussed above are quite useful in understanding salient features about the expansion rate and the contents driving the expansion. Although we want to stay away from dynamics, it helps to know how these variable are related to the behavior of the contents of our universe. For example, in the standard cosmological model with GR, we can relate the kinematic variables to the total pressure and density through the Friedmann equations as follows:

$$\begin{aligned} H^2 =& \frac{8\pi G}{3}\rho \\ q =& -\frac{1}{2} - \frac{4\pi G}{H^2}P \\ j =& 1 - \frac{4\pi G}{H^3}\dot{P} \end{aligned} \tag{2.48}$$

- $H(a)$: Sign tells us whether the universe is expanding or contracting. Its magnitude tells us how much stuff there is in our universe.

- $q(a)$: Sign tells us whether the universe is accelerating or decelerating. Its magnitude tells us about the total pressure in our universe.

- $j(a)$: Sign tells us whether the rate or acceleration is increasing or decreating. $j(a) \neq 1$ implies a time evolving pressure.

During an era with non-relativistic matter ($P_m = 0$) and a cosmological constant ($P_\Lambda = -\rho_\Lambda$) the effective pressure $P = P_\Lambda + P_m = -\Lambda/8\pi G = \textit{constant}$. Hence in

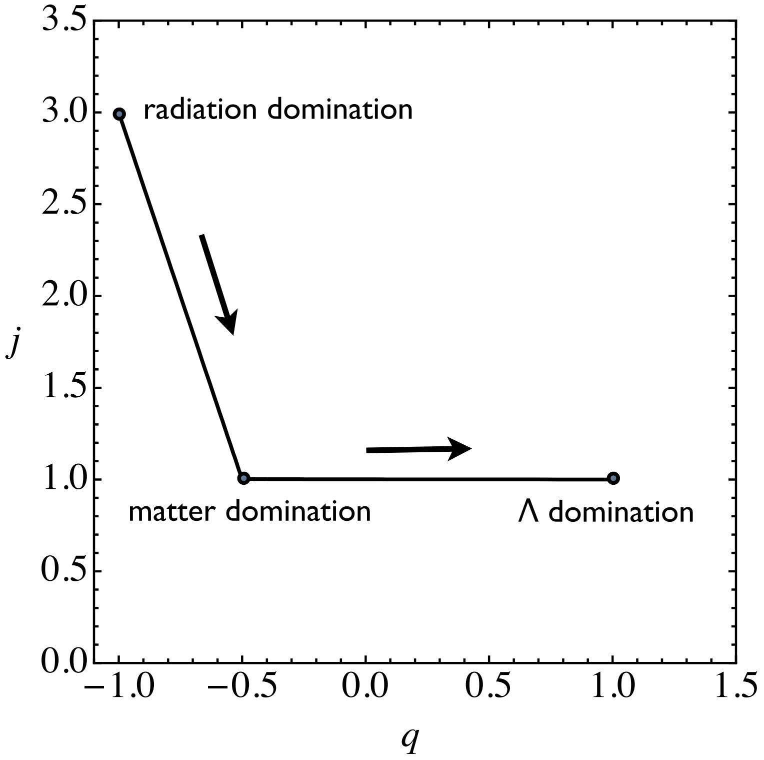

Figure 2.9: In the qj plane the the expansion history of our universe is extremely simple. In the standard model with radiation, cold dark matter and cosmological constant $j = -(1 + 4q)$ when matter and radiation dominate the energy density whereas when matter and the cosmological constant dominate we have $j = 1$.

a universe with cold dark matter and cosmological constant as the dominant energy densities,

$$j = 1 \tag{2.49}$$

When radiation ($P_r = \rho_r/3$) and cold dark matter dominate the energy densities we get

$$j = -(1 + 4q) \tag{2.50}$$

The jerk starts out at $j = 3$ deep in the radiation era, approaches $j = 1$ as matter domination approaches. The expansion of our universe looks simplest in the qj plane shown in the Figure 2.9. The points $(q, j) = (-1, 3)$, $(q, j) = (-1/2, 1)$ and

$(q, j) = (1, 1)$ correspond to radiation, matter and cosmological constant domination respectively. It is worth noting that the jerk parameter: $j = 1$ in any era when the effective pressure in our universe is constant with time. If one considers a slightly more general (but arbitrary) model for dark energy with $P_w = w\rho_w$ with constant w, then we get $j = -\frac{1}{2}(1 + 3w) - 3q(1 + w)$. Adding more components usually lead to more complicated relations between the kinematic variables.

2.C.3 Step-kinematics

Let us take a more detailed view of the kinematic variables in a spatially flat universe filled with radiation, cold-dark matter and a cosmological constant. For the standard model, we have

$$\frac{H^2}{H_0^2} = 1 - \Omega_m - \Omega_r + \Omega_m a^{-3} + \Omega_r a^{-4}, \tag{2.51}$$

where $\Omega_i = \rho_i/\rho_c$ are the contemporary Russian density parameters with ρ_c being the critical density. From the above equation we can solve for the scale factor $a(H_0 t; \Omega_i)$. For the scale factor $a(H_0 t; \Omega_i)$ obtained from [2.51], we can construct $u_n(H_0 t; \Omega_i)$. It is instructive to plot these dimensionless kinematic parameters as a function of the scale factor a rather than $H_0 t$. Figure 2.10. shows $u_2(a)$, $u_3(a)$ and $u_4(a)$ (ie. $q(a)$, $j(a)$ and $s(a)$) as our universe evolves from a radiation dominated era to a cosmological constant dominated era via a matter dominated era. Note the step like behavior in the kinematic parameters. We shall concentrate on three features of these kinematic steps: (i) The height (ii) location of transition (iii) rate of transition. We will restrict our attention to two kinematic variable $u_2 = q$ and $u_3 = j$. Let us first look at the height of the steps. For $a \gg 1$, the expansion rate is dominated by the cosmological constant. In this era the scale factor has an exponential dependence on time which yields $u_n(a) = 1$. As discussed before, for any era with a power law scale factor, $u_n(a) = \textit{constant}$. Specifically, during matter domination we have

$$a(t) \propto t^{2/3} \Longrightarrow u_2(a) = q(a) = -\frac{1}{2}, \qquad u_3(a) = j(a) = 1, \tag{2.52}$$

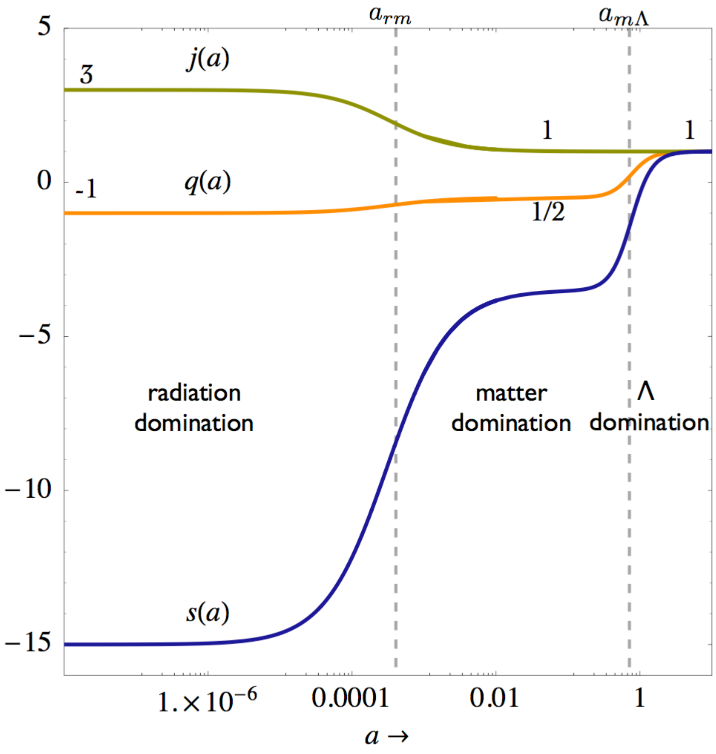

Figure 2.10: The evolution of kinematic variables as a function of scale factor a for a spatially flat universe with radiation, matter and a cosmological constant. For any era with a power law scale factor $a(t) \propto t^{\beta}$, the kinematic variables $u_n(t) = a^{(n)}(t)a^{n-1}(t)/\dot{a}^n(t)$, $(n \geq 2)$ are constants. During radiation domination $a(t) \propto t^{1/2}$ and we have $[u_2(a), u_3(a), u_4(a)] = [q(a), j(a), s(a)] = [-1, 3, -15]$ whereas during matter domination $a(t) \propto t^{2/3}$ which yields $[u_2(a), u_3(a), u_4(a)] = [q(a), j(a), s(a)] = [-1/2, 1, -7/2]$. For the de-Sitter era $(a \gg 1)$ we have an exponential scale factor which yields $u_n(a) = 1$ for all n, all the kinematic variables asymptode to one. In the above plot we have taken $\Omega_m = 0.3, \Omega_r = 10^{-4}$ which determine the location of the transitions. At the radiation matter transition $dq/d\ln a = 1/8$ and $dj/d\ln a = -1/2$ while at the matter dark energy transition we have $dq/d\ln a = 9/8$ and $dj/d\ln a = 0$

while during radiation era

$$a(t) \propto t^{1/2} \Longrightarrow u_2(a) = q(a) = -1, \qquad u_3(a) = j(a) = 3, \tag{2.53}$$

The value of the scale factor where the transitions occur are determined by the Ω_i or the energy densities of the different components. At radiation matter equality the transition rates are

$$\left.\frac{dq}{d\ln a}\right|_{a=a_{rm}} = \frac{1}{8}, \qquad \left.\frac{dj}{d\ln a}\right|_{a=a_{rm}} = -\frac{1}{2}, \tag{2.54}$$

whereas at matter-Λ equality

$$\left.\frac{dq}{d\ln a}\right|_{a=a_{m\Lambda}} = \frac{9}{8}, \qquad \left.\frac{dj}{d\ln a}\right|_{a=a_{m\Lambda}} = 0. \tag{2.55}$$

Possible applications

The step like behavior suggests many simple ways of constructing departures from the standard model. Although we do not go into details here, a simple approach would be to use parameters that control the height of the steps, the location of the transition and the rate of the transition. Most dark energy models in the current literature can be described (at least to a good approximation) by such a parameterization.

2.C.4 Reconstruction

Finally, we provide a taste of how kinematic variables can be related to relevant features of an unknown component responsible for cosmic acceleration. For example, if it is assumed that quintessence is responsible for cosmic acceleration, then we can reconstruct it from the kinematic variables as follows

$$\begin{aligned} \dot{\phi}^2 &= -\rho_c \left(\frac{2}{3}\frac{H^2}{H_0^2}(q-1) + \Omega_m a^{-3} \right), \\ V &= \rho_c \left(\frac{1}{3}\frac{H^2}{H_0^2}(2+q) - \frac{1}{2}\Omega_m a^{-3} \right). \end{aligned} \tag{2.56}$$

Using the above expression, one can easily relate the kinematic variables and the effective equation of state parameter:

$$w = \frac{\dot{\phi}^2/2 - V}{\dot{\phi}^2/2 + V} = -\frac{1}{3}\frac{(1+2q)}{1 - \Omega_m a^{-3}(H_0/H)^2}.$$

Similarly, it is also possible to reconstruct relevant "potentials" in modified gravity models from the expansion history. In general, the problem is not that we can find a model that fits a given expansion history, but the fact that we can find too many (though none have a strong theoretical basis). One way of alleviating this problem is to include information from the inhomogeneous universe. This is pursued in the next chapter.

Bibliography 2

[1] R. D. Blandford, Mustafa Amin, E. A. Baltz, K. Mandel, and P. J. Marshall. "cosmokinetics". In *ASP Conf. Ser. 339, 27, "Observing Dark Energy", astro-ph/0408279*, 2004.

[2] D. N. Spergel et al. First-Year Wilkinson Microwave Anisotropy Probe (WMAP) Observations: Determination of Cosmological Parameters. *ApJ S.*, 148:175–194, sep 2003.

[3] D. N. Spergel et al. Wilkinson microwave anisotropy probe (wmap) three year results: Implications for cosmology. *astro-ph/0603449*, 2006.

[4] A. G. Riess et al. Observational Evidence from Supernovae for an Accelerating Universe and a Cosmological Constant. *ApJ*, 116:1009, 1998.

[5] S. Perlmutter et al. Measurements of omega and lambda from 42 high-redshift supernovae. *ApJ*, 517:565, 1999.

[6] R. A. Knop et al. New Constraints on Ω_M, Ω_Λ, and w from an Independent Set of 11 High-Redshift Supernovae Observed with the Hubble Space Telescope. *ApJ*, 598:102–137, November 2003.

[7] A. G. Riess et al. Type Ia Supernova Discoveries at $z > 1$ from the Hubble Space Telescope: Evidence for Past Deceleration and Constraints on Dark Energy Evolution. *ApJ*, 607:665–687, June 2004.

[8] P. Astier et al. The Supernova Legacy Survey: Measurement of $Omega_M$, Ω_Λ and w from the First Year Data Set. *astro-ph/0510447*, oct 2005.

[9] S. W. Allen, R. W. Schmidt, and A. C. Fabian. Cosmological constraints from the X-ray gas mass fraction in relaxed lensing clusters observed with Chandra. *MNRAS*, 334:L11–L15, August 2002.

[10] S. W. Allen, R. W. Schmidt, H. Ebeling, A. C. Fabian, and L. van Speybroeck. Constraints on dark energy from Chandra observations of the largest relaxed galaxy clusters. *MNRAS*, 353:457, July 2004.

[11] S. Ettori, P. Tozzi, and P. Rosati. Constraining the cosmological parameters with the gas mass fraction in local and $z > 0.7$ galaxy clusters. *Astron. Astrophys.*, 398:879–890, 2003.

[12] S. Borgani, P. Rosati, P. Tozzi, S. A. Stanford, P. R. Eisenhardt, C. Lidman, B. Holden, R. Della Ceca, C. Norman, and G. Squires. Measuring Ω_m with the ROSAT Deep Cluster Survey. *ApJ*, 561:13–21, November 2001.

[13] S. W. Allen, R. W. Schmidt, A. C. Fabian, and H. Ebeling. Cosmological constraints from the local X-ray luminosity function of the most X-ray-luminous galaxy clusters. *MNRAS*, 342:287–298, June 2003.

[14] T. H. Reiprich and H. Böhringer. The Mass Function of an X-Ray Flux-limited Sample of Galaxy Clusters. *ApJ*, 567:716–740, March 2002.

[15] Peter Schuecker, Robert R. Caldwell, Hans Bohringer, Chris A. Collins, and Luigi Guzzo. Observational constraints on general relativistic energy conditions, cosmic matter density and dark energy from x- ray clusters of galaxies and type-ia supernovae. *Astron. Astrophys.*, 402:53–64, 2003.

[16] A. Voevodkin and Alexey Vikhlinin. Constraining amplitude and slope of the mass fluctuation spectrum using cluster baryon mass function. *ApJ*, 601:610–620, 2004.

[17] Max Tegmark et al. Cosmological parameters from sdss and wmap. *Phys. Rev.*, D69:103501, 2004.

[18] Shaun Cole et al. The 2df galaxy redshift survey: Power-spectrum analysis of the final dataset and cosmological implications. *MNRAS*, 362:505–534, 2005.

[19] Daniel J. Eisenstein et al. Detection of the baryon acoustic peak in the large-scale correlation function of sdss luminous red galaxies. *ApJ*, 633:560–574, 2005.

[20] Rupert A. C. Croft et al. Towards a precise measurement of matter clustering: Lyman- alpha forest data at redshifts 2-4. *ApJ*, 581:20–52, 2002.

[21] Matteo Viel, Jochen Weller, and Martin Haehnelt. Constraints on the primordial power spectrum from high resolution lyman-alpha forest spectra and wmap. *MNRAS*, 355:L23, 2004.

[22] Uros Seljak et al. Cosmological parameter analysis including sdss ly-alpha forest and galaxy bias: Constraints on the primordial spectrum of fluctuations, neutrino mass, and dark energy. *Phys. Rev.*, D71:103515, 2005.

[23] Ludovic van Waerbeke et al. Detection of correlated galaxy ellipticities on cfht data: first evidence for gravitational lensing by large-scale structures. *Astron. Astrophys.*, 358:30–44, 2000.

[24] Henk Hoekstra, Howard K. C. Yee, and Mike D. Gladders. Constraints on ω_m and σ_8 from weak lensing in rcs fields. *ApJ*, 577:595–603, 2002.

[25] L. Van Waerbeke, Y. Mellier, and H. Hoekstra. Dealing with systematics in cosmic shear studies: New results from the VIRMOS-Descart survey. *Astron. Astrophys.*, 429:75–84, January 2005.

[26] M. Jarvis, B. Jain, G. Bernstein, and D. Dolney. Dark Energy Constraints from the CTIO Lensing Survey. *astro-ph/0502243*, February 2005.

[27] R. Scranton et al. Physical Evidence for Dark Energy. *astro-ph/0307335*, July 2003.

[28] Pablo Fosalba, Enrique Gaztanaga, and Francisco Castander. Detection of the isw and sz effects from the cmb-galaxy correlation. *ApJ*, 597:L89–92, 2003.

[29] R.R. Caldwell, R. Dave, and P.J. Steinhardt. *Phys. Rev. Lett.*, 80:1582, 1998.

[30] Ivaylo Zlatev, Li-Min Wang, and Paul J. Steinhardt. Quintessence, cosmic coincidence, and the cosmological constant. *Phys. Rev. Lett.*, 82:896–899, 1999.

[31] Edmund J. Copeland, Andrew R Liddle, and David Wands. Exponential potentials and cosmological scaling solutions. *Phys. Rev.*, D57:4686–4690, 1998.

[32] Paul J. Steinhardt, Li-Min Wang, and Ivaylo Zlatev. Cosmological tracking solutions. *Phys. Rev.*, D59:123504, 1999.

[33] T. Barreiro, Edmund J. Copeland, and N. J. Nunes. Quintessence arising from exponential potentials. *Phys. Rev.*, D61:127301, 2000.

[34] Takeshi Chiba, Takahiro Okabe, and Masahide Yamaguchi. Kinetically driven quintessence. *Phys. Rev.*, D62:023511, 2000.

[35] C. Armendariz-Picon, V. Mukhanov, and Paul J. Steinhardt. A dynamical solution to the problem of a small cosmological constant and late-time cosmic acceleration. *Phys. Rev. Lett.*, 85:4438–4441, 2000.

[36] C. Armendariz-Picon, V. Mukhanov, and Paul J. Steinhardt. Essentials of k-essence. *Phys. Rev.*, D63:103510, 2001.

[37] J. S. Bagla, Harvinder Kaur Jassal, and T. Padmanabhan. Cosmology with tachyon field as dark energy. *Phys. Rev.*, D67:063504, 2003.

[38] Edmund J. Copeland, Mohammad R. Garousi, M. Sami, and Shinji Tsujikawa. What is needed of a tachyon if it is to be the dark energy? *Phys. Rev.*, D71:043003, 2005.

[39] Alexander Yu. Kamenshchik, Ugo Moschella, and Vincent Pasquier. An alternative to quintessence. *Phys. Lett.*, B511:265–268, 2001.

[40] M. C. Bento, O. Bertolami, and A. A. Sen. Generalized chaplygin gas, accelerated expansion and dark energy-matter unification. *Phys. Rev.*, D66:043507, 2002.

[41] G. R. Dvali, Gregory Gabadadze, and Massimo Porrati. 4d gravity on a brane in 5d minkowski space. *Phys. Lett.*, B485:208–214, 2000.

[42] C. Deffayet, G. Dvali, and G. Gabadadze. Accelerated universe from gravity leaking to extra dimensions. *Phys. Rev.D*, 65(4):044023–+, February 2002.

[43] Cedric Deffayet, Susana J. Landau, Julien Raux, Matias Zaldarriaga, and Pierre Astier. Supernovae, cmb, and gravitational leakage into extra dimensions. *Phys. Rev.*, D66:024019, 2002.

[44] Roy Maartens and Elisabetta Majerotto. Observational constraints on self-accelerating cosmology. *astro-ph/0603353*, 2006.

[45] Zong-Kuan Guo, Zong-Hong Zhu, J. S. Alcaniz, and Yuan-Zhong Zhang. Constraints on the dgp model from recent supernova observations and baryon acoustic oscillations. *astro-ph/0603632*, 2006.

[46] S. Capozziello, S. Carloni, and A. Troisi. Quintessence without scalar fields. *astro-ph/0303041*, March 2003.

[47] Sean M. Carroll, Vikram Duvvuri, Mark Trodden, and Michael S. Turner. Is cosmic speed-up due to new gravitational physics? *Phys. Rev.*, D70:043528, 2004.

[48] Dan N. Vollick. Curvature corrections as the source of the cosmological acceleration. *Phys. Rev.*, D68:063510, 2003.

[49] Sean M. Carroll et al. The cosmology of generalized modified gravity models. *Phys. Rev.*, D71:063513, 2005.

[50] Olga Mena, Jose Santiago, and Jochen Weller. Constraining inverse curvature gravity with supernovae. *Phys. Rev. Lett.*, 96:041103, 2006.

[51] Ignacio Navarro and Karel Van Acoleyen. Modified gravity, dark energy and mond. *gr-qc/0512109*, 2005.

[52] Shin'ichi Nojiri and Sergei D. Odintsov. Introduction to modified gravity and gravitational alternative for dark energy. *hep-th/0601213*, 2006.

[53] Charles Shapiro and Michael S. Turner. What do we really know about cosmic acceleration? *astro-ph/0512586*, 2005.

[54] Y. Gong and A. Wang. Observational constraints on the acceleration of the Universe. *astro-ph/0601453*, January 2006.

[55] Oystein Elgaroy and Tuomas Multamaki. Bayesian analysis of friedmannless cosmologies. *astro-ph/0603053*, 2006.

[56] S. W. Allen et al. . *in preparation*, 2007.

[57] Varun Sahni, Tarun Deep Saini, Alexei A. Starobinsky, and Ujjaini Alam. Statefinder – a new geometrical diagnostic of dark energy. *JETP Lett.*, 77:201–206, 2003.

[58] Ujjaini Alam, Varun Sahni, Tarun Deep Saini, and A. A. Starobinsky. Exploring the expanding universe and dark energy using the statefinder diagnostic. *MNRAS*, 344:1057, 2003.

[59] Takeshi Chiba and Takashi Nakamura. The luminosity distance, the equation of state, and the geometry of the universe. *Prog. Theor. Phys.*, 100:1077–1082, 1998.

[60] Robert R. Caldwell and Marc Kamionkowski. Expansion, geometry, and gravity. *JCAP*, 0409:009, 2004.

[61] Edmund J. Copeland, M. Sami, and Shinji Tsujikawa. Dynamics of dark energy. *hep-th/0603057*, 2006.

[62] Matt Visser. Jerk and the cosmological equation of state. *Class. Quant. Grav.*, 21:2603–2616, 2004.

[63] Eric V. Linder. The paths of quintessence. *Phys. Rev.*, D73:063010, 2006.

[64] Sean M. Carroll, Mark Hoffman, and Mark Trodden. Can the dark energy equation-of-state parameter w be less than -1? *Phys. Rev.*, D68:023509, 2003.

[65] V. K. Onemli and R. P. Woodard. Quantum effects can render w ¡ -1 on cosmological scales. *Phys. Rev.*, D70:107301, 2004.

[66] Wayne Hu. Crossing the phantom divide: Dark energy internal degrees of freedom. *Phys. Rev.*, D71:047301, 2005.

[67] Alexander Vikman. Can dark energy evolve to the phantom? *Phys. Rev.*, D71:023515, 2005.

[68] Robert R. Caldwell and Michael Doran. Dark-energy evolution across the cosmological-constant boundary. *Phys. Rev.*, D72:043527, 2005.

[69] Gong-Bo Zhao, Jun-Qing Xia, Mingzhe Li, Bo Feng, and Xinmin Zhang. Perturbations of the quintom models of dark energy and the effects on observations. *Phys. Rev.*, D72:123515, 2005.

[70] J. Weller and A. M. Lewis. Large-scale cosmic microwave background anisotropies and dark energy. *MNRAS*, 346:987–993, dec 2003.

[71] A. Cabre, E. Gaztanaga, M. Manera, P. Fosalba, and F. Castander. Cross-correlation of wmap 3rd year and the sdss dr4 galaxy survey: new evidence for dark energy. *astro-ph/0603690*, 2006.

[72] H. K. Jassal, J. S. Bagla, and T. Padmanabhan. Wmap constraints on low redshift evolution of dark energy. *MNRAS*, 356:L11–L16, 2005.

[73] P. S. Corasaniti, M. Kunz, D. Parkinson, E. J. Copeland, and B. A. Bassett. The foundations of observing dark energy dynamics with the Wilkinson Microwave Anisotropy Probe. *Phys. Rev.*, D70:083006, 2004.

[74] D. Rapetti, S. W. Allen, and J. Weller. Constraining dark energy with x-ray galaxy clusters, supernovae and the cosmic microwave background. *MNRAS*, 360:555–564, june 2005.

[75] Amol Upadhye, Mustapha Ishak, and Paul J. Steinhardt. Dynamical dark energy: Current constraints and forecasts. *Phys. Rev.*, D72:063501, 2005.

[76] Gong-Bo Zhao, Jun-Qing Xia, Bo Feng, and Xinmin Zhang. Probing dynamics of dark energy with supernova, galaxy clustering and the three-year wilkinson microwave anisotropy probe (wmap) observations. *astro-ph/0603621*, 2006.

[77] M. A. Amin and R. D. Blandford. . *in preparation*, 2007.

[78] S. Nesseris and Leandros Perivolaropoulos. Comparison of the legacy and gold snia dataset constraints on dark energy models. *Phys. Rev.*, D72:123519, 2005.

[79] W.L. Freedman et al. Final results from the Hubble Space Telescope key project to measure the Hubble constant. *ApJ*, 553:47, 2001.

[80] D. Kirkman, D. Tytler, N. Suzuki, J. M. O'Meara, and D. Lubin. The Cosmological Baryon Density from the Deuterium-to-Hydrogen Ratio in QSO Absorption Systems: D/H toward Q1243+3047. *ApJ S.*, 149:1–28, nov 2003.

[81] Vincent R. Eke, Julio F. Navarro, and Carlos S. Frenk. The evolution of x-ray clusters in low density universes. *ApJ*, 503:569, 1998.

[82] A. Lewis and S. Bridle. Cosmological parameters from CMB and other data: a Monte-Carlo approach. *Phys. Rev.*, D66:103511, 2002.

[83] A. Gelman and D. B. Rubin. Inference from iterative simulation using multiple sequences. *Statis. Sci.*, 7:457–511, 1992.

[84] G. Schwarz. *Ann. Stat.*, 6:461, 1978.

[85] H. Jeffreys. *Theory of probability.* Oxford Univ. Press, Oxford, 1961.

[86] R. E. Kass and A. E. Raftery. *J. Am. Stat. Assn.*, 90:773, 1995.

[87] S. Mukherjee, E. D. Feigelson, G. Jogesh Babu, F. Murtagh, C. Fraley, and A. Raftery. Three Types of Gamma-Ray Bursts. *ApJ*, 508:314–327, November 1998.

[88] Andrew R. Liddle. How many cosmological parameters? *MNRAS*, 351:L49–L53, 2004.

[89] Licia Verde et al. First year wilkinson microwave anisotropy probe (wmap) observations: Parameter estimation methodology. *ApJ S.*, 148:195, 2003.

[90] J. C. Mather, D. J. Fixsen, R. A. Shafer, C. Mosier, and D. T. Wilkinson. Calibrator Design for the COBE Far-Infrared Absolute Spectrophotometer (FIRAS). *ApJ*, 512:511–520, February 1999.

[91] G. Hinshaw et al. Three-year wilkinson microwave anisotropy probe (wmap) observations: Temperature analysis. *astro-ph/0603451*, 2006.

[92] Michael Doran and Matthew Lilley. The location of cmb peaks in a universe with dark energy. *MNRAS*, 330:965–970, 2002.

[93] William H. Kinney. Inflation: Flow, fixed points and observables to arbitrary order in slow roll. *Phys. Rev.*, D66:083508, 2002.

[94] Dragan Huterer and Eric V. Linder. Separating dark physics from physical darkness: Minimalist modified gravity vs. dark energy. *Phys. Rev.*, D75:023519, 2007.

Chapter 3

A framework for probing gravity on cosmological scales

Mustafa A. Amin, Robert V. Wagoner and Roger D. Blandford

KIPAC/Department of Physics, Stanford University, CA 94305, USA

accepted for publication in Mon. Not. Roy. Astron. Soc. [arXiv:0708.1793v2].

Abstract The relationship between the metric and nonrelativistic matter distribution depends on the theory of gravity and additional fields, hence providing a possible way of distinguishing competing theories. With the assumption that the geometry and kinematics of the homogeneous universe have been measured to sufficient accuracy, we present a procedure for understanding and testing the relationship between the cosmological matter distribution and metric perturbations (along with their respective evolution) using the ratio of the physical size of the perturbation to the size of the horizon as our small expansion parameter. We expand around Newtonian gravity on linear, subhorizon scales with coefficient functions in front of the expansion parameter. Our framework relies on an ansatz which ensures that (i) the Poisson equation is recovered on small scales (ii) the metric variables (and any additional fields) are generated and supported by the nonrelativistic matter overdensity. The scales for which our framework is intended are small enough so that cosmic variance does not significantly limit the accuracy of the measurements and large enough to avoid complications due to nonlinear effects and baryon cooling. From a theoretical perspective, the coefficient functions provide a general framework for contrasting the consequences of ΛCDM and its

alternatives. We calculate the coefficient functions for general relativity (GR) with a cosmological constant and dark matter, GR with dark matter and quintessence, scalar-tensor theories (STT), $f(R)$ gravity and braneworld (DGP) models. We identify a possibly unique signature of braneworld models. For observers, constraining the coefficient functions provides a streamlined approach for testing gravity in a scale dependent manner. We briefly discuss the observations best suited for an application of our framework.

3.1 Introduction

A successful model of the universe must include a background geometry, an inventory of its contents, a kinematical description of its expansion and a dynamical explanation of how its constituents interact, drive the expansion and develop structure. Recent observations (for example [1, 2, 3, 4, 5, 6, 7, 8, 9, 26, 11, 12, 13, 14] and references therein) have led to a "Flat ΛCDM cosmology" (henceforth FΛCDM), dominated by dark energy (cosmological constant Λ) and matter (predominately dark and initially cold) and the observed expansion rate and growth of structure agree with the predictions of this model at the ten percent level. Future observations should be capable of testing this model at the one percent level. If they verify its predictions, they will affirm a remarkable, simple description of the universe, implicit in the earliest relativistic investigations of Einstein, Friedmann and Lemaître, analogous to the affirmation of general relativity (GR) that took place twenty years ago (for example [15]). If FΛCDM passes this test, then the challenge will be to account for this outcome in terms of physical processes operating at earlier epochs; if it fails, then we shall either have learned something important about gravitational physics or described a new, dominant component of the universe. Many alternatives, with and without GR, to FΛCDM have been proposed. At this stage, none of them stands out. There is therefore a need to provide a framework for describing future observations and theoretical investigations in general terms which will facilitate a distinction between FΛCDM and its alternatives. The provision of one such framework is the goal of this paper.

Further observational progress is anticipated over the coming decade. The analysis of Planck observations [16] of the microwave background, coupled with local measurements of the contemporary Hubble parameter, H_0, should result in an extremely accurate description of the physical conditions and the statistical properties of the density fluctuation spectrum at the epoch of recombination when the universe had a scale factor $a \equiv (1+z)^{-1} \sim 10^{-3}$ relative to today. Combining the calculated physical sizes of the acoustic peaks in the background radiation spectrum with the Hubble constant and the Copernican Principle leads to a measurement of spatial curvature, which is already known to contribute to the kinematics at a level of less than a few percent [14]. We shall adopt a value of zero for illustration purposes. Essentially kinematic measurements, for example, those involving Type Ia supernova explosions, baryonic acoustic oscillations (BAO) and baryonic gas fractions in clusters should provide a record of the comoving distance, $d(a) = \int c dt/a$, from which the evolution of the Hubble parameter $H(a) = d\ln a/dt$ and the acceleration parameter $q(a) = d\ln(Ha)/d\ln a$ can be inferred[1]. For the rest of the paper we shall assume that these evolutions have been measured to a sufficient accuracy. Note that we are using a instead of the cosmic time t as the time coordinate as this relates directly to the observable photon frequency shift. For recent constraints on the expansion history, see for example [17] and references therein.

Given an understanding of the geometry and kinematics, the task is then to see if the dynamical evolution of the universe is consistent with GR or mandates an alternative theory. Now, GR provides a relationship between the spacetime geometry on a cosmological scale measured by the Einstein tensor $\mathbf{G}[g_{\mu\nu}]$ and the total Energy-Momentum Tensor (EMT) of its contents $\mathbf{T}$, $\mathbf{G}[g_{\mu\nu}] = 8\pi G\mathbf{T}$. The discovery that $\mathbf{G}[g_{\mu\nu}] \neq 8\pi G\mathbf{T}[\text{“obs”}]$ where $\mathbf{T}[\text{“obs”}]$ includes known forms of matter such as electromagnetic radiation, baryons etc. has led to the addition of dark matter and dark energy contributions to the EMT. Dark matter candidates include Weakly Interacting Massive Particles and axions which would presumably behave gravitationally like baryonic matter. However other possibilities exist which might behave differently such as massive neutrinos (as a subdominant component). Dark energy is most simply characterized as a temporaily and spatially constant vacuum energy field with zero enthalpy (see [18] for a review). However, it could also have quite different dynamical properties and might include contributions from additional scalar [19], vector [20] or tensor fields with possible interactions between each other [21] and with known forms of matter. Historically, the first representation of dark energy was Einstein's cosmological constant, which was seen as an augmentation to $\mathbf{G}$, not $\mathbf{T}$ (see for example [22]). This original proposal has also been generalized in many ways so that $\mathbf{G}[g_{\mu\nu}] + \mathbf{F}[g_{\mu\nu}, \varphi] = 8\pi G\mathbf{T}[\text{“obs”}]$, where $\mathbf{F}[g_{\mu\nu}, \varphi]$ depends on the metric and

---

[1] Our acceleration parameter differs from the conventional deceleration parameter by a minus sign.

more generally some additional gravitational fields, φ. For example φ could be the additional gravitational scalar field in Scalar-Tensor Theories (STT) (see for example [23, 24]). Nature could of course be unkind and we might have

$$\mathbf{G}[g_{\mu\nu}] + \mathbf{F}[g_{\mu\nu}, \varphi] = 8\pi G\mathbf{T}[\text{“obs”}] + 8\pi G\mathbf{T}[\text{“dark”}]. \tag{3.1}$$

Considerable effort has been made in constructing models that fall into the above mentioned categories and more recently in finding ways to distinguish between them (for example see [25, 26, 27, 28, 29]).

Now, modifying the physics beyond GR with cold dark matter and Λ can have three quite separate manifestations. Firstly it can lead to a change in expansion of the universe, secondly, it can influence the growth of structure and the metric and thirdly, it can confront local tests of the theory of gravity. The approach that we follow is to assume that the theory is constrained by the first and third manifestations and that it is the growth of structure that is providing the test. This oversimplifies the data analysis but does lead to a transparent and simple approach. One important consequence of adopting local gravitational tests is that photons and baryons, at least, will follow geodesics and that the unperturbed photons will be subject to cosmological redshifting of their frequencies, $\nu \propto a^{-1}$. This simplifies the interpretation of observational data.

Our procedure is to adopt a general form for the metric of a linearly perturbed homogeneous and isotropic universe which introduces two potentials $\Phi(\mathbf{x}, a)$ and $\Psi(\mathbf{x}, a)$ (scalar metric perturbations in the Newtonian gauge), where $\mathbf{x}$ denotes the three spatial coordinates. We also introduce an associated fractional density perturbation $\delta_m(\mathbf{x}, a)$ in nonrelativistic matter and relate it to the potentials. We assume that there is a dominant nonbaryonic contribution to the clustering of nonrelativistic matter. In practice, it is easier to work with Fourier modes and this allows us to focus attention on the range of length scales that are most relevant observationally: sufficiently smaller than the horizon so that our expansion is valid and we can observe enough independent volumes within our current horizon allowing for a high precision measurement despite “cosmic variance”, and yet large enough that nonlinear effects and baryonic cooling are not a factor. Within this range of length scales, we adopt the following ansatz regarding the relationship between linearized metric and density perturbations, written as an expansion in powers of (aH/k), where k is the magnitude of the comoving wavevector $\mathbf{k}$

$$\begin{aligned}
\Phi(\mathbf{k},a) &= -\frac{4\pi G\rho_m}{H^2}\left(\frac{aH}{k}\right)^2 \delta_m(\mathbf{k},a)\left[\beta_0(a)+\beta_1(a)\left(\frac{aH}{k}\right)+\beta_2(a)\left(\frac{aH}{k}\right)^2+\dots\right]\\
\Psi(\mathbf{k},a) &= -\frac{4\pi G\rho_m}{H^2}\left(\frac{aH}{k}\right)^2 \delta_m(\mathbf{k},a)\left[\gamma_0(a)+\gamma_1(a)\left(\frac{aH}{k}\right)+\gamma_2(a)\left(\frac{aH}{k}\right)^2+\dots\right]\\
\delta_m(\mathbf{k},a) &= \delta_{mi}(\mathbf{k})\left[\delta_0(a)+\delta_1(a)\left(\frac{aH}{k}\right)+\delta_2(a)\left(\frac{aH}{k}\right)^2+\dots\right]
\end{aligned} \tag{3.2}$$

We have set the speed of light $c = 1$. The background mass density $\rho_m \propto a^{-3}$. $\delta_{mi}(\mathbf{k})$ is determined from initial conditions which can in principle be taken close to the surface of last scattering, $a_i \sim 10^{-3}$, as long as the modes are sufficiently sub-horizon. Note that often, we are only interested in the scale dependence of the growth of the perturbations in the matter distribution and the metric at linear, subhorizon scales. Such measurements require taking ratios of the matter distribution or the metric at different redshifts, whereby, the initial conditions cancel out in the final expressions. The coefficient functions $\{\beta_n, \gamma_n, \delta_n\}$ with $n = 0, 1, 2$ are arbitrary functions of the scale factor. The leading terms in the expansion agree with Poisson's equation on small scales, while subsequent terms allow for a scale-dependent departure as we move towards larger scales. This approach introduces a length-scale dependence to the perturbations through an expansion in powers of $(GM/d_p)^{1/2} \sim d_P/d_H$, where $M \sim \rho_m d_p^3$ is the total mass enclosed within the physical size d_p and $d_H \equiv 1/H$ is the Hubble horizon. In Fourier space, with $d_p \sim a/k$, we get $(GM/d_p)^{1/2} \sim aH/k$.

The theories that we discuss below introduce different corrections (different coefficient functions $\{\beta_n, \gamma_n, \delta_n\}$) and these differences are measurable[2] . From an observer's perspective, constraining the coefficient functions with measurents of Φ, Ψ and δ_m provides a streamlined approach to characterizing gravity on cosmological scales in a scale dependent manner. On the other hand, from a theorist's perspective, substituting the ansatz into the field equations for a given theory allows for a (mostly straightforward) calculation of the coefficient functions. The coefficient functions provide a means of comparing the consequences of different theories. We shall discuss our assumptions, limitations and our ansatz in detail in the next section.

This is certainly not the first time that an attempt at constructing and applying such a framework has been made. The Parametrized Post Newtonian formalism (see [15] and references therein) has been a powerful framework for understanding and constraining gravity on solar system (and other isolated system) scales. Our aim is to construct a similar framework for cosmological scales. Recently a few attempts have been made in this direction. However most of these are either concerned with the expansion history alone, deal with specific aspects of departures from GR such as effective gravitational constant on small scales [30], growth of perturbations on small scales [31], the gravitational slip [32], or deal with superhorizon scales [33]. The authors in [34] take into account growth of structure, anisotropic stress and the modification to the Poisson equation and parametrize departures from Einstein's gravity with a growth index and two functions of the scale factor which are relevant for weak lensing surveys. However, they do not consider scale dependent departures. Another popular phenomenological approach for characterizing the effects of the unknown physics (additional fields, their interactions, or modified gravitational laws) is to define an effective fluid energy momentum tensor for everything other than the standard model matter, effectively move $\mathbf{F}$ in equation (3.1) to the right hand side and define $\mathbf{T}_{eff} = -(8\pi G)^{-1}\mathbf{F}[\varphi, g_{\mu\nu}] + \mathbf{T}[\text{“dark”}]$. This effective energy momentum

---

[2] As we shall see at the end of Section 2 and in Section 3, the coefficients $\beta_2, \gamma_2, \delta_2 \neq 0$ even in GR with non-relativistic matter and represent “post-Newtonian” corrections. Also note that δ_m characterizes the fractional matter density perturbation in the Newtonian gauge, which is related to the often used comoving density perturbation Δ_m through $\Delta_m = \delta_m + 3a\partial_a(\delta_m - 3\Psi)(aH/k)^2$. A combination of the 00 and 0i Einstein equations yields $(k/aH)^2\Psi = -(4\pi G\rho_m/H^2)\Delta_m$.

tensor is then parametrized in terms of the equation of state, sound speed, anisotropic stress, etc. [35, 36]. This approach, however, seems to put an unnecessary restriction of a fluid interpretation which might be misleading, especially when the effective dark energy is due to modified gravity or extra dimensions. We are unaware of a systematic approach undertaken where the framework includes a scale *dependent* departure in the relationship between the matter distribution and the metric perturbations along with their respective evolution on cosmological scales up to post-Newtonian order. [3]

The rest of the paper is organized as follows. Section 2 discusses our assumptions and the particular form of the ansatz in detail. In Section 3 we apply our framework to GR, STT, quintessence, $f(R)$ models [18] and DGP gravity [41]. In particular, we calculate the coefficient functions in these theories and comment on our ansatz in the context of these theories. Section 4 is devoted to how our framework might be employed by observers. We briefly discuss the observations that could be used to constrain the different coefficient functions. Section 5 presents a short summary and future directions for extending the framework.

3.2 Our ansatz and associated assumptions

With an eye towards observations in the next decade, we assume that the geometry (spatial curvature) and kinematics (expansion history) of the universe have been measured to a percent level accuracy. What remains to be understood and measured accurately (at the few percent level) is the relationship between the metric fluctuations and the nonrelativistic matter distribution along with their respective evolution on linear, subhorizon scales. This relationship will depend on the theory of gravity or the presence of yet unknown components, thus providing a test for distinguishing

---

[3] We note that during the final stages of preparation of this this paper we became aware of a scale dependent framework for modified gravity that includes super and sub-horizon scales [37]. After submission of this manuscript, the following were posted on arXiv.org which are relevant to this work. [38] provide an analysis of the observational tests for modified gravity; [39] use evolution of galaxy bias to constrain scale dependent departures from GR; whereas [40] build on [33] to include sub-horizon scales; [37] extend [37] to include multiple fluids and curvature relevant for cosmic microwave background calculations and constraints; whereas [32] discuss the effects of gravitational slip on the CMB, growth of structure, and lensing observations.

different theories. To explore this relationship in an (almost) model independent way, we provide an ansatz, equation (3.2), relating the scalar metric perturbations (in Newtonian gauge) and the nonrelativistic matter overdensity in Fourier space. In this section we discuss the particular form of the ansatz and the underlying assumptions in detail. We introduce our notation and conventions followed by some physical arguments regarding our choice of the particular form of the ansatz. We end with a discussion of the range of scales for which our ansatz is expected to be useful.

We focus on a perturbed FRW universe (spatially flat) with scalar metric fluctuations in the Newtonian gauge [42]. In this gauge the metric takes the following form ($c = 1$)

$$ds^2 = -[1 + 2\Phi(\mathbf{x}, t)]dt^2 + a^2(t)[1 - 2\Psi(\mathbf{x}, t)]d\mathbf{x} \cdot d\mathbf{x}$$

Here the metric perturbations $|\Phi(\mathbf{x}, t)|, |\Psi(\mathbf{x}, t)| \ll 1$. We choose to work in the Newtonian gauge because $\Phi(\mathbf{x}, t)$ is the generalization of the Newtonian gravitational potential and the potentials $\Phi(\mathbf{x}, t)$ and $\Psi(\mathbf{x}, t)$ are gauge invariant Bardeen variables when we specialize to the Newtonian gauge. The energy density perturbation $\delta_m(\mathbf{x}, t)$ is also gauge invariant, corresponding to the energy density perturbation on the zero shear spatial hypersurface which is closest to Newtonian time slicing (see equation (3.14) in [42]). In what follows, we use the scale factor a as the independent variable instead of cosmic time t with $a(\text{today}) = 1$. With this change of variables, the metric takes the form

$$ds^2 = -[1 + 2\Phi(\mathbf{x}, a)](aH)^{-2}da^2 + a^2[1 - 2\Psi(\mathbf{x}, a)]d\mathbf{x} \cdot d\mathbf{x}$$

We shall work primarily in Fourier space and use the following convention: $f(\mathbf{x}, a) = (2\pi)^{-3} \int d^3\mathbf{k} f(\mathbf{k}, a)e^{i\mathbf{k}\cdot\mathbf{x}}$. To avoid unnecessary clutter we write the Fourier transform of the metric perturbations $\Phi(\mathbf{k}, a)e^{i\mathbf{k}\cdot\mathbf{x}}$ as Φ. The same is true for Ψ and δ_m. The background quantities depend on a. We shall often suppress this dependence; for example by H we mean $H(a)$.

We have assumed spatial flatness as expected on the basis of the simplest interpretation of inflation. If the universe has measureable spatial curvature or large scale deviations from the Robertson-Walker assumptions of homogeneity and isotropy, then the following development must be generalized at the expense of introducing parameters that need fitting. A purely geometrical demonstration of spatial flatness would obviate some of this concern. Such a demonstration is possible, in principle, using two screen gravitational lenses (Blandford 2008, in preparation), though it is not known how practical it will be to implement this demonstration. If we choose to include curvature as an additional parameter, then location of the first acoustic peak in the CMB (and BAO scale) would likely provide the best constraints.

Our ansatz provides a relationship between Φ, Ψ and δ_m on linear (in Φ, Ψ and δ_m), subhorizon scales. We now turn to the discussion of some important features of this ansatz. On scales that are much smaller than the size of the horizon, $aH/k \ll 1$, the leading term has the form of a linearised Newtonian gravitational field equation. For the purpose of this paper the Newtonian form of the field equation refers to the the following relation between the time-time metric perturbation $\Phi(\mathbf{x}, a)$ and the nonrelativistic matter density contrast $\delta_m(\mathbf{x}, a)$, $\nabla^2\Phi(\mathbf{x}, a) \propto \delta_m(\mathbf{x}, a)$, which in Fourier space becomes $\Phi \propto (aH/k)^2\delta_m$. Now, in the Newtonian gauge $\Phi(\mathbf{x}, a)$ plays the role of the Newtonian potential once the background has been subtracted out. The proportionality allows for a possible temporal variation in the effective Newton's constant which could depend on the cosmological background evolution.

From GR we know that this Newtonian relation starts breaking down as the size of the perturbation becomes comparable to the size of the horizon. In general, different theories of gravity will introduce different scale dependent departures from this equation, changing the metric-matter relationship. Our claim is that for a large class of theories, our ansatz, equation (3.2), captures the scale dependence of the relationship between the nonrelativistic matter distribution and cosmological metric perturbations. In particular, our ansatz faithfully reproduces the scale dependence of the metric-matter relationship in the fiducial case of GR with cold dark matter and a cosmological constant. In the presence of additional fields one might expect this relationship to break down; however, this is usually not the case. Suppose that an additional field enters the equations, for example as a source (quintessence), as a time varying gravitational constant (Brans Dicke theory) or indirectly encapsulating the effect of higher dimensions, etc. Perturbations $\delta\varphi$ in such a scalar field φ (consider quintessence or scalar-tensor theories) will be involved in the relationship between δ_m and Φ. However, from the field equation for $\delta\varphi$, equations (3.18) and (3.19), we can see that $\delta\varphi \propto \Phi(aH/k)^2$ for quintessence and $\delta\varphi \propto \Phi$ for scalar-tensor theories when $aH/k \ll 1$. Thus, even if additional scalar fields are present, our ansatz should be a good approximation for the relationship between the matter distribution and the metric at the scales of interest. Note that we have assumed $\Psi = \mathcal{O}[\Phi]$ for this argument.

Another feature of our ansatz is that Φ and Ψ are directly proportional to δ_m. This might seem unusual, since it implies that in the absence of nonrelativistic matter perturbations, there would be no metric perturbations. This is certainly not true in principle if an additional scalar field is present. However observationally, we know that nonrelativistic perturbations are present and they dominate over perturbations in other fields. The following argument provides a more detailed justification. Since on the smallest scales, to lowest order in (aH/k), the potential $\Phi \propto \delta_m(aH/k)^2$, we have $\delta\varphi \propto \delta_m(aH/k)^4$ and $\delta\varphi \propto \delta_m(aH/k)^2$ in quintessence models and STT respectively. This means that the potentials and pertubations in other scalar fields are supported by the nonrelativistic matter perturbations. We do not expect to see the effects of the initial power spectrum of these additional fields up to the order of the terms considered in our ansatz, with the initial power spectrum of the additional field possibly playing a role in higher order terms. This is one of the reasons for not extending the power series in aH/k beyond the order considered in the ansatz.

Our ansatz does not capture the matter-metric relationship for all available models in the literature. Consider for example k-essence [43],where the effective "sound speed" (c_s) can be small. This leads to a significant clustering of dark energy on small scales which can be comparable to nonrelativistic matter perturbations. In these scenarios, our ansatz does not provide a good approximation to the full theory. The coefficients $\beta_2, \gamma_2(\propto {c_s}^{-2}) \gg 1$ signaling a breakdown in our assumptions. More generally, if a model introduces an additional physical scale within the range of scales of interest, then care needs to be taken in using our ansatz. In the k-essence example, this additional scale is the Jean's length for the scalar field fluctuations, whereas in the case of $f(R)$ models this could the "Compton wavelength" ($\sim f_{RR}^{-1/2}$) of the effective gravitational scalar degree of freedom (see for example [44]). In such cases the ansatz might still be applicable in a more limited range of parameters and length scales (see Section 3.4).

We note that some of the above arguments are made under the assumption that the additional gravitational or nongravitational contribution to the field equations is due to a scalar field (quintessence or scalar tensor theories). As argued above, this leads to only even powers of aH/k in the expansion. Furthermore, $f(R)$ modification of the Einstein-Hilbert action also lead to even powers of aH/k. An intriguing case where one can get an odd power of aH/k is in DGP braneworld models. In these extra-dimensional theories, the junction conditions on our 4 dimensional brane gives rise to a scale dependence involving terms linear in aH/k. We come back to this in Section 3.5.

Regarding Ψ, we assume that the relationship between Ψ and δ_m has the same (aH/k) dependence as Φ and δ_m since from GR we expect $\Phi = \Psi$ when no anisotropic stress is present. The form of $\delta_m(\mathbf{k}, a)$ in the ansatz can be motivated from the conservation equation for nonrelativistic matter at first order in Φ, Ψ and δ_m:

$$a^2\partial_a^2\delta_m + (2+q)a\partial_a\delta_m = -\left(\frac{k}{aH}\right)^2\Phi + 3\left[a^2\partial_a^2\Psi + (2+q)a\partial_a\Psi\right]. \tag{3.3}$$

As discussed above at lowest order in $(aH/k)^2$, the metric perturbations $\Phi, \Psi \propto \delta_m(aH/k)^2$, thus the largest term on the RHS of equation (3.3) is proportional to $\delta_m(\mathbf{k}, a)$. At this order we get a homogeneous equation for δ_m which has a solution of the form $\delta_m(\mathbf{k}, a) = \delta_{mi}(\mathbf{k})\delta_0(a)$. This is the usual approximation used when investigating the growth function on small scales. Perturbatively including the next order term on the RHS, we can see that our ansatz captures the general form of the solution to that order. Again, we use this argument as motivation for the form of the ansatz, being aware of the fact that nonrelativistic dark matter is not covariantly conserved in some models. In δ_m, we include both baryonic and nonbaryonic dark matter, with an understanding that baryonic matter contibutes a small fraction to the total. We assume that baryons are covariantly conserved and follow timelike geodesics, serving as test particles whose motion can be used to probe the metric.

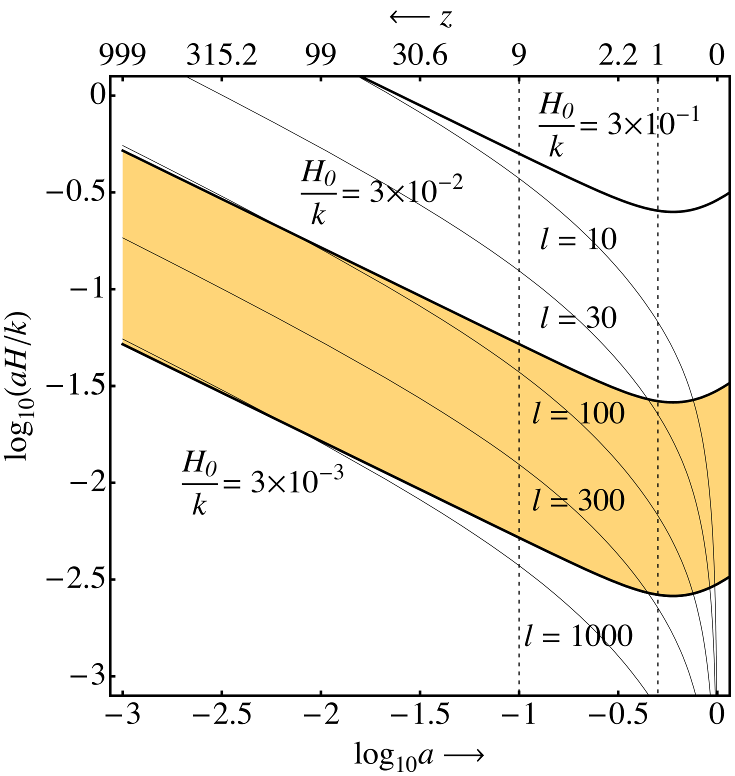

Figure 3.1: The ratio of the physical size of the perturbation to the size of the horizon is used as an expansion parameter in our anzatz. We plot this ratio, (aH/k), as a function of a from last scattering to the present for the concordance model (yellow region). The upper and lower bounds of the yellow region are determined by considering scales that are small enough so that cosmic variance does not dominate the errors and at the same time large enough so that nonlinear evolution and baryon cooling are not a significant factor. Most of the observations in the next decade will yield information in the range $10^{-1} \lesssim a \lesssim 1$. If we are interested in observations that only care about a smaller range of the scale factor, then the allowed range of H_0/k increases. We also plot lines of constant multipole $l \sim kd(a)$, which provides a rough estimate of the relationship between k and angular scales at different redshifts.

We now turn to a discussion of the range of scales where we expect our procedure to be applicable. Our ansatz uses the ratio of the physical size of the perturbation $d_p(a)$ to the size of the Hubble horizon $d_H(a) \equiv 1/H(a)$ as our small (post-Newtonian) expansion parameter. In Fourier space $d_p(a) \sim a/k$ and we need $d_p(a)/d_H(a) \sim aH/k \ll 1$ for the expansion in aH/k to be meaningful. From Figure 1, we can see that for a given k, aH/k is a decreasing function of the scale factor (till dark energy domination). So if $aH/k \ll 1$ at early times, it will remain so till today.

We first give a rough upper bound on H_0/k. In addition to $aH/k \ll 1$, from an observational standpoint, the largest scales of interest are the ones where cosmic variance does not significantly limit the precision of our measurements (angular multipoles $l \gg 1$). To convert this constraint on l to a constraint on H_0/k, we need a relationship between k and l. For large k, a perturbation with a given k corresponds roughly to a multipole $l \sim kd(a) = (aH/k)^{-1}aHd(a)$, where $d(a)$ is the co-moving distance. Note that this relationship is scale factor dependent. Let us take $l \sim 30$ as the largest angular scale where cosmic variance does not significantly limit measurement precision. For $0.1 \lesssim a \lesssim 0.5$ we get $aH/k \sim aHd(a)/l \lesssim 0.06$ since $aHd(a) \lesssim 3.7$ in this range. At $a \sim 0.5$, the corresponding comoving wavevector of the perturbation is $k \sim 10^{-2}\,h\,\mathrm{Mpc}^{-1}$ or equivalently $H_0/k \sim 3 \times 10^{-2}$. On the other hand, this same l would correspond to $aH/k > 1$ for $a \sim 10^{-3}$. So if we are also interested in the CMB, then $aH/k \lesssim 1$ implies that $l \sim (aH/k)^{-1}aHd(a) \gtrsim 55$ at $a \sim 10^{-3}$ because $aHd(a) \sim 55$ at last scattering. In summary, for observations at large redshifts, the requirement $aH/k \lesssim 1$ provides the upper bound on the scales for which our ansatz can be used wheres $l \gtrsim 30$ does the same as low redshifts. This upper bound can be relaxed depending on the range of redshift in which the observations are made.

Now, for the lower bound on H_0/k we get $H_0/k \gtrsim 3 \times 10^{-3}$. This corresponds to $k_{nl} \sim 10^{-1}\,h\,\mathrm{Mpc}^{-1}$ which is at the boundary between linear and nonlinear evolution of δ_m today. At these scales the linear and nonlinear matter power spectrum differ by a few percent today (and less in the past). Since the scalar metric fluctuations $\mathcal{O}[\Phi(\mathbf{x}, a), \Psi(\mathbf{x}, a)] \sim 10^{-5}$ on these scales, as indicated by measurements of the cosmic microwave background (CMB), we can linearize the field equations in Φ, Ψ and δ_m at these scales. Another reason for this lower bound is that on scales larger than these we do not expect a significant bias between the baryonic and nonbaryonic matter. We can relax the lower bound if the observations are restricted to smaller scale factors since the scale factor dependence of the boundary between linear and nonlinear evolution is given by $k_{nl}(a) \sim 10^{-1}a^{-3/2}\,h\,\mathrm{Mpc}^{-1}$. For example if we restrict our selves to $10^{-3} \lesssim a \lesssim 10^{-1}$, then $H_0/k \gtrsim 10^{-4}$.

Figure 1 shows the typical order of magnitude of aH/k for the range $3\times10^{-3} \lesssim H_0/k \lesssim 3\times10^{-2}$ (filled yellow region). Finally, the range of scale factors we have in mind for our framework is $10^{-1} \lesssim a \lesssim 1$. Gravitational dynamics at late times (large a) is particularly interesting due to cosmic acceleration. The next generation of observations including lensing, BAO, cluster counts, galaxy power spectra etc. will be made within this range. Although we concentrate on late times, with some care, our framework can be used with CMB observations. For example, after including radiation and baryons, using our framework we can calculate the anisotropies in the CMB if we know the initial conditions for each mode *after* it enters the horizon. Once the modes are sufficiently subhorizon, their subsequent evolution can be used to constrain the coefficient functions. Note, that for the mode corresponding to the first acoustic peak ($l \sim 220$), $aH/k \sim 0.3$ at last scattering. This comoving scale (as well as a range of smaller scales) is within the yellow shaded region in Figure 1.

Before we end this section we provide a concrete example of what the coefficient functions look like in a simple case, the Einstein-de Sitter universe:

$$\begin{aligned}
&\beta_0 = \gamma_0 = 1,\\
&\beta_1 = \gamma_1 = 0,\\
&\beta_2 = \gamma_2 = -3,\\
&\delta_0 = a/a_i,\\
&\delta_1 = 0,\\
&\delta_2 = 3(a/a_i)(1 - a/a_i).
\end{aligned} \tag{3.4}$$

where $a_i \sim 10^{-2}$. We turn to the calculation of the coefficient functions in the next section.

3.3 Application of the framework with examples

In this section we calculate the coefficient functions for GR with a cosmological constant and nonrelativistic matter, GR with quintessence, scalar-tensor theories, $f(R)$ theories and DGP gravity. In general, the nonrelativistic matter consists of baryons, massive neutrinos and nonbaryonic dark matter with (possibly) nongravitational interactions between them and other fields. For simplicity we will ignore massive neutrinos and baryons in this section. Local tests of gravity provide strong constraints on baryons and photons and their interactions. They do not yet provide similar constraints on the interactions of nonbaryonic matter. Hence, nonbaryonic matter need not be covariantly conserved. However in the examples considered, we treat dark matter as a perfect fluid that is covariantly conserved for simplicity. This allows us to use the conservation equation (3.3), which is sometimes easier to use than a gravitational field equation that would otherwise take its place.

The basic strategy is to substitute our ansatz into the field equations and conservation equations and solve for the coefficient functions. We begin by substituting our ansatz (3.2) into the conservation equation for nonrelativistic perfect fluid dark matter (3.3), collecting terms with like powers of (aH/k) and setting their coefficient terms equal to zero to obtain

$$\begin{aligned}
&\left[a^2\partial_a^2+(2+q)a\partial_a\right]\delta_0-\frac{4\pi G\rho_m}{H^2}\beta_0\delta_0=0,\\
&\left[a^2\partial_a^2+(2+q)a\partial_a\right][(aH)\delta_1]-\frac{4\pi G\rho_m}{H^2}\beta_0[(aH)\delta_1]=\frac{4\pi G\rho_m}{H^2}(aH)\beta_1\delta_0,\\
&\left[a^2\partial_a^2+(2+q)a\partial_a\right][(aH)^2\delta_2]-\frac{4\pi G\rho_m}{H^2}\beta_0[(aH)^2\delta_2]\\
=&\frac{4\pi G\rho_m}{H^2}(aH)^2[2\beta_1\delta_1+\beta_2\delta_0-3(a^2\partial_a^2+qa\partial_a-q)(\gamma_0\delta_0)],
\end{aligned}\tag{3.5}$$

where $q(a)$ and $H(a)$ are assumed to be known from the background evolution. The above equations are second order differential equations for δ_0, δ_1 and δ_2. The equation for δ_0 can be solved once β_0 is known. $G\beta_0$ is the effective gravitational "constant". If $\beta_0=1$, the equation for δ_0 is the usual equation for the fractional matter overdensity on linear and small scales in GR with nonrelativistic matter as the only clustering component.

We digress a bit to note that for $\bar{\delta}_n \equiv (aH)^n \delta_n$, the differential operator acting on $\bar{\delta}_n$ is $[a^2\partial_a^2 + (2+q)a\partial_a - 4\pi G\rho_m\beta_0/H^2]$. This feature continues if we were to go to higher order terms as well, hence it might be useful to find a Green's function for this operator. In general, to solve for δ_1, we need to know β_0, β_1 and δ_0 with two initial conditions. Similarly, to solve for δ_2 we need to know $\beta_0, \gamma_0, \delta_0, \beta_1, \delta_1$ and β_2 along with two initial conditions. To progress further we turn to specific theories of gravitation. Our aim is to show how to apply the formalism rather than discuss in detail the various models considered. We leave out the detailed steps, which are straightforward but tedious.

3.3.1 General relativity with cold dark matter and the cosmological constant

We start with the usual Einstein Hilbert action:

$$S = \frac{1}{16\pi G}\int d^4x\sqrt{-g}\,[R - 2\Lambda] + \int d^4x\sqrt{-g}\mathcal{L}_m, \tag{3.6}$$

with $\mathcal{L}_m$, the lagrangian density for perfect fluid cold dark matter The corresponding field equations are

$$G^\mu_\nu + \Lambda\delta^\mu_\nu = 8\pi G T^\mu_\nu, \tag{3.7}$$

where $G^\mu_\nu = R^\mu_\nu - \delta^\mu_\nu R/2$ and T^μ_ν is the energy-momentum tensor for a pressureless perfect fluid. As usual, we separate the field equations into the background and perturbed parts (first order in Φ, Ψ and δ_m). Upon substitution of our ansatz into the perturbed field equations we get the following expressions/equations for the coefficient functions.

$$\begin{aligned}
&\left[a^2\partial_a^2 + (2+q)a\partial_a\right]\delta_0 - \frac{4\pi G\rho_m}{H^2}\delta_0 = 0,\\
&\left[a^2\partial_a^2 + (2+q)a\partial_a\right][(aH)\delta_1] - \frac{4\pi G\rho_m}{H^2}[(aH)\delta_1] = 0,\\
&\left[a^2\partial_a^2 + (2+q)a\partial_a\right][(aH)^2\delta_2] - \frac{4\pi G\rho_m}{H^2}[(aH)^2\delta_2]\\
=&-\frac{12\pi G\rho_m}{H^2}(aH)^2\left[a^2\partial_a^2 + (q+1)a\partial_a - q\right]\delta_0,
\end{aligned}\tag{3.8}$$

$$\begin{aligned}
&\beta_0 = \gamma_0 = 1,\\
&\beta_1 = \gamma_1 = 0,\\
&\beta_2 = \gamma_2 = -3\frac{a\partial_a\delta_0}{\delta_0},
\end{aligned}$$

where we used the 00 and $i \neq j$ Einstein equations along with the coefficient form of the conservation equations (3.5). We need to provide 6 constants of integration for the three second order differential equations. We take these to be

$$\begin{aligned}
\delta_0(a_i) &= 1, \qquad a_i\partial_a\delta_0(a_i) = 1,\\
\delta_1(a_i) &= 0, \qquad a_i\partial_a\delta_1(a_i) = 0,\\
\delta_2(a_i) &= 0, \qquad a_i\partial_a\delta_2(a_i) = -3.
\end{aligned}\tag{3.9}$$

This ensures that $\delta_m(\mathbf{k}, a_i) = \delta_{mi}(\mathbf{k})$, thus defining $\delta_{mi}(\mathbf{k})$ in our ansatz (3.2). The derivatives are chosen to agree with the case of pure matter domination at early times ($a_i \sim 10^{-2}$), where the explicit solution takes the form $\delta_0 = a/a_i$, $\delta_1 = 0$ and $\delta_2 = 3(a/a_i)(1 - a/a_i)$ after rejecting the decaying modes. For any model under consideration, we can choose fix initial condition by rejecting the decaying mode. For simplicity, we shall use the above initial conditions for the scalar-tensor as well the braneworld models for which we plot the coefficient functions. For these models the parameters have been chosen so that at $a_i \sim 10^{-2}$, the conservation equations approach those of an Einstein-deSitter universe in GR.

The dashed lines in Figures 2 and 3 show these dimensionless coefficient functions for the spatially flat-ΛCDM with $\Omega_m = 8\pi G\rho_{m0}/3H_0^2 = 0.3$. Since $\beta_0 = \gamma_0 = 1$, there are no corrections to the Newtonian gravitational constant as far as growth of perturbations is concerned on small scales. Since single gradients do not appear in the Einstein equations involving δ_m, Φ and Ψ (after eliminating the velocity through the conservation equation), $\beta_1 = \gamma_1 = 0$. The 00 Einstein equation imposes $\delta_1 = 0$. The fact that $\beta_2 = \gamma_2 \neq 0$ reflects corrections because of GR to the relationship between matter and metric perturbations, whereas $\beta_2 = \gamma_2 \neq -3$ reflects the effect of the cosmological constant. δ_0 characterizes the growth of structure on small scales. It deviates from $\delta_0 = a/a_i$ because of Λ. δ_2 reflects the corrections to the growth function as we move to larger scales. Note that β_2 and γ_2 and δ_2 are multiplied by $(aH/k)^2$, whose magnitude is shown in Figure 1. The terms $\beta_2(aH/k)^2$, $\gamma_2(aH/k)^2$ and $\delta_2(aH/k)^2$ are much smaller than β_0, γ_0 and δ_0, making it difficult to observe their effects unless we investigate large scales.

3.3.2 Scalar-tensor theory with cold dark matter (matter representation)

Scalar-tensor theories are popular alternatives to GR. In the matter representation (also called the Jordan frame), the action contains two free functions $f(\varphi)$ and $V(\varphi)$

$$S = \frac{1}{16\pi G}\int d^4x\sqrt{-g}\,[f(\varphi)R + \mathcal{L}_\varphi] + \int d^4x\sqrt{-g}\mathcal{L}_m. \tag{3.10}$$

Note that we have decided to make φ dimensionless since we wish to treat the perturbation in this field $\delta\varphi$ on the same footing as the metric perturbations Φ and Ψ. Also $\mathcal{L}_\varphi = -(\partial\varphi)^2/2 - V(\varphi)$ and $\mathcal{L}_m$ does not contain φ. The field equations for this theory are

$$\begin{aligned} &G^\mu_\nu + \frac{1}{f}\left[\delta^\mu_\nu\Box - \nabla^\mu\nabla_\nu\right] f \\ =&\frac{8\pi G}{f}T^\mu_\nu + \frac{1}{2f}\left[\partial^\mu\varphi\partial_\nu\varphi - \delta^\mu_\nu\left(\frac{1}{2}\partial^\sigma\varphi\partial_\sigma\varphi + V\right)\right]. \end{aligned} \tag{3.11}$$

The field equation for φ is

$$\Box\varphi - V_\varphi + f_\varphi R = 0, \tag{3.12}$$

where $f_\varphi = \partial_\varphi f$ and $V_\varphi = \partial_\varphi V$.

These field equations at the background level can be found in the literature (for example see [45]). Using our ansatz in the perturbed gravitational field equations and the field equations for φ at first order in Φ, Ψ, δ_m and $\delta\varphi$, collecting terms with like powers of (aH/k), and setting the expression in front of each power of (aH/k) equal to zero, we get the following expressions/equations for the coefficient functions:

$$
\begin{aligned}
\beta_0 &= \frac{1}{f}\left(\frac{1+4f\alpha^2}{1+3f\alpha^2}\right) \approx \frac{1}{f} + \mathcal{O}[\alpha^2],\\
\gamma_0 &= \frac{1}{f}\left(\frac{1+2f\alpha^2}{1+3f\alpha^2}\right) \approx \frac{1}{f} + \mathcal{O}[\alpha^2],\\
\beta_1 &= \gamma_1 = 0,\\
\beta_2 &= -\frac{3}{f}\frac{a\partial_a\delta_0}{\delta_0} + \frac{1}{4f^2}(a\partial_a\varphi)^2\\
&\quad + \left[-3(a\partial_a\varphi)\frac{a\partial_a\delta_0}{\delta_0} + \frac{1}{2}(a\partial_a\varphi)^2\frac{\alpha_\varphi}{\alpha} + 3(a\partial_a\varphi) + \frac{3V_\varphi}{2H^2}\right]\frac{\alpha}{f}\\
&\quad + \mathcal{O}[\alpha^2],\\
\gamma_2 &= -\frac{3}{f}\frac{a\partial_a\delta_0}{\delta_0} + \frac{1}{4f^2}(a\partial_a\varphi)^2\\
&\quad + \left[(a\partial_a\varphi)\frac{a\partial_a\delta_0}{\delta_0} + \frac{1}{2}(a\partial_a\varphi)^2\frac{\alpha_\varphi}{\alpha} - (a\partial_a\varphi) - \frac{V_\varphi}{2H^2}\right]\frac{\alpha}{f}\\
&\quad + \mathcal{O}[\alpha^2],
\end{aligned}
\tag{3.13}
$$

where $\alpha = f_\varphi/f$ is the coupling function and all the functions depend on the scale factor a . We have calculated the full expressions for β_2 and γ_2, which are rather long. The first two terms are listed as a power series in the coupling function $\alpha \ll 1$ with $\alpha \sim \alpha_\varphi, \alpha_{\varphi\varphi}...$. We used the $i \neq j$ equation, $\alpha\delta\varphi = \Psi - \Phi$, to eliminate $\delta\varphi$ from the field equations. The 00 equation and the field equation for $\delta\varphi$ yield β_n and γ_n with $(n = 0, 1, 2)$. The equations for δ_0, δ_1 and δ_2 are given by equations (3.5) with β_n and γ_n $(n = 0, 1, 2)$ given above. Again using the initial conditions (3.9), we can solve for all the coefficient functions once $f(\varphi)$ and $V(\varphi)$ have been provided. Note that the difference $\Phi - \Psi$ depends on $\beta_n - \gamma_n$ $(n = 0, 2)$. This is usually small for $\alpha \ll 1$ since $\beta_0 - \gamma_0 \sim \alpha^2$ and $\beta_2 - \gamma_2 \sim \alpha$.

We plot the coefficient functions in Figures 2 and 3. We have chosen $f(\varphi) =$

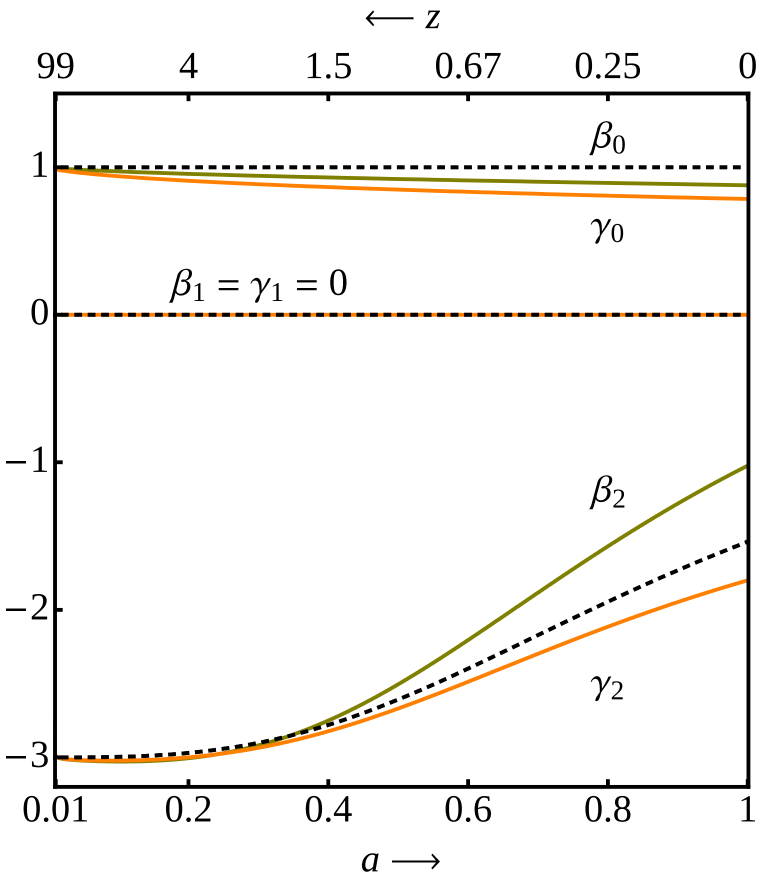

Figure 3.2: The dimensionless coefficient functions characterizing the relationship between the metric perturbations and matter distribution are shown above for $F\Lambda$CDM(dashed lines) and the scalar-tensor theory (STT) (solid lines). The STT model is chosen so that its expansion history is consistent with observations. In the case of ΛCDM $\beta_0 = \gamma_0 = 1$, $\beta_1 = \gamma_1 = 0$ and $\beta_2 = \gamma_2$. At early time (matter domination) $\beta_2 = \gamma_2 = -3$ with the cosmological constant causing a departure from this value at late times. The variation of β_0 with the scale factor in the STT can be interpreted as a variation of Newton's constant "$G\beta_0$" as far as growth of perturbations is concerned. Also note that for STT, $\beta_0 \neq \gamma_0$ and $\beta_2 \neq \gamma_2$. For STT, the difference in the coefficient functions is due to $\Phi - \Psi = -\alpha(\varphi)\delta\varphi \neq 0$. Note that $\beta_1 = \gamma_1 = 0$ in STT as well as ΛCDM. We remind the reader that in the ansatz (3.2) the coefficients β_2 and γ_2 are multiplied by $(aH/k)^2$, whose magnitude is shown in Figure 1, making them accessible at large scales only.

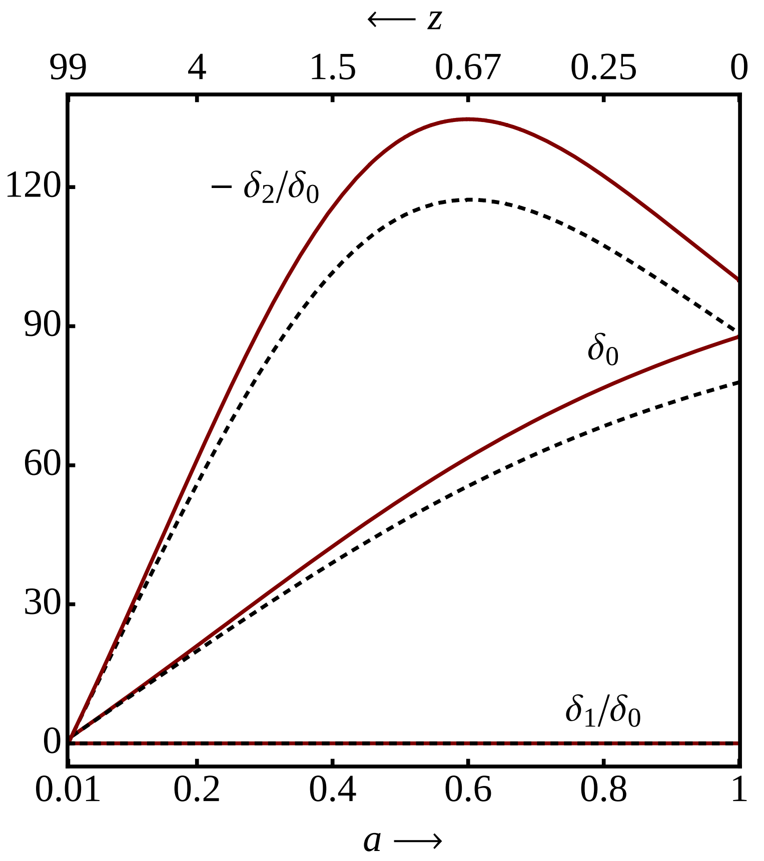

Figure 3.3: The dimensionless coefficient functions characterizing growth of structure are show above for ΛCDM(dashed lines) and the scalar-tensor theory (STT) (solid lines). The STT model is chosen so that its expansion history is consistent with observations. δ_0 is the usual growth function on small scales, whereas δ_2 characterizes the departures as we move to larger scales. For ΛCDM and STT, $\delta_1 = 0$. We note that δ_2 is the coefficient of $(aH/k)^2$, which is small withing the scales of interest (see Figure 1). The initial conditions for δ_0 and δ_2 are chosen at $a_i \sim 10^{-2}$ and are consistent with growth of structure in a matter dominated era.

$1 + c_1\varphi^2$ and $V(\varphi) = 2\Lambda(1 + c_2\varphi^2)$ with $c_1 = c_2 = 0.1$. The initial conditions and c_1, c_2 were chosen to ensure that the expansion history remains consistent with observations (consistent with ΛCDM to within a few percent). The difference between β_n and γ_n $(n = 0, 2)$ is due to nonminimal coupling $(\alpha \neq 0)$. We stress that we have not included baryons in this illustrative calculation. Including baryons would lead to very strong constraints on the function $f(\varphi)$ today from solar system tests [46]. For an example of a STT that includes dark matter and baryons with different couplings to gravity see [47].

3.3.3 General relativity with cold dark matter and quintessence

GR with quintessence is a special case of the scalar-tensor theories discussed above, with $f(\varphi) = 1$. The action and corresponding field equations are

$$S = \frac{1}{16\pi G}\int d^4x\sqrt{-g}\,[R + \mathcal{L}_\varphi] + \int d^4x\sqrt{-g}\mathcal{L}_m \tag{3.14}$$

$$G^\mu_\nu = 8\pi G T^\mu_\nu + \frac{1}{2}\left[\partial^\mu\varphi\partial_\nu\varphi - \delta^\mu_\nu\left(\frac{1}{2}\partial^\sigma\varphi\partial_\sigma\varphi + V\right)\right] \tag{3.15}$$

$$\Box\varphi - V_\varphi = 0 \tag{3.16}$$

The coefficient functions are given by

$$\begin{aligned}\beta_0 &= \gamma_0 = 1,\\ \beta_1 &= \gamma_1 = 0,\\ \beta_2 &= \gamma_2 = -3\frac{a\partial_a\delta_0}{\delta_0} + \frac{1}{4}(a\partial_a\varphi)^2\end{aligned} \tag{3.17}$$

where $(a\partial_a\varphi)^2/4 = 1 - q - 4\pi G\rho_m/H^2$. The $i \neq j$ Einstein equation yields $\beta_n = \gamma_n$ $(n = 0, 1, 2)$. We used the $0i$ equation to eliminate $\delta\varphi$ from the field equations. As before δ_0, δ_1 and δ_2 are provided by equation (3.5).

We pause to comment on a difference between minimally and nonminimally coupled scalar-tensor theories. Consider the field equation (3.12) for $\delta\varphi$:

$$\begin{aligned}&\left[a^2\partial_a^2+(3+q)a\partial_a\right]\delta\varphi+\left[\left(\frac{k}{aH}\right)^2+\frac{V_{\varphi\varphi}}{H^2}-6(1+q)f_{\varphi\varphi}\right]\delta\varphi\\ =&(a\partial_a\varphi-6f\alpha)a\partial_a\Phi+3(a\partial_a\varphi-2(4+q)f\alpha)a\partial_a\Psi\\ &-2\left(6f\alpha(1+q)+\frac{V_\varphi}{H^2}\right)\Phi+2f\alpha\left(\frac{k}{aH}\right)^2(\Phi-2\Psi)\end{aligned} \tag{3.18}$$

In the minimally coupled case we set $f(\varphi)=1,\alpha(\varphi)=0$ to get

$$\begin{aligned}&\left[a^2\partial_a^2+(3+q)a\partial_a\right]\delta\varphi+\left[\left(\frac{k}{aH}\right)^2+\frac{V_{\varphi\varphi}}{H^2}\right]\delta\varphi\\ =&(a\partial_a\varphi)a\partial_a\Phi+3(a\partial_a\varphi)a\partial_a\Psi-2\frac{V_\varphi}{H^2}\Phi.\end{aligned} \tag{3.19}$$

From the above equations we can see that in the nonminimally coupled case, for $k/aH\gg 1$ we have $\delta\varphi\propto\alpha(\varphi)\Phi$ whereas in the minimally coupled case $\delta\varphi\propto\Phi(aH/k)^2$. Along with $\Phi\propto\delta_m(aH/k)^2$, at large k the additional field $\delta\varphi$ follows the same aH/k expansion as the potentials with $\delta_{mi}(\mathbf{k})$ multiplying the expansion. This is one of the arguments we had used in Section 2 to justify the form of our ansatz. We have assumed $\Psi=\mathcal{O}[\Phi]$ in this argument.

3.3.4 $f(R)$ gravity with cold dark matter

In recent years modifications of the Einstein-Hilbert action in the form of a function of the Ricci scalar has become a popular alternative to quintessence (see for example [22, 48]). The action and field equations are

$$\begin{aligned}&S=\frac{1}{16\pi G}\int d^4x\sqrt{-g}\left[R+f(R)\right]+\int d^4x\sqrt{-g}\mathcal{L}_m\\ &(1+f_R)G^\mu_\nu-\delta^\mu_\nu\frac{f}{2}+[\delta^\mu_\nu\Box-\nabla^\mu\nabla_\nu]f_R=8\pi GT^\mu_\nu\,.\end{aligned} \tag{3.20}$$

In the above expressions $f_R = \partial_R f(R)$. The coefficient functions are

$$
\begin{aligned}
\beta_0 &= \frac{4}{3(1+f_R)}, \\
\gamma_0 &= \frac{2}{3(1+f_R)}, \\
\beta_1 &= \gamma_1 = 0, \\
\beta_2 &= \frac{1}{(1+f_R)}\left[\frac{2}{3}\frac{a^2\partial_a^2\delta_0}{\delta_0}\right. \\
&\quad -\frac{2}{3}\{(24B(j+q-2)+2-q\}\frac{a\partial_a\delta_0}{\delta_0} \\
&\quad +4B\left\{10-4q+q^2+2j(q-4)-s\right\} \\
&\quad \left.+72B^2(j+q-2)^2-4(j+q-2)a\partial_a B+2q-\frac{1}{9B}\right], \\
\gamma_2 &= \frac{1}{(1+f_R)}\left[-\frac{2}{3}\frac{a^2\partial_a^2\delta_0}{\delta_0}\right. \\
&\quad +\frac{2}{3}\{(6B(j+q-2)-7-q\}\frac{a\partial_a\delta_0}{\delta_0} \\
&\quad -4B\left\{4-q+q^2+j(2q-5)-s\right\} \\
&\quad \left.+4(j+q-2)a\partial_a B-2q+\frac{1}{9B}\right],
\end{aligned}
\tag{3.21}
$$

where $j = dq/d\ln a - (1-2q)q$ and $s = dj/d\ln a - (2-3q)j$ are the scale factor dependent functions, jerk and snap respectively, and $B = H^2 f_{RR}/(1+f_R)$[4]. To obtain δ_0, δ_1 and δ_2 we use equation (3.5). Again, as in the case of GR and scalar-tensor example, the coefficients of the aH/k term in the ansatz vanish. Note that we have assumed $(aH/k)^2 B^{-1} \ll 1$ in deriving the above expressions, hence it is not appropriate to take the limit $B \to 0$ after deriving the coefficient functions. Under this assumption, to lowest order in aH/k, we get $\Phi = 2\Psi$, unlike GR with ΛCDM where $\Phi = \Psi$. If we take the opposite limit, $(aH/k)^2 B^{-1} \gg 1$ the coefficient functions are quite different. In particular, $\beta_0 = \gamma_0 = (1+f_R)^{-1}$ and we get reach the GR limit as we let $f_R \to 0$. As long as we ensure, a priori, that this transition

---

[4] Our $B = H^2 f_{RR}/(1+f_R)$ differs from the definition of B in [49] by a factor of $(q-1)/6(j+q-2)$

scale $(H/k_C) \sim B^{1/2}$ (see for example [44]) is outside the length range of physical scales of interest, we can use our ansatz. More details on the dynamics of $f(R)$ theories in the context of structure formation, solar system tests, etc. can be found in [50, 49, 51, 52, 44]. Finally we note, that our purpose in discussing $f(R)$ models was to illustrate an application of our framework. These models suffer from a number of problems including fine tuning to match the solar system constraints as well as a rather serious instability, where the curvature blows up at finite matter densities [53].

3.3.5 Brane world models: DGP Gravity

As a final example, we provide the expressions and equations governing the coefficient functions for DGP gravity. In this model, matter is restricted to a four dimensional brane in a five dimensional bulk. In addition to the the Einstein-Hilbert action in the bulk, there is an induced four dimensional term [41]. More explicitly, the full 5D action is given by

$$\begin{aligned} S = \frac{1}{32\pi G r_c} \int d^5x \sqrt{-g_{(5)}} R_{(5)} \\ + \frac{1}{16\pi G} \int d^4x \sqrt{-g} R + \int d^4x \sqrt{-g} \mathcal{L}_m \,. \end{aligned} \tag{3.22}$$

In the above action $r_c = G^{(5)}/2G$ where $G^{(5)}$ is 5D gravitational constant. The field equations are given by the Einstein equations in the bulk $(A, B = 0, 1, 2, 3, 4)$:

$$G^A_B = 0, \tag{3.23}$$

and the Israel junction conditions on the brane $(\mu, \nu = 0, 1, 2, 3)$

$$K^\mu_\nu = r_c \left(\mathcal{G}^\mu_\nu - \frac{1}{3} \mathcal{G} \delta^\mu_\nu \right) , \tag{3.24}$$

where K^μ_ν is the extrinsic curvature on the brane. In Gaussian normal co-ordinates, the extrinsic curvature is given by the derivative normal to the brane

$$K^\mu_\nu = \frac{1}{2}\partial_y g_{\mu\nu} \, . \tag{3.25}$$

On the RHS of the junction conditions

$$\mathcal{G}^\mu_\nu = G^\mu_\nu - 8\pi G T^\mu_\nu \, , \tag{3.26}$$

where G^μ_ν and T^μ_ν are the 4D Einstein and stress-energy tensors respectively. For this model our coefficient functions are given by (which can be easily determined from the results in [54])

$$\begin{aligned} \beta_0 &= \frac{4-2Hr_c(2+q)}{3-2Hr_c(2+q)}, \\ \gamma_0 &= \frac{2-2Hr_c(2+q)}{3-2Hr_c(2+q)}, \\ \beta_1 &= \frac{12(-1+Hr_c(1+q))^2}{Hr_c(3-2Hr_c(2+q))^2}, \\ \gamma_1 &= \frac{6(1-2Hr_c)(1-Hr_c(1+q))}{Hr_c(3-2Hr_c(2+q))^2}. \end{aligned} \tag{3.27}$$

We can solve for δ_0 and δ_1 using (3.5). Note that even though $\delta_1(a_i) = a_i\partial_a\delta_1(a_i) = 0$, $\delta_1(a) \neq 0$ because $\beta_1 \neq 0$. We note an important difference between the the DGP braneworld model and the examples considered so far in this paper. Unlike the previous examples, the coefficients of the odd power of aH/k are non-zero ($\beta_1, \gamma_1, \delta_1 \neq 0$). As explained below, the odd power of aH/k arises due to the junction conditions that must be satisfied by metric perturbations at the location of our four dimensional brane in the higher dimensional bulk.

A general way to understand the odd power in our (aH/k) expansion is as follows. The Israel junction condition relates the first (y) derivative of a metric perturbation normal to the brane at its surface to the 4D Einstein tensor and stress-energy tensor in the brane (see equations (3.24),(3.25) and (3.26)). The 5D vacuum Einstein equations in the bulk provide homogeneous second-order linear differential equations for the metric perturbations. Just outside the brane, the operators in these equations will be

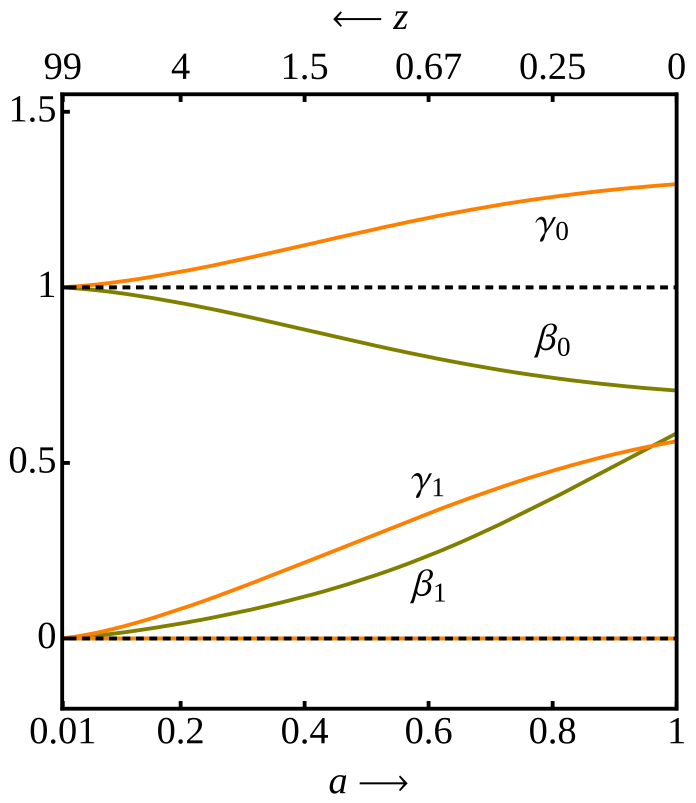

Figure 3.4: The dimensionless coefficient functions characterizing the relationship between the metric perturbations and matter distribution are show above for ΛCDM(dashed lines) and DGP braneworld model (solid lines). The variation of β_0 with the scale factor in DGP can be interpreted as a variation of Newton's constant "$G\beta_0$" as far as growth of perturbations is concerned. Also note that for DGP, $\beta_0 \neq \gamma_0$. In contrast to all the other examples considered, the coefficients of aH/k: $\beta_1, \gamma_1 \neq 0$. This is due to the junction conditions on the brane. The linear aH/k term provides an intriguing signature of braneworld models.

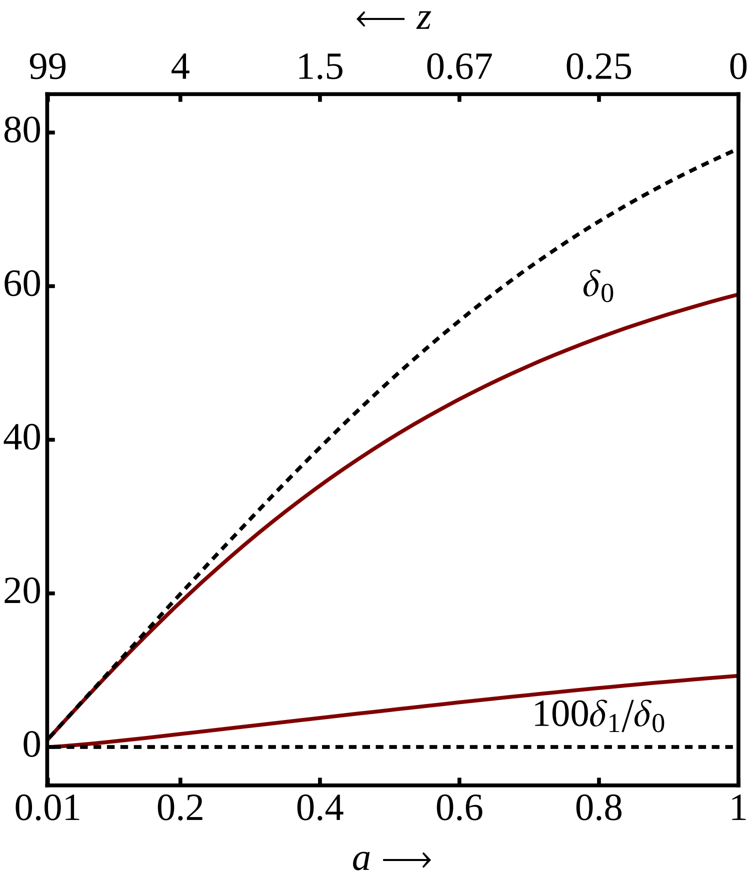

Figure 3.5: The dimensionless coefficient functions characterizing growth of structure are show above for ΛCDM(dashed lines) and DGP braneworld model (solid lines). δ_0 is the usual growth function on small scales, whereas δ_1 characterizes the departures as we move to larger scales. In contrast to ΛCDM, for the DGP case $\delta_1 \neq 0$. This could provide a distinct signature of braneworld models.

dominated (in our large k limit) by the 3-dimensional spatial derivatives (continuous across the brane surface), giving terms proportional to k^2. These must be balanced by terms proportional to ∂_y^2. Thus we see that ∂_y must be proportional to k.

We note that the above arguments are rather general. Although the RHS of equation (3.24) will be different in different braneworld models, due to the LHS a linear k^{-1} term will be present in most braneworld models. However, the coefficients might not be of $\mathcal{O}[1]$ as in the case of DGP. [5] The existence of this non-zero linear aH/k term provides an exciting new signature for the DGP (or other) braneworld models. Since on subhorizon scales $aH/k \ll 1$, it is significantly easier to constrain the linear term compared to the quadratic one.

We plot the coefficient functions in Figures 4 and 5. For DGP, we have assumed $\Omega_m = 0.25$ and $\Omega_k = 0$ for simplicity although this model is in tension with current data [55]. The dotted lines represent the coefficients in ΛCDM. We have not calculated the coefficients β_2, γ_2 and δ_2 of the $(aH/k)^2$ terms for the DGP case because they are expected to be subdominant compared to the linear aH/k terms.

We have ignored two important features in the DGP model, the strong coupling problem and the ghost problem in the self accelerating branch (see for example [56, 57]). The transition to the strong coupling regime happens at the Vainshtein radius $r_\star$. For a localized matter distributions with Schwarzchild radius r_g, $r_\star \sim (r_g r_c^2)^{1/3}$. Using $r_c \sim 1/H_0$, for the largest localized distribution in our universe, galaxy clusters ($M \sim 10^{14} M_\odot$), we get $r_\star < 10\,\mathrm{Mpc}$. This scale is well below the smallest scales where we intend to apply our framework. We are unaware of a calculation for $r_\star$, when considering distribution of matter on cosmological scales (which is not localized). To avoid the ghost problem one can choose the normal branch rather than the self-accelerating branch of the DGP model (see for example [58]). A calculation similar to the one done in this section can be repeated for the normal branch, however in that case we do not have an accelerating universe.

In this section we have calculated the coefficient functions for a few examples. Our aim was to give a flavor of the calculations rather than be exhaustive in the

---

[5] Another way of seeing the odd power of aH/k in DGP case is through the form of a propagator which involves $\sqrt{\Box}$ [41].

investigation of the models considered. It would be interesting to investigate these models in more detail in the context of these coefficient functions to see if there is come generic behavior across a large class of models. Based on the examples considered it might be tempting to conclude that $\beta_n - \gamma_n \neq 0$ indicates physics beyond general relativity. However this is not so. For example a hypothetical dark energy component could also yield significant anisotropic stress. In the early universe, a more standard source of anisotropic stress was provided by neutrinos. Nevertheless this difference could serve as an indicator of new physics in the matter or gravity sector. Another intriguing result was the presence of a term linear in aH/k in the braneworld scenario, which could provide a unique signature of braneworld models. We have left out many possibilities including Bekenstein's TeVeS [59], models with non-canonical kinetic terms [60], models of imperfect fluid dark energy with anisotropic stress [61], and many others (see [62] for a review). We now turn our attention to observables and their relationship to the coefficient functions.

3.4 Observational implications

We have outlined a procedure that allows many alternative, dynamical theories to GR with FΛCDM cosmology to be explored within a common framework. Our approach has been devised with future observations in mind as its usefulness is limited to the observations that we expect will be the most prescriptive. We assume that the expansion history of the universe is well constrained through the distance redshift relation obtained from the apparent magnitude of Type 1a supernovae, the baryon acoustic oscillation scale and the ratio of baryons to total matter in galaxy clusters. The large k expansion connects the inhomogeneous nonrelativstic matter distribution to the perturbed metric in a universe of known (unperturbed) kinematical behavior, *i.e.* with a given relation $H(a)$ [or, equivalently, $a(t)$]. Our approach also presumes that the theories under consideration provide an understanding of how the distribution of observable entities such as galaxies relate to that of total mass. This allows us to focus on the manner in which structure can be observed to grow in the linear regime well within the horizon, which avoids the limitations imposed by cosmic variance considerations and the complications associated with gas dynamics. We further suppose that gravitational motion of baryonic matter and photons follows timelike and null geodesics respectively in this spacetime.

From an observational standpoint, our focus is on comoving length scales from $\sim$ 40 Mpc to $\sim$ 400 Mpc or equivalently $300 \gtrsim l \gtrsim 30$ at $z \sim 1$, where we expect the effects to stand out the best. There are three types of observations that are likely to be relevant. Firstly, there are direct measurements of the two point correlation function and its evolution. Counting galaxies (or clusters) in three dimensions will lead to measurements of the evolution of the density function δ_m using future survey instruments such as LSST [63, 64] limited solely by cosmic variance as the photometric redshift accuracy and biasing errrors will be ignorable on these scales. We can construct the ratio of the matter power spectrum $P_{\delta_m}(k,a)$ at different redshifts to obtain constraints on $\delta_0(a), \delta_1(a)$ and $\delta_2(a)$. As discussed in the Introduction, by taking ratios, we can eliminate the need for knowing the initial conidtions $\delta_{mi}(\mathbf{k})$:

$$\frac{P_{\delta_m}(k,a_2)}{P_{\delta_m}(k,a_1)} = \left[\frac{\delta_0(a_2)}{\delta_0(a_1)}\right]^2 \left[1 + \left\{\frac{aH}{k}\frac{\delta_0}{\delta_1}\right\}_{a_1}^{a_2} + \ldots\right],$$

where $\{f(k,a)\}_{a_1}^{a_2} \equiv f(k,a_2) - f(k,a_1)$.

The second type of observation that will be carried out involves departures from the Hubble flow. These are dominated by the potential function Φ. Under our assumptions, galaxies will follow timelike geodesics and satisfy the linear conservation equations relating their peculiar velocities to Φ.

Finally there are weak lensing observations which depend upon the sum, $\Phi + \Psi$, presuming photons follow null geodesics. These then allow us to track the evolution of Ψ. A combination of these measurements would not only allow us to understand the scale dependent evolution of Φ, Ψ and δ_m but also allow us to probe the relationship between them. For example, using our ansatz, one can obtain constraints on the coefficient functions by comparing the correlation functions for the potentials,

$P_{\Phi+\Psi}(k,a)$ (provided by lensing tomography) and the nonrelativistic matter overdensity $P_{\delta_m}(k,a)$ (provided by growth of structure measurements) using

$$k^4 P_{\Phi+\Psi} \propto P_{\delta_m}(\beta_0+\gamma_0)^2\left[1+2\left(\frac{\beta_1+\gamma_1}{\beta_0+\gamma_0}\right)\left(\frac{aH}{k}\right)+...\right].$$

Comparing the matter and potential power spectrum allows us to constrain the coefficient function without worrying about the initial conditions, though one would still have to obtain this ratio at different redshifts to constrain the time evolution of the coefficient functions.

In this exploratory paper, we have discussed only a handful of observations that can allow is to constrain the coefficient functions. In addition to the observations mentioned above, we list a few other observations that we think might be relevant for our framework. The matter and potential fluctuations at the last scattering surface can be compared to their counterparts at late times, as long as we restrict ourselves to linear subhorizon scales. The same is true for BAO measurements (see discussion of range of scales at the end of Section 2). Recently, a 3σ detection of lensing of the CMB at large l, has been reported by the ACBAR group [65]. This measurement probes the distribution and evolution of potentials after last scattering, and can also be used for constraining the coefficient functions [66]. With the Planck mission [16], such constraints are expected to improve significantly. Another exciting probe of the three dimensional matter distribution may be provided by the 21 cm observations (see for example [67] and references therein).

We have limited ourselves to the linear regime. On small scales, the nonlinear matter power spectrum and its evolution can play a role in the observations discussed above. The linear to nonlinear mapping discussed in [68] can be used for this purpose. However, without understanding the theories under consideration in the nonlinear regime, this is not fully robust.

Recall that $\{\beta_n, \gamma_n, \delta_n\}$ with $(n = 0, 1, 2)$ are functions of the scale factor, a. If the observations are to be done in a limited range of redshifts then Taylor expanding the coefficient functions around the central value of the redshift might be a simple and model independent way of characterizing these coefficient functions in terms of a few parameters. From a theoretical perspective, the coefficient functions will depend on relevant parameters in the theory or model under consideration. A detailed investigation of the parameterization of the coefficient functions and the possible constraints that can be obtained from current and future observations is beyond the scope of this paper. For a more detailed discussion of the observations for distinguishing different models of modified gravity and dark energy we refer the reader to some of the references cited at the end of Section 1 in this paper.

3.5 Discussion

We have outlined a procedure that can be used to test the application of general relativity (more specifically FΛCDM) on cosmological scales in the context where it is most likely to fail and in the regime where observations should be most sensitive to measuring a departure from the general relativistic prediction. The scales are large enough to avoid the complications from nonlinearities and gas physics, yet small enough to avoid strong limitations to the interpretation of observations posed by cosmic variance.

Our procedure assumes that (i) The geometry and kinematics of the universe is understood (ii) baryons and photons behave as ideal test particles following geodesics of the cosmological metric. Given these assumptions, at late times, it is the relationship between the cosmological metric and the nonrelativistic matter distribution (along with their respective evolution) that provides a test for alternatives GR with a cosmological constant and cold dark matter. To probe the dynamics of gravity (or any additional fields) we provided an ansatz, equation(3.2), which gave a relationship between the cosmological metric and nonrelativistic matter perturbations in the linear, subhorizon regime. This form of the ansatz is consistent with a large class of theories with the differences between different theories evident in the coefficient functions $\{\beta_n(a), \gamma_n(a), \delta_n(a)\}$ with $n = 0, 1, 2$. It is hoped that three scalar functions, the nonrelativistic matter overdensity δ_m and the metric potentials Φ and Ψ can be measured over the next decade, providing constraints on the coefficient functions. Constraining these coefficient functions provides observers with concrete targets for testing gravity in a scale dependent manner.

Our goal was to provide a perturbative framework, similar in spirit to the PPN formalism for testing gravity on solar system scales. However unlike the PPN case, we were left with coefficient functions that depend on the scale factor rather than constant coefficients. Although we have not done so in this paper, if the observations are limited to a small range of scale factors, it is possible to characterize these coefficient functions using a few parameters by expanding around a given scale factor at which the observations are centered.

With our choice of scales, we have restricted ourselves to linear, subhorizon evolution. We leave the connection between superhorizon and subhorizon evolution as well as consideration of nonlinearities for the future. Although, we have restricted ourselves to scalar perturbations, the framework could be extended to include vector and tensor perturbations.

3.6 Acknowledgments

We thank the members of KIPAC at Stanford University and the Stanford Gravity Probe-B theory group for helpful discussions. We would also like to thank an anonymous referee for a number of insightful comments and suggestions. MAA would like to acknowledge the financial support of a Stanford Graduate Fellowship. RDB acknowledges support from the National Science Foundation grant AST05-07732. This work was supported in part by the U.S. Department of Energy under contract number DE-AC02-76SF00515.

3.A Aspects of cosmological perturbation theory

The purpose of this appendix is two fold. First, we provide a pedagogical (but rigorous) discussion of gauge invariance and gauge transformations. We also introduce the notion of scalar, vector and tensor decomposition of perturbations. After that, we collect some useful results for scalar perturbations in the Newtonian gauge which was used throughout this chapter.

3.A.1 Gauge transformations and invariance

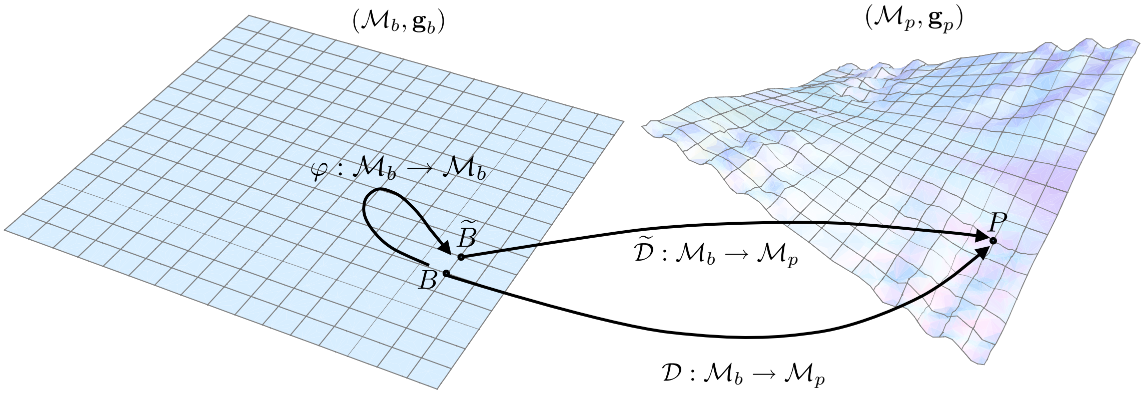

In cosmological perturbation theory we usually start with a known solution for the evolution of a field *and* the spacetime in some simplified scenario. For example, the evolution of a homogenous and isotropic scalar field φ in a FRW universe. The next step is to perturb the spacetime and the field about the known solution and try to understand how these perturbations evolve. However, there is an ambiguity in what we mean by perturbations in a field when the spacetime is also perturbed [6]. This ambiguity in defining perturbations will lead us to the notion of gauge transformations and to the idea of gauge invariant perturbations. We discuss these concepts from a geometric viewpoint first and then relate it to a more conventional co-ordinate viewpoint.

---

[6] The ambiguity exists in unperturbed spacetime as well. Different foliations of spacetime would yield different description of the field and its perturbations. However usually physical considerations such as homogeneity of matter and isotropy allow us to choose the right foliation

Geometric View: Consider two spacetimes: the perturbed physical spacetime $(\mathcal{M}_p, \mathbf{g_p})$ and a fictitious background spacetime $(\mathcal{M}_b, \mathbf{g_b})$ where $\mathbf{g_p}$ and $\mathbf{g_b}$ are the metrics on the manifolds $\mathcal{M}_p$ and $\mathcal{M}_b$ respectively. Let $\mathbf{A_p}$ be a tensor field defined on $\mathcal{M}_p$ and let $\mathbf{A_b}$ be a related tensor field defined on $\mathcal{M}_b$. We will assume that $\mathbf{g_b}$ and $\mathbf{A_b}$ are known.[7] To understand the evolution of perturbations, first, we need to construct a difference between these $\mathbf{A_p}$ and $\mathbf{A_b}$. Since these fields are defined on different manifolds, we must first associate points in $\mathcal{M}_b$ with points in $\mathcal{M}_p$ and then provide a prescription for comparing the tensor fields defined on two different manifolds.

Let $\mathcal{D} : \mathcal{M}_b \to \mathcal{M}_p$ be a diffeomorphism[8] between the two spacetimes. Pick a point B in $\mathcal{M}_b$. The corresponding point in $\mathcal{M}_p$ under $\mathcal{D}$ is $P = \mathcal{D}(B)$. $\mathcal{D}$ naturally induces a map which takes the tensor field $\mathbf{A_p}(P)$ to the point B in $\mathcal{M}_b$ through the pull back map $\mathcal{D}^*\mathbf{A_p}$. Note that $\mathcal{D}^*\mathbf{A_p}$ is a tensor field in $\mathcal{M}_b$. Its action on vectors in the tangent space of some point B in $\mathcal{M}_b$ is equal to the action of the $\mathbf{A_p}$ on the pull back of those vectors to the tangent space at P in $\mathcal{M}_p$. With these tools in hand we can construct the required difference:

$$\delta\mathbf{A}(B) = [\mathcal{D}^*\mathbf{A_p}](B) - \mathbf{A_b}(B). \tag{3.28}$$

This difference is a tensor field defined on $\mathcal{M}_b$. Thus what we mean by a perturbation at a given spacetime point depends on the identification maps between the perturbed and the unperturbed spacetimes.

Now consider a different map $\widetilde{\mathcal{D}}$ such that $\widetilde{\mathcal{D}}(\widetilde{B}) = P$. Under this map, the difference between the pull back of $\mathbf{A_p}(P)$ to $\mathcal{M}_b$ and $\mathbf{A_b}(\widetilde{B})$:

$$\widetilde{\delta\mathbf{A}}(\tilde{B}) = [\widetilde{\mathcal{D}}^*\mathbf{A_p}](\tilde{B}) - \mathbf{A_b}(\tilde{B}). \tag{3.29}$$

We cannot compare $\widetilde{\delta\mathbf{A}}(\tilde{B})$ and $\delta\mathbf{A}(B)$ yet because they are evaluated at different

---

[7] From now on $\mathbf{A}$ can be the metric $\mathbf{g}$ also.

[8] A diffeomorphism is a bijective map between manifolds with the property that both the map and its inverse are differentiable.

points of $\mathcal{M}_b$. So we need the pull back of $\widetilde{\delta\mathbf{A}}(\tilde{B})$ to B which requires a map from $B \rightarrow \widetilde{B}$. Now, the diffeomorphisms $\mathcal{D}, \widetilde{\mathcal{D}} : \mathcal{M}_b \rightarrow \mathcal{M}_p$ are linked by another diffeomorphism $\varphi : \mathcal{M}_b \rightarrow \mathcal{M}_b$. This diffeomorphism is given by $\varphi = \widetilde{\mathcal{D}}^{-1} \cdot \mathcal{D}$ under which $\varphi(B) = \widetilde{B}$. Using φ to pull back $\widetilde{\delta\mathbf{A}}(\tilde{B})$ we get

$$[\varphi^* \widetilde{\delta\mathbf{A}}](B) - \delta\mathbf{A}(B) = -[\varphi^* \mathbf{A_b}](B) + \mathbf{A_b}(B) \tag{3.30}$$

because $[\varphi^* \widetilde{\mathcal{D}}^* \mathbf{A_p}](B) = [\mathcal{D}^* \mathbf{A_p}](B)$. If φ is the integral curve of an infinitesimal vector field ξ, then the above difference can be expressed as the Lie derivative of $\mathbf{A_b}$ with respect to ξ, ie.

$$[\varphi^* \widetilde{\delta\mathbf{A}}](B) - \delta\mathbf{A}(B) = -\mathcal{L}_\xi \mathbf{A_b}(B). \tag{3.31}$$

There were two important steps in deriving equation (3.31). The first was constructing the difference $\delta\mathbf{A}$ between tensors on different manifolds and second was constructing the the difference *between* $\delta\mathbf{A}$ (resulting from different identification maps) at two different points on the same manifold.

In summary, we have shown that in relativistic perturbation theory (i) the perturbation in a field depends on the identification of points between the background spacetime time and the perturbed spacetime. (ii) The difference between perturbations resulting from two different identification maps can be expressed as a Lie derivative of the (known) background field. The choice of the identification map is often called a choice of "gauge" and the transformation that allows us to relate perturbations in different gauges are called gauge transformations.

Gauge Invariance: The perturbation $\delta\mathbf{A}$ is "gauge-invariant" iff $\mathcal{L}_\xi \mathbf{A_b} = 0$ for all ξ (equivalently, all pairs $\mathcal{D}, \widetilde{\mathcal{D}}$), ie. when $\mathbf{A_b} =$ constant on the background.

Co-ordinate View: Let us now write the above expressions (3.28) and (3.31) in component form. The maps, $\mathcal{D}$ and $\widetilde{\mathcal{D}}$ can be thought of as inducing different co-ordinate systems on $\mathcal{M}_p$ in the following sense. Let x^γ and $\tilde{x}^\gamma = x^\gamma + \xi^\gamma$ be the co-ordinates associated with the points $B = \mathcal{D}^{-1}(P)$ and $\widetilde{B} = \widetilde{\mathcal{D}}^{-1}(P)$ in $\mathcal{M}_b$. The point P in $\mathcal{M}_p$ is assigned x^γ and $\tilde{x}^\gamma$ depending on the identification maps $\mathcal{D}$ and $\widetilde{\mathcal{D}}$. In component notation, equation (3.28) becomes

$$\begin{aligned}[\delta\mathbf{A}]^{\mu_1...\mu_n}_{\nu_1...\nu_m}(x^\gamma) &= \frac{\partial x^{\beta_1}}{\partial x^{\nu_1}}...\frac{\partial x^{\beta_m}}{\partial x^{\nu_m}}\frac{\partial x^{\mu_1}}{\partial x^{\alpha_1}}...\frac{\partial x^{\mu_n}}{\partial x^{\alpha_n}}[\mathbf{A_p}]^{\alpha_1...\alpha_n}_{\beta_1...\beta_m}(x^\gamma) - [\mathbf{A_b}]^{\mu_1...\mu_n}_{\nu_1...\nu_m}(x^\gamma) \\ &= [\mathbf{A_p}]^{\mu_1...\mu_n}_{\nu_1...\nu_m}(x^\gamma) - [\mathbf{A_b}]^{\mu_1...\mu_n}_{\nu_1...\nu_m}(x^\gamma),\end{aligned} \tag{3.32}$$

where the first equality results from the definition of the pull back map. The second equality is due of our assigning of the same co-ordinates to B and P. Similarly, the equation (3.31) becomes

$$[\varphi^*\widetilde{\delta\mathbf{A}}]^{\mu_1...\mu_n}_{\nu_1...\nu_m}(x^\gamma) = \frac{\partial \tilde{x}^{\beta_1}}{\partial x^{\nu_1}}...\frac{\partial \tilde{x}^{\beta_m}}{\partial x^{\nu_m}}\frac{\partial x^{\mu_1}}{\partial \tilde{x}^{\alpha_1}}...\frac{\partial x^{\mu_n}}{\partial \tilde{x}^{\alpha_n}}\widetilde{\delta A}^{\alpha_1...\alpha_n}_{\beta_1...\beta_m}(\tilde{x}^\gamma) = \widetilde{\delta A}^{\mu_1...\mu_n}_{\nu_1...\nu_m}(x^\gamma), \tag{3.33}$$

where the first equality is the definition of the pull back map and the last equality follows from our assumption that ξ^γ is infinitesimal. We restrict ourselves to coordinate systems where $[\widetilde{\delta\mathbf{A}}]^{\mu_1...\mu_n}_{\nu_1...\nu_m}$ remain small. Finally we have the following operational way of comparing perturbations in two different gauges (ie. maps $\mathcal{D}, \widetilde{\mathcal{D}}$)

$$\widetilde{\delta A}^{\mu_1...\mu_n}_{\nu_1...\nu_m}(x^\gamma) = \delta A^{\mu_1...\mu_n}_{\nu_1...\nu_m}(x^\gamma) - \mathcal{L}_\xi A^{\mu_1...\mu_n}_{\nu_1...\nu_m}(x^\gamma), \tag{3.34}$$

where

$$\begin{aligned}\mathcal{L}_\xi A^{\mu_1...\mu_n}_{\nu_1...\nu_m} &= \xi^\lambda \partial_\lambda A^{\mu_1...\mu_n}_{\nu_1...\nu_m} \\ &\quad - A^{\lambda...\mu_n}_{\nu_1...\nu_m}\partial_\lambda \xi^{\mu_1} - ... - A^{\mu_1...\lambda}_{\nu_1...\nu_m}\partial_\lambda \xi^{\mu_n} \\ &\quad + A^{\mu_1...\mu_n}_{\lambda...\nu_m}\partial_{\nu_1}\xi^\lambda + ... + A^{\mu_1...\mu_n}_{\nu_1...\lambda}\partial_{\nu_m}\xi^\lambda \\ &= \xi^\lambda \nabla_\lambda A^{\mu_1...\mu_n}_{\nu_1...\nu_m} \\ &\quad - A^{\lambda...\mu_n}_{\nu_1...\nu_m}\nabla_\lambda \xi^{\mu_1} - ... - A^{\mu_1...\lambda}_{\nu_1...\nu_m}\nabla_\lambda \xi^{\mu_n} \\ &\quad + A^{\mu_1...\mu_n}_{\lambda...\nu_m}\nabla_{\nu_1}\xi^\lambda + ... + A^{\mu_1...\mu_n}_{\nu_1...\lambda}\nabla_{\nu_m}\xi^\lambda.\end{aligned} \tag{3.35}$$

For ease of future reference, we write down (3.35) explicitly for scalar, vector and higher rank tensor fields.

- scalar field perturbations φ:

$$\widetilde{\delta\varphi} = \delta\varphi - \xi^\lambda \partial_\lambda \varphi \tag{3.36}$$

- four velocity u_μ

$$\widetilde{\delta u}_\mu = \delta u_\mu - \xi^\lambda \partial_\lambda u_\mu - u_\lambda \partial_\mu \xi^\lambda \tag{3.37}$$

- metric perturbation $\delta g_{\mu\nu}$ we have

$$\widetilde{\delta g}_{\mu\nu} = \delta g_{\mu\nu} - \xi^\lambda \partial_\lambda g_{\mu\nu} - g_{\lambda\nu}\partial_\mu \xi^\lambda - g_{\mu\lambda}\partial_\nu \xi^\lambda \tag{3.38}$$

3.A.2 Classifying perturbations

One can decompose perturbations in tensor field based on how they transform under spatial rotations and translations at a given instant of time. For concreteness, let us decompose perturbations in the metric tensor (on a spatially flat FRW background) . Based on the index structure, it is clear that the metric perturbation δg_{00} behaves like a (spatial) scalar. We will write it as $\delta g_{00} = -2A$. The space-time part, δg_{0i} can be written as a sum of a divergence free and curl free spatial vector $\delta g_{0i} = \partial_i B + B_i$, where $\partial^i B_i = 0$. The space-space part can be written as

$$\delta g_{ij} = a^2 \left[-2\psi \delta_{ij} + \{\partial_i \partial_j - \frac{1}{3}\delta_{ij}\nabla^2\} 2E + 2\partial_{(i}F_{j)} + h_{ij} \right],$$

where $\partial^i F_i = 0$ and $h^i_i = \partial^i h_{ij} = 0$. To make sure we have accounted for all ten components of the metric perturbation, let us count the number of free functions. We have 4 scalar function (A, B, ψ, E), two transverse vectors (B_i, F_i) and one transverse, traceless tensor h_{ij}. (B_i, F_i) contain 4 free functions, and h_{ij} contains 2 free functions. Putting it all together we have 10 free functions as expected for a symmetric 4D matrix.

In cosmological perturbation theory, when talking about scalar, vector and tensor perturbations we are referring to perturbations constructed out of scalar functions, transverse, spatial vectors and transverse, traceless spatial tensors respectively. When using the Einstein equations; scalar, vector and tensor perturbations decouple at linear order.

3.A.3 Scalar metric perturbations

For the most part scalar perturbations are the ones relevant for structure formation, CMB temperature fluctuations etc. For scalar perturbations the perturbed metric is given by

$$ds^2 = -(1+2A)dt^2 + 2\partial_i B dt dx^i + a^2(t)[(1-2\psi)\delta_{ij} + \{\partial_i\partial_j - \frac{1}{3}\delta_{ij}\nabla^2\}2E]dx^i dx^j \tag{3.39}$$

Even when we restrict ourselves to scalar fluctuations, we can simplify the field equations considerably by an appropriate choice of gauge. Here is the general procedure. Like any other perturbation, the components of the infinitesimal vector field ξ^γ in (3.35) can be be written as $\xi^\gamma = (\xi^0, \xi^i)$. The spatial part ξ^i can be further decomposed into a curl free and a divergence free part: $\xi^i = \partial^i\xi + \xi^i_\perp$, where $\partial_i\xi^i_\perp = 0$. For scalar perturbations we are only interested in ξ^0 and $\xi^i = \partial^i\xi$. Under the gauge transformation generated by $\xi^\gamma = (\xi^0, \partial^i\xi)$, the four functions in the metric transform as

$$\begin{aligned}
\tilde{A} &= A - \dot{\xi}^0 \\
\tilde{B} &= B + 2H\xi - \dot{\xi} + \xi^0 \\
\tilde{\psi} &= \psi + H\xi^0 + \frac{\nabla^2}{a^2}\xi \\
\tilde{E} &= E - \frac{\xi}{a^2}
\end{aligned} \tag{3.40}$$

Since the field equations are gauge invariant, we are free to choose ξ^0 and ξ. With the help of these two functions ξ^0 and ξ we can eliminate two out of the four scalar functions in the metric perturbations. A particular choice of these two functions, corresponds to a choice of gauge.

Consider the metric in some arbitrary co-ordinate system (x^γ) defined by the functions A, B, Ψ and E. Now consider the a gauge transformation defined by $\xi = a^2 E$ and $\xi^0 = -(B - a^2\dot{E})$. This choice sets $\tilde{B} = \tilde{E} = 0$. We then define $\Phi \equiv \tilde{A} =$

$A + (B - a^2\dot{E})^{\cdot}$ and $\Psi \equiv \tilde{\psi} = \psi + \nabla^2 E - H\left(B - a^2\dot{E}\right)$ to get the metric in the form

$$ds^2 = -(1+2\Phi)dt^2 + a^2(1-2\Psi)\delta_{ij}dx^i dx^j.$$

This gauge is called the Newtonian gauge. There are a number of benefits in using the Newtonian gauge. First, it is diagonal which simplifies calculations. For the purposes of this chapter the most important aspect is the following. In this gauge, on small scales and in the presence of non-relativistic sources, the perturbed Einstein field equations yield $\Phi = \Psi$ and the usual Poisson equation $\nabla^2\Phi = 4\pi G\rho_m\delta_m$. Similarly, the conservation equations also yield equations similar to their Newtonian counterparts. Hence in this gauge, our intuition from perturbations in "Newtonian" cosmology carries over nicely. [9]

On the other hand one can also work with explicitly gauge invariant variables. The idea is to take combinations of the above transformation equations in such a way that the dependence on ξ^γ is eliminated. We then have equations of the form

$$F(A, B, \psi, E, \dot{A}, \dot{B}\ldots) = F(\tilde{A}, \tilde{B}, \tilde{\psi}, \tilde{E}, \dot{\tilde{A}}, \dot{\tilde{B}}\ldots),$$

where F is a linear function of its arguments. Any such function F is a gauge invariant variable. A particularly useful and complete set of gauge invariant variables is (gauge invariance an be easily checked using equation (3.40)

$$\begin{aligned} \Phi_{\rm GI} &= A + \left(B - a^2\dot{E}\right)^{\cdot} \\ \Psi_{\rm GI} &= \psi + \nabla^2 E - H\left(B - a^2\dot{E}\right) \end{aligned} \tag{3.41}$$

---

[9] For a more physical perspective consider particles at rest with respect to this co-ordinate system. The four velocity (which is normal to the spatial hypersurface) is given by $u^\mu = (1-\Phi, \vec{0})$. One can then check that, these world-lines have no shear, ie.

$$\sigma_{\mu\nu} = \nabla_{(\mu}u_{\nu)} - \frac{\nabla_\gamma u^\gamma}{3}(g_{\mu\nu} - u_\mu u_\nu) = 0.$$

Similarly there is no rotation either. This means that the world lines of particles at rest converge towards or diverge away from each other.

Note that the above gauge invariant variables are the amplitudes of the metric perturbations $\Phi = \tilde{A}$ and $\Psi = \tilde{\psi}$ in the Newtonian gauge. This is another extremely useful feature of the Newtonian gauge. In practical terms, one can simply do the calculation in Newtonian gauge and in the end, then in the end make the replacement $\Psi \to \Psi_{\rm GI}$ and $\Phi \to \Phi_{\rm GI}$ to express the results in an explicitly gauge invariant form. Because of these reasons we exclusively used the Newtonian gauge throughout the chapter. Below we provide a number of formulae in the Newtonian gauge that are quite useful for calculations. For more details on cosmological perturbation theory and different gauge choices see ([42]).

3.A.4 Newtonian gauge: useful formulae

- **metric**: $ds^2 = -(1+2\Phi)dt^2 + a^2(1-2\Psi)\delta_{ij}dx^i dx^j$.

- **Christoffel Symbols**

$$\begin{aligned}
\Gamma^i_{0j} &= H\delta^i_j - \partial_0\Psi\delta^i_j \\
\Gamma^0_{ij} &= a^2 H\delta_{ij} - a^2[\partial_0\Psi + 2H(\Phi+\Psi)]\delta_{ij} \\
\Gamma^0_{00} &= \partial_0\Phi \\
\Gamma^0_{i0} &= \partial_i\Phi \\
\Gamma^i_{00} &= \frac{\partial_i\Phi}{a^2} \\
\Gamma^i_{ji} &= \Gamma^j_{jj} = -\Gamma^j_{ii} = -\partial_j\Psi \qquad i \neq j \\
\Gamma^i_{jk} &= 0 \qquad\qquad\qquad i \neq j \neq k
\end{aligned}$$

- **Conservation equations**

$$\begin{aligned}
&\partial_0\bar{\rho} + 3H(\bar{\rho}+\bar{p}) = 0 \\
&\partial_0\delta T^0_0 + \partial_i\delta T^i_0 + 3H\delta T^0_0 - H\delta T^i_i = -3(\bar{\rho}+\bar{p})\partial_0\Psi \\
&\partial_0\delta T^0_i + \partial_j\delta T^j_i + 3H\delta T^0_i = -(\bar{\rho}+\bar{p})\partial_i\Phi
\end{aligned}$$

where we have ignored the following term $2(\Phi + \Psi)\delta T^0_i$

- **Ricci Tensor**(mixed)

$$
\begin{aligned}
R^0_0 &= 3H^2 q - 3H^2 \left(2q\Phi + \frac{1}{H}\partial_0(\Phi + 2\Psi) + \frac{1}{H^2}\partial^2_0\Psi + \frac{1}{3a^2H^2}\nabla^2\Phi \right) \\
R^0_i &= -2H\partial_i \left(\Phi + \frac{1}{H}\partial_0\Psi \right) \\
R^i_i &= 3H^2(2+q) \\
&\quad - 3H^2 \left[2(2+q)\Phi + \frac{1}{H}\partial_0(\Phi + 6\Psi)\frac{1}{H^2}\partial^2_0\Psi + \frac{1}{3a^2H^2}\nabla^2(\Phi - 4\Psi) \right] \\
R^i_j &= -\frac{1}{a^2}\partial_i\partial_j(\Phi - \Psi) \qquad i \neq j
\end{aligned}
$$

- **Ricci Scalar**

$$
R = 6H^2(1+q) - 2H^2 \left[6(1+q)\Phi + \frac{3}{H}\partial_0(\Phi + 4\Psi) + \frac{3}{H^2}\partial^2_0\Psi + \frac{1}{a^2H^2}\nabla^2(\Phi - 2\Psi) \right]
$$

- **Einstein Tensor**(mixed)

$$
\begin{aligned}
G^0_0 &= -3H^2 + 6H^2 \left(\Phi + \frac{\partial_0\Psi}{H} - \frac{1}{3a^2H^2}\nabla^2\Psi \right) \\
G^0_i &= -a^2 G^i_0 = -2H\partial_i \left(\Phi + \frac{\partial_0\Psi}{H} \right) \\
G^i_i &= -3H^2(1+2q) \\
&\quad + 6H^2 \left[(1+2q)\Phi + \frac{1}{H}\partial_0(\Phi + 3\Psi) + \frac{1}{H^2}\partial^2_0\Psi + \frac{1}{3a^2H^2}\nabla^2(\Phi - \Psi) \right] \\
G^i_j &= -\frac{1}{a^2}\partial_i\partial_j(\Phi - \Psi) \qquad i \neq j
\end{aligned}
$$

$f(a,\vec{x}) = \int f(a,\vec{k})e^{i\vec{k}\cdot\vec{x}}d^3k$. $\vec{x}$ and $\vec{k}$ are co-moving co-ordinates and wave numbers respectively with $\vec{k}\cdot\vec{x} \equiv \Sigma k^i x^i$, $k_i = k^i$ and $k^2 = k_i k^i$. We define $\tilde{k}_i = k_i/aH$. Derivatives with respect to a are denoted by primes.

- **Christoffel Symbols**

$$\begin{aligned}
&\Gamma^i_{0j} = H\delta^i_j - aH\Psi'\delta^i_j \\
&\Gamma^0_{ij} = a^2H\delta_{ij} - a^2H[a\Psi' + 2(\Phi+\Psi)]\delta_{ij} \\
&\Gamma^0_{00} = aH\Phi' \\
&\Gamma^0_{i0} = iaH\tilde{k}_i\Phi \\
&\Gamma^i_{00} = iH\frac{\tilde{k}^i\Phi}{a} \\
&\Gamma^i_{ji} = \Gamma^j_{jj} = -\Gamma^j_{ii} = -iaH\tilde{k}_j\Psi \qquad i \neq j \\
&\Gamma^i_{jk} = 0 \qquad\qquad\qquad\qquad\qquad i \neq j \neq k
\end{aligned}$$

- **Conservation equations**

$$\begin{aligned}
&a\bar{\rho}' + 3(\bar{\rho}+\bar{p}) = 0 \\
&a(\delta T^0_0)' + ia\tilde{k}_i\delta T^i_0 + 3\delta T^0_0 - \delta T^i_i = -3(\bar{\rho}+\bar{p})a\Psi' \\
&a(\delta T^0_i)' + ia\tilde{k}_j\delta T^j_i + 3\delta T^0_i = -(\bar{\rho}+\bar{p})ia\tilde{k}_i\Phi
\end{aligned} \tag{3.42}$$

- **Ricci Tensor**(mixed)

$$\begin{aligned}
&R^0_0 = 3H^2q - 3H^2\left(2q\Phi + a\Phi' + (2+q)a\Psi' + a^2\Psi'' - \frac{1}{3}\tilde{k}^2\Phi\right) \\
&R^0_i = -i2aH^2\tilde{k}_i\left(\Phi + a\Psi'\right) \\
&R^i_i = 3H^2(2+q) \\
&- 3H^2\left[2(2+q)\Phi + a\Phi' + (6+q)a\Psi' + a^2\Psi'' - \frac{1}{3}\tilde{k}^2(\Phi - 4\Psi)\right] \\
&R^i_j = H^2\tilde{k}_i\tilde{k}_j(\Phi - \Psi) \qquad i \neq j
\end{aligned}$$

- **Ricci Scalar**

$$R = 6H^2(1+q) - 2H^2\left[6(1+q)\Phi + 3a\Phi' + 3(4+q)\Psi' + 3a^2\Psi'' - \tilde{k}^2(\Phi - 2\Psi)\right]$$

- **Einstein Tensor**

$$\begin{aligned}
G^0_0 &= -3H^2 + 6H^2\left(\Phi + a\Psi' + \frac{1}{3}\tilde{k}^2\Psi\right)\\
G^0_i &= -a^2 G^i_0 = -i2aH^2\tilde{k}_i\left(\Phi + a\Psi'\right)\\
G^i_i &= -3H^2(1+2q)\\
&\quad + 6H^2\left[(1+2q)\Phi + a\Phi' + (3+q)a\Psi' + a^2\Psi'' - \frac{1}{3}\tilde{k}^2(\Phi - \Psi)\right]\\
G^i_j &= H^2\tilde{k}_i\tilde{k}_j(\Phi - \Psi) \qquad i \neq j
\end{aligned}$$

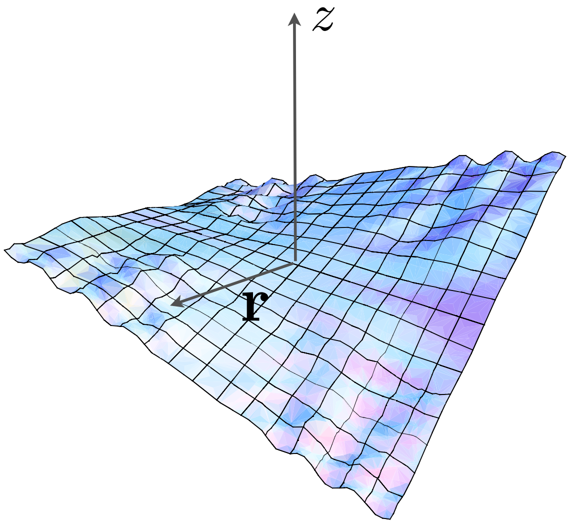

3.B Braneworld perturbations

In this appendix, we wish to carry out a detailed calculation of perturbations in braneworld models. Our main interest is in understanding the odd power of the comoving wave number, k, that are expected to arise in the field equation for braneworld models (see Section 3.3.5 of this chapter). To gain some intuition into the calculation, we first explore braneworld electrostatics as an analogy for braneworld gravity. We then move on to the calculation of Dvali-Gabadase-Porrati (DGP)[41] and Randall Sundrum (RS)[69] braneworld perturbations to sub-leading order in spatial derivatives.

3.B.1 Braneworld electrostatics: An analogy

Let us begin with a lower dimensional case. Consider the following (3+1) dimensional Lagrangian density (with $x^3 = z$)

$$\mathcal{L} = -\frac{1}{16\pi} F^{\mu\nu}_{(3)} F_{(3)\mu\nu} - \delta(z) \left[\frac{2\eta}{16\pi} F^{ab}_{(2)} F_{(2)ab} + \frac{1}{c} J_{(2)a} A^a_{(2)} \right], \tag{3.43}$$

where $\eta = constant$, $[\eta] = L$, $\{\mu, \nu = 0, 1, 2, 3\}$ whereas $\{a, b = 0, 1, 2\}$ and the subscripts "(2)" and "(3)" denote fields defined on the sheet at $z = 0$ and in the full

3-space respectively. The field tensors $F_{(3)\mu\nu}$ and $F_{(2)ab}$ are not independent. They are related by $F_{(2)ab} = \delta^\mu_a \delta^\nu_b F_{(3)\mu\nu}|_{z=0}$. For the above lagrangian density, the field equations are given by

$$-\partial_\mu F^{\mu b}_{(3)} - \delta(z)\left[2\eta\partial_a F^{ab}_{(2)} - \frac{4\pi}{c}J^b_{(2)}\right] = 0. \tag{3.44}$$

For $b = 0$, with $F^{i0} \equiv E^i$ and $J^0 \equiv c\,\sigma(\mathbf{r})$ with $\mathbf{r} = x\hat{\imath} + y\hat{\jmath}$ and assuming static configurations, equation (3.44) yields

$$\nabla \cdot \mathbf{E}_{(3)} + \delta(z)\left[2\eta\nabla_{\mathbf{r}} \cdot \mathbf{E}_{(2)} - 4\pi\sigma\right] = 0, \tag{3.45}$$

where $\nabla = \hat{\imath}\partial_x + \hat{\jmath}\partial_y + \hat{k}\partial_z$ and $\nabla_{\mathbf{r}} = \hat{\imath}\partial_x + \hat{\jmath}\partial_y$. The 2D and 3D fields are related by $\mathbf{E}_{(2)x} = \mathbf{E}_{(3)x}|_{z=0}, \mathbf{E}_{(2)y} = \mathbf{E}_{(3)y}|_{z=0}$. Now, for $z \neq 0$ we get the usual Gauss' law.

$$\nabla \cdot \mathbf{E}_{(3)} = 0 \qquad z \neq 0. \tag{3.46}$$

We integrate the equation (3.45) across the $z = 0$ surface to get

$$E_{(3)z} = 2\pi\sigma - \eta(\partial_x E_{(2)x} + \partial_y E_{(2)y}) \qquad z = 0. \tag{3.47}$$

As usual, we define a potential function Φ corresponding to the fields: $\mathbf{E}_{(2)} = -\nabla_{\mathbf{r}}\Phi(\mathbf{r}, z = 0)$ and $\mathbf{E}_{(3)} = -\nabla\Phi(\mathbf{r}, z)$. Then equations (3.46) and (3.47) yield

$$\begin{aligned} \nabla^2\Phi &= 0 \qquad z \neq 0, \\ \partial_z\Phi &= -2\pi\sigma - \eta\nabla^2_{\mathbf{r}}\Phi \qquad z = 0. \end{aligned} \tag{3.48}$$

Note: *The junction condition yields a relationship between the "off-brane"(linear) and "in-brane" derivatives.*

Let $\sigma(\mathbf{r}) = \sigma_0 + \int d^2\mathbf{k}\,\sigma_{\mathbf{k}} e^{i\mathbf{k}\cdot\mathbf{r}}$ and $\Phi(\mathbf{r}, z) = -2\pi\sigma_0 z + \int d^2\mathbf{k}\,\Phi_{\mathbf{k}}(z)e^{i\mathbf{k}\cdot\mathbf{r}}$. This yields

$$\begin{aligned} \left(\partial_z^2 - k^2\right)\Phi_{\mathbf{k}} &= 0 \qquad z \neq 0. \\ \partial_z\Phi_{\mathbf{k}} &= -2\pi\sigma_{\mathbf{k}} + \eta k^2\Phi_{\mathbf{k}} \qquad z = 0. \end{aligned} \tag{3.49}$$

A solution is given by

$$\Phi_{\mathbf{k}}(z) = 2\pi\eta \frac{e^{-k|z|}}{(k\eta)^2 + (k\eta)} \sigma_{\mathbf{k}}. \tag{3.50}$$

For small scales, we get

$$\Phi_{\mathbf{k}} = \frac{2\pi\eta}{(k\eta)^2} \sigma_{\mathbf{k}} \left[1 - \frac{1}{(k\eta)} + \ldots\right] \qquad z = 0,\ k\eta \gg 1. \tag{3.51}$$

Note that we get an odd power of k as the leading order correction to the Poisson equation on the brane. This same feature will be carried over in the DGP scenario (as is shown next)[10]. The reason that the off-brane derivative introduces an on-brane linear power of k is because of the bulk field equation, which enforces $\partial_z \sim k$. In the braneworld models the Israel junction conditions on the brane yield

$$\partial_y g_{\mu\nu} = \kappa_{(5)}^2 \left(\mathcal{G}_{\mu\nu} - \frac{1}{3} \mathcal{G} g_{\mu\nu} \right), \tag{3.52}$$

where $\kappa_{(5)}$ is the bulk gravitational coupling and $\mu, \nu = 0, 1, 2, 3$. The linear derivative, ∂_y, is normal to the brane. The tensor $\mathcal{G}_{\mu\nu}$ represents an effective energy momentum tensor on the brane. For the case of DGP it is given by $\kappa^{-2}\left(G_{\mu\nu} - \kappa^2 T_{\mu\nu}\right)$ where κ is the 4D gravitational coupling, $G_{\mu\nu}$ is the 4D Einstein tensor and $T_{\mu\nu}$ is the energy momentum tensor of matter on the brane. Again, the important feature is that there is a relationship between the offbrane, linear y-derivative and the in brane derivatives (present in $G_{\mu\nu}$ and G). Along with $G_{AB} = 0$ $(A, B = 0, 1, 2, 3, y = 4)$ in the bulk, arguments similar to the ones used for the electrostatics case yields the odd k dependence. We turn to the detailed calculation in the subsequent sections.

3.B.2 Braneworld perturbations: Details

In the following, we obtain the matter-metric relation to sub-leading order in spatial derivatives. Following [54] we will consider an action of the following form for

---

[10] The RS scenario is discussed in the last section of this appendix

braneworld models:

$$S = \frac{1}{2\kappa_{(5)}^2}\int d^5x\sqrt{-g_{(5)}}\left[R_{(5)} - 2\Lambda_{(5)}\right] + \int d^4x\sqrt{-g}\mathcal{L}_{\rm eff}, \tag{3.53}$$

where $\mathcal{L}_{\rm eff}$ is the effective Lagrangian on the brane (see below for explicit examples). The brane energy momentum tensor corresponding to this effective brane lagrangian is defined as

$$\mathcal{G}_{\mu\nu} = -\frac{2}{\sqrt{-g}}\frac{\delta}{\delta g^{\mu\nu}}\int d^4x\sqrt{-g}\mathcal{L}_{\rm eff}. \tag{3.54}$$

In the bulk, the field equations are given by

$$G^A_B + \Lambda_{(5)}\delta^A_B = 0$$

where $A, B = 0, 1, 2, 3, 4$. In addition the metric must also satisfy the Israel Junction condition at the location of the brane. This is given by

$$K^\mu_\nu = \frac{\kappa_{(5)}^2}{2}\left(\mathcal{G}^\mu_\nu - \frac{1}{3}\mathcal{G}\delta^\mu_\nu\right) \tag{3.55}$$

where K^μ_ν is the extrinsic curvature of the brane and $\mathcal{G} = \mathrm{Tr}[\mathcal{G}^\mu_\nu]$. We have assumed Z_2 symmetry about the brane and $\mu, \nu = 0, 1, 2, 3$.[11]

Although we will try to keep our arguments as general as possible, as explicit examples, we will consider the DGP and RS models. DGP modified gravity on cosmological scales whereas RS does the same on sub millimeter scales.

To carry out the calculation will need the Einstein tensor in the bulk, the extrinsic curvature and the effective energy momentum tensor. The form of first two is independent of the model under consideration. So we shall calculate them first. Then we will calculate the effective energy momentum tensor for the DGP and RS models. Finally we will put these tensors into the field equations and the junction conditions to obtain the desired matter metric relation at sub-leading order in spatial derivatives.

---

[11] For κ, Λ, g, R etc. when the subscript (5) is not used, we are referring to their 4D values.

Einstein tensor and extrinsic curvature tensor

Consider a metric of the form (see [70])

$$ds^2 = -N^2(1+2\Phi)dt^2 + A^2(1-2\Psi)\delta_{ij}dx^i dx^j + 2l\partial_i\varphi dx^i dy + (1+2\Gamma)dy^2 \tag{3.56}$$

where $N = N(t,y), A = A(t,y)$ and the others functions: Φ, Ψ, φ and Γ depend on all five co-ordinates. l is a constant ([l]=length) which we will choose based on the problem under consideration. The brane is located at $y = 0$. To recover the perturbed FRW metric in Newtonian gauge on the brane, we require $A(t,0) = a(t)$ and $N(t,0) = 1$. The Einstein tensor upto linear order in the perturbations is given by (" prime "$= \partial_y$ and "dot"$= \partial_t$)

$$\begin{aligned}
G^0_0 &= 3\left[\left(\frac{A'}{A}\right)^2 + \frac{A''}{A} - \frac{1}{N^2}\left(\frac{\dot{A}}{A}\right)^2\right] \\
&\quad - 3\Psi'' + \frac{\nabla^2}{A^2}\left(\Gamma - l\varphi' - 2l\frac{A'}{A}\varphi - 2\Psi\right) - 3\frac{A'}{A}\left(\Gamma' + 4\Psi'\right) \\
&\quad - 6\left\{\frac{A''}{A} + \left(\frac{A'}{A}\right)^2\right\}\Gamma + \frac{6}{N^2}\left(\frac{\dot{A}}{A}\right)^2\Phi - \frac{3}{N^2}\frac{\dot{A}}{A}\left(\dot{\Gamma} - 2\dot{\Psi}\right) \\
G^0_y &= \frac{3}{N^2}\left[\frac{\dot{A}'}{A} - \frac{\dot{A}}{A}\frac{N'}{N}\right] \\
&\quad - \frac{1}{2N^2}\left(l\frac{\nabla^2}{A^2}\varphi' + 6\frac{\dot{A}}{A}(\Phi' + \Psi') + 6\dot{\Psi}'\right) \\
&\quad + \frac{6}{N^2}\frac{N'}{N}\frac{\dot{A}}{A}\Phi - \frac{3}{N^2}\left\{\frac{A'}{A}\dot{\Gamma} + \left(\frac{A'}{A} - \frac{N'}{N}\right)\dot{\Psi}\right\} \\
G^0_i &= \frac{l}{2N^2}\partial_i\left[2\varphi' - \dot{\varphi}'\right] + \frac{1}{N^2}\partial_i\left[\dot{\Gamma} - 2\dot{\Psi} - \frac{\dot{A}}{A}(\Gamma + 2\Phi)\right. \\
&\quad \left. + l\left(\left\{2\frac{A'}{A}\frac{\dot{N}}{N} - \frac{\dot{A}}{A}\frac{N'}{N} + \frac{\dot{A}'}{A}\right\}\varphi + \frac{1}{2}\left\{-3\frac{A'}{A} + \frac{N'}{N}\right\}\dot{\varphi}\right)\right] \\
G^i_j &= -\frac{\partial_i\partial_j}{A^2}\left(\Gamma - l\varphi' - l\left\{\frac{A'}{A} + \frac{N'}{N}\right\}\varphi + \Phi - \Psi\right)
\end{aligned} \tag{3.57}$$

$$\begin{aligned}
G^y_y = {} & 3\left[\left(\frac{A'}{A}\right)^2 + \frac{A'}{A}\frac{N'}{N} + \frac{1}{N^2}\frac{\dot{A}}{A}\frac{\dot{N}}{N} - \frac{1}{N^2}\left\{\left(\frac{\dot{A}}{A}\right)^2 + \frac{\ddot{A}}{A}\right\}\right] \\
& + \frac{\nabla^2}{A^2}\left(\Phi - 2\Psi - l\left\{\frac{N'}{N} + 2\frac{A'}{A}\right\}\varphi\right) - 3\frac{A'}{A}(\Phi' - 2\Psi') - 3\frac{N'}{N}\Psi' \\
& + \frac{6}{N^2}\left\{\left(\frac{\dot{A}}{A}\right)^2 + \frac{\ddot{A}}{A} - \frac{\dot{A}}{A}\frac{\dot{N}}{N}\right\}\Phi - \frac{6}{N^2}\left\{\left(\frac{A'}{A}\right)^2 + \frac{A'}{A}\frac{N'}{N}\right\}\Gamma \\
& + \frac{3}{N^2}\frac{\dot{A}}{A}\left(\dot{\Phi} + 4\dot{\Psi}\right) + \frac{\ddot{\Psi}}{N^2} \\
G^i_i = {} & 3\left[\left(\frac{A'}{A}\right)^2 + 2\frac{A''}{A} + \left\{2\frac{A'}{A}\frac{N'}{N} + \frac{N''}{N}\right\} + \frac{2}{N^2}\frac{\dot{A}}{A}\frac{\dot{N}}{N} - \frac{1}{N^2}\left\{\left(\frac{\dot{A}}{A}\right)^2 + 2\frac{\ddot{A}}{A}\right\}\right] \\
& + 2\frac{\nabla^2}{A^2}\left(\Gamma - l\varphi' + \Phi - \Psi - l\left\{\frac{A'}{A} + \frac{N'}{N}\right\}\varphi\right) + 3(\Phi'' - 2\Psi'') \\
& - 3\frac{N'}{N}(\Gamma' + 2\Psi' - 2\Phi') - 6\frac{A'}{A}(\Gamma' - \Phi' + 3\Psi') \\
& - 6\left\{\left(\frac{A'}{A}\right)^2 + 2\frac{A'}{A}\frac{N'}{N} + 2\frac{A''}{A} + \frac{N''}{N}\right\}\Gamma + \frac{6}{N^2}\left\{\left(\frac{\dot{A}}{A}\right)^2 - 2\frac{\dot{A}}{A}\frac{\dot{N}}{N} + 2\frac{\ddot{A}}{A}\right\}\Phi \\
& + \frac{3}{N^2}\left\{\frac{\dot{N}}{N} - 2\frac{\dot{A}}{A}\right\}\dot{\Gamma} + \frac{6}{N^2}\frac{\dot{A}}{A}\dot{\Phi} + \frac{6}{N^2}\left\{3\frac{\dot{A}}{A} - \frac{\dot{N}}{N}\right\}\dot{\Psi} - \frac{3}{N^2}\left\{\ddot{\Gamma} - 2\ddot{\Psi}\right\} \\
G^y_i = {} & -\partial_i(\Phi' - 2\Psi') + \partial_i\left[\left\{\frac{A'}{A} - \frac{N'}{N}\right\}\Phi + \left\{2\frac{A'}{A} + \frac{N'}{N}\right\}\Gamma\right. \\
& \left. - \frac{l}{N^2}\left(\left\{\frac{\ddot{A}}{A} - \frac{\dot{A}}{A}\frac{\dot{N}}{N} + 2\left(\frac{\dot{A}}{A}\right)^2\right\}\varphi - \frac{1}{2}\left\{\frac{\dot{A}}{A} - \frac{\dot{N}}{N}\right\}\dot{\varphi} + \frac{1}{2}\ddot{\varphi}\right)\right]
\end{aligned}$$

The extrinsic curvature is defined as[12]

$$K^\mu_\nu = \nabla_\nu n^\mu,$$

---

[12] In the case of Gaussian-normal co-odinates adapted to the brane, the extrinsic curvature is defined as $K_{\mu\nu} = \frac{1}{2}\partial_y g_{\mu\nu}$.

where n^μ is the normal to the brane. For the metric (3.56), the normal is given by $n^\mu = (0, lA^{-2}\partial_i\varphi, 1-\Gamma)$. Explicitly, the extrinsic curvature on the brane upto linear order in the perturbations is given by

$$\begin{aligned} K^0_0 &= \frac{N'}{N} + \Phi' + \Gamma\frac{N'}{N}, \\ K^i_i &= 3\frac{A'}{A} + l\frac{\nabla^2}{a^2}\varphi - 3(\Psi' + \Gamma\frac{A'}{A}), \\ K^i_j &= l\frac{\partial_i\partial_j}{a^2}\varphi. \end{aligned} \tag{3.58}$$

To make further progress we need $\mathcal{G}^\mu_\nu$. The form of $\mathcal{G}^\mu_\nu$ depends on the model under consideration. Let us first concentrate on the DGP model.

Large scale modification of gravity: DGP model:

For this model, $\Lambda_{(5)} = 0$ in the action (3.53) and

$$\mathcal{L}_{\text{eff}} = \frac{1}{2\kappa^2}R - \mathcal{L}_m, \tag{3.59}$$

where $\mathcal{L}_m$ is the lagrangian for non-relativistic dark matter (for simplicity). The field equations in the bulk are given by

$$G^A_B = 0.$$

For this model a length scale is defined by the ratio of the gravitational coupling in the bulk and the brane

$$l = r_c = \frac{\kappa^2_{(5)}}{2\kappa^2}.$$

In what follows we take $r_c \sim \mathcal{O}[H_0^{-1}]$ which is required for consistency with the expansion history. One of the solutions in this model allows for cosmic acceleration and is referred to as the self-accelerated solution. Note that gravity becomes 5D at scales comparable to and larger than r_c.

The effective energy momentum tensor defined by equations (3.54) and (3.59) is

$$\mathcal{G}^\mu_\nu = \kappa^{-2}\left(G^\mu_\nu - \kappa^2 T^\mu_\nu\right),$$

where T^μ_ν is the matter energy momentum tensor. For the r.h.s of the Israel junction conditions we need $\mathcal{G}^\mu_\nu - \frac{1}{3}\mathcal{G}\delta^\mu_\nu$ which on the brane is given by (upto the order $\mathcal{O}[\nabla^2\Phi]$):

$$\begin{aligned}
\kappa^2\left(\mathcal{G}^0_0 - \frac{1}{3}\mathcal{G}\delta^0_0\right) &= -H^2(1-2q) + \frac{2}{3}\kappa^2\rho_m + \frac{2}{3}\left[-\frac{\nabla^2}{a^2}(\Phi+\Psi) + \kappa^2\rho_m\delta_m\right], \\
\kappa^2\left(\mathcal{G}^i_i - \frac{1}{3}\mathcal{G}\delta^i_i\right) &= 3H^2 - \kappa^2\rho_m + 2\frac{\nabla^2}{a^2}\Psi - \kappa^2\rho_m\delta_m, \\
\kappa^2\left(\mathcal{G}^i_j - \frac{1}{3}\mathcal{G}\delta^i_j\right) &= -\frac{\partial_i\partial_j}{a^2}(\Phi-\Psi). \qquad\qquad i \neq j
\end{aligned} \tag{3.60}$$

We now have all the essential ingredients for obtaining the matter metric relation. The field equations in the bulk , $G^A_B = 0$, are satisfied by (at the background level)

$$A = a(1+Hy) \quad \text{and} \quad N = (1+Hqy).$$

Now we move on to the perturbed junction condition[13]. The junction condition up to sub-leading order in the spatial derivatives yields (see equations (3.55, 3.58, 3.60))

$$\begin{aligned}
\Phi' &= \frac{2r_c}{3}\left[-\frac{\nabla^2}{a^2}(\Phi+\Psi) + \kappa^2\rho_m\delta_m\right], && 0-0 \\
\varphi &= \Psi - \Phi, && i \neq j \\
\Psi' &= \frac{r_c}{3}\left[\frac{\nabla^2}{a^2}\varphi - 2\frac{\nabla^2}{a^2}\Psi + \kappa^2\rho_m\delta_m\right]. && i-i
\end{aligned} \tag{3.62}$$

Combining the above three equations one gets $\Phi' - 2\Psi' = 0$. Fourier transforming

---

[13] The Israel junction condition (using the background parts of the *ii* equations in (3.58, 3.60)), we get the modified Friedmann equation

$$H^2 - \frac{H}{r_c} = \frac{\kappa^2}{3}\rho_m \tag{3.61}$$

Note that for $r_c H \ll 1$ we recover the usual Friedmann equation.

the above equations, and using $i \neq j$ equation in $i - i$ equation we have

$$\begin{aligned} \Psi' &= \frac{r_c}{3}\left[\frac{k^2}{a^2}(\Phi+\Psi) + \kappa^2\rho_m\delta_m\right], \\ \Phi' - 2\Psi' &= 0. \end{aligned} \tag{3.63}$$

To eliminate Ψ' we need another expression involving Ψ', Φ and Ψ. This is provided by the solution to a "wave" equation for Ψ in the bulk (obtained below). Also, to obtain, Φ and Ψ independently in terms of δ_m we need another equation relating Φ and Ψ. This additional equation is also provided by the bulk field equations, which we turn to next.

In the bulk $\delta G^A_B = 0$ (refer to (3.57)). Starting with $\delta G^0_0 = 0$, eliminating $\Gamma - r_c\varphi'$ using $\delta G^i_j = 0$ and then using $\delta G^y_y = 0$ to eliminate Φ we get

$$\Psi'' + \frac{\nabla^2}{A^2}\left(\Psi + r_c\frac{A'}{A}\varphi\right) + \frac{A'}{A}\left(\Gamma' + 4\Psi'\right) + \frac{A'}{A}(\Phi' - 2\Psi') + \frac{N'}{N}\Psi' = 0.$$

Now from $\delta G^y_i = 0$ we see that $\Phi' - 2\Psi' \sim \mathcal{O}[\Phi]$ so we drop this term. This leaves us with

$$\Psi'' + \frac{\nabla^2}{A^2}\left(\Psi + r_c\frac{A'}{A}\varphi\right) + \frac{A'}{A}\left(\Gamma' + 4\Psi'\right) + \frac{N'}{N}\Psi' = 0. \tag{3.64}$$

We collect two important equations. These are $\delta G^y_y = 0$ and equation (3.64). To sub-leading order in the spatial derivatives, the fourier transformed equations yield

$$\begin{aligned} &\Psi'' - \frac{k^2}{A^2}\left(\Psi + r_c\frac{A'}{A}\varphi\right) + \frac{A'}{A}\left(\Gamma' + 4\Psi'\right) + \frac{N'}{N}\Psi' = 0, \\ &\frac{k^2}{A^2}\left(\Phi - 2\Psi - r_c\left\{\frac{N'}{N} + 2\frac{A'}{A}\right\}\varphi\right) + 3\frac{N'}{N}\Psi' = 0. \end{aligned} \tag{3.65}$$

We need equation (3.64) only upto *leading* order in the spatial derivatives;

$$\Psi'' - \frac{k^2}{A^2}\left(\Psi + r_c\frac{A'}{A}\varphi\right) = 0, \tag{3.66}$$

which can be solved up to leading order in k to obtain

$$\Psi = c_1(1+Hy)^{-k/aH} + r_c \frac{A'}{A}\varphi. \tag{3.67}$$

This implies that

$$\Psi'|_{y=0} = -\frac{k}{a}(\Psi - r_c H\varphi)|_{y=0}. \tag{3.68}$$

Note that the off-brane derivative provides an odd power of k. On the other hand from $\delta G^y_y = 0$ we get,

$$\Phi - 2\Psi - r_c \left\{ \frac{N'}{N} + 2\frac{A'}{A} \right\} \varphi + 3\frac{N'}{N}\Psi' = 0, \tag{3.69}$$

which when evaluated on the brane, yields

$$\Phi - 2\Psi - r_c H(2+q)\varphi + 3Hq\Psi' = 0. \tag{3.70}$$

Now we are ready to write down a complete set of equations that allow us to read off the matter-metric relationship to sub-leading order in spatial derivatives (using equations (3.63, 3.68, 3.70))

$$\begin{aligned}
\Psi' &= \frac{r_c}{3}\left[\frac{k^2}{a^2}(\Phi+\Psi) + \kappa_4^2\rho_m\delta_m\right] \\
\Psi' &= -\frac{k}{a}(\Psi - r_c H(\Phi - \Psi)) \\
\frac{k^2}{a^2}&\left[\Phi - 2\Psi - r_c H(2+q)(\Phi-\Psi)\right] + 3Hq\Psi' = 0
\end{aligned} \tag{3.71}$$

The above equations can be rearranged in the form

$$\begin{aligned}
\Phi &= -\frac{4\pi G\rho_m\delta_m}{H^2}\left(\frac{aH}{k}\right)^2\left[\beta_0 + \beta_1\left(\frac{aH}{k}\right) + ...\right] \\
\Psi &= -\frac{4\pi G\rho_m\delta_m}{H^2}\left(\frac{aH}{k}\right)^2\left[\gamma_0 + \gamma_1\left(\frac{aH}{k}\right) + ...\right]
\end{aligned} \tag{3.72}$$

where[14]

$$\begin{aligned}\beta_0 &= \frac{4-2Hr_c(2+q)}{3-2Hr_c(2+q)},\\ \gamma_0 &= \frac{2-2Hr_c(2+q)}{3-2Hr_c(2+q)},\\ \beta_1 &= \frac{12(1-Hr_c)(1-Hr_c(3+q))}{Hr_c(3-2Hr_c(2+q))^2},\\ \gamma_1 &= \frac{6(1-2Hr_c(1+q))(1-Hr_c(3+q))}{Hr_c(3-2Hr_c(2+q))^2}.\end{aligned} \tag{3.73}$$

Thus we have explicitly obtained the matter-metric relationship in for the DGP model upto subleading order in spatial derivatives. As expected, there is a linear power of k due to the Israel junction condition. Note that $\beta_1(aH/k), \gamma_1(aH/k) \sim \mathcal{O}[1] \times (a/r_c k)$, so essentially we are expanding in powers of $(a/r_c k)$. We suspect that for any braneworld model that modifies gravity on Hubble scales ($l \gtrsim H^{-1}$), the matter-metric relation in Fourier space will involve an odd power of a/lk. This provides a possibly unique signature of such braneworld models.

We now provide a similar calculation for the RS model that modifies gravity on small scales ($\Lambda \lesssim$ mm). We take a slightly different approach to the calculation, and use the results from [54] directly to read off the coefficient functions.

Small scale modifications: RS model

Let us consider braneworld models which modify gravity on small scales ($\sim l$) and investigate their impact on linear, cosmological perturbations. We are interested in scales a/k such that

$$l \ll \frac{a}{k} \ll H^{-1}$$

with the requirement that a poisson equation be recovered on intermediate ($\sim$ mm to cluster scales). This is a bit silly since linearity certainly does not hold on these scales. Also we expect the scale $l \lesssim 0.1$mm to evade laboratory tests, which means it will have a negligible effect on cosmological scales. However, the purpose of this exercise is to gain insight into how the odd k term might (or might not) enter into the

---

[14] The coefficient functions (β_1, γ_1) derived above do not agree with the ones derived from [54]. We suspect that this is due a different choice of gauge.

equations when the modification to GR is on small scales rather than Hubble scales (as in the case of DGP). We expect the following form for the perturbed matter-metric relation:

$$\begin{aligned}\Phi &= -\frac{4\pi G\rho_m\delta_m}{H^2}\left(\frac{aH}{k}\right)^2\left[\bar{\beta}_0+\bar{\beta}_1\left(l\frac{k}{a}\right)+...\right]\\ \Psi &= -\frac{4\pi G\rho_m\delta_m}{H^2}\left(\frac{aH}{k}\right)^2\left[\bar{\gamma}_0+\bar{\gamma}_1\left(l\frac{k}{a}\right)+...\right]\end{aligned} \tag{3.74}$$

since the modifications are coming in from small scales. Compare this with the form used when the modification is expected to come in at Hubble scales

$$\begin{aligned}\Phi &= -\frac{4\pi G\rho_m\delta_m}{H^2}\left(\frac{aH}{k}\right)^2\left[\beta_0+\beta_1\left(\frac{aH}{k}\right)+...\right]\\ \Psi &= -\frac{4\pi G\rho_m\delta_m}{H^2}\left(\frac{aH}{k}\right)^2\left[\gamma_0+\gamma_1\left(\frac{aH}{k}\right)+...\right]\end{aligned} \tag{3.75}$$

We will calculate these coefficients $(\bar{\beta}_n, \bar{\gamma}_n)$ in the Randall Sundrum model (no cosmic acceleration here), whose action is given by (3.53) with

$$\mathcal{L}_{\text{eff}} = -\frac{\Lambda}{\kappa^2} - \mathcal{L}_m. \tag{3.76}$$

For this model

$$l = r_{(5)} = \frac{\kappa_{(5)}^2}{\kappa^2} = \sqrt{-6\Lambda_{(5)}^{-1}} = \sqrt{6\Lambda^{-1}}.$$

This fine tuning of parameters is essential for recovering standard gravity. The background metric in the bulk has the form

$$N(t,y) = e^{-y/r_{(5)}} \quad \text{and} \quad A(t,y) = a(t)e^{-y/r_{(5)}}.$$

Note that we have ignored terms of order $r_{(5)}^2\kappa^2\rho_m \ll 1$ which is required for a standard matter dominated era and follows from $r_{(5)} \ll H^{-1}$. This is a pretty good approximation (we are making errors of the order $(r_{(5)}H)^2$). We will continue this approximation in the perturbation equations below as well. The strong warping of the brane near the bulk localizes low momentum modes and thus allows recovery of standard gravity at scales which are large compared to $r_{(5)}$.

We will calculate the coefficients using the results in (equation $107-109$ in [54]). First we tweek the equations $(107-109)$ in [54]) to make them more transparent. We rearrange the terms in such a way that the terms that are expected to be largest, appear first (remember $r_{(5)} \ll a/k \ll H^{-1}$). The equations are

$$\begin{aligned}
\Phi &= \frac{1}{2a}\left[\frac{1}{r_{(5)}^2}\left(\Omega + r_{(5)}\partial_y\Omega\right) - \frac{2}{3}\frac{k^2}{a^2}\Omega + 2H\partial_t\Omega - \partial_t^2\Omega\right],\\
\Psi &= \frac{1}{2a}\left[\frac{1}{r_{(5)}^2}\left(\Omega + r_{(5)}\partial_y\Omega\right) - \frac{1}{3}\frac{k^2}{a^2}\Omega + H\partial_t\Omega\right], \qquad (3.77)\\
\kappa^2\delta\rho_m &= \frac{1}{a}\left[-\frac{1}{r_{(5)}^2}\frac{k^2}{a^2}\left(\Omega + r_{(5)}\partial_y\Omega\right) - \frac{3}{r_{(5)}^2}H\partial_t\left(\Omega + r_{(5)}\partial_y\Omega\right)\right].
\end{aligned}$$

To get the above form, we have assumed that the time evolution happens on Hubble scales and $r_{(5)}\partial_y\Omega \sim \Omega$. Ω is the Mukhoyama master variable [71], which satisfies the following wave equation

$$\partial_t\left(\frac{1}{NA^3}\partial_t\Omega\right) + \left(-\frac{1}{r_{(5)}^2} + \frac{k^2}{A^2}\right)\frac{N}{A^3}\Omega - \partial_y\left(\frac{N\partial_y\Omega}{A^3}\right) = 0.$$

Even without solving the Mukhoyama master equation, we can see that from the first terms in the expressions for Φ, Ψ and $\delta\rho_m$, ie. terms linear in $\Omega + r_{(5)}\partial_y\Omega$, we recover "Newtonian" gravity with $\bar{\beta}_0 = \bar{\gamma}_0 = 1$. To make further progress we require an understanding of the solution to the master equation for Ω. Let us first solve the master equation under the assumption the $\partial_t\Omega \sim H\Omega$ and $k^2/A^2 \approx k^2/a^2$ near the brane. In this case it is easy to write down the solution as

$$\Omega \propto \exp\left[-\left(1 - r_{(5)}\frac{k}{a}\right)\frac{y}{r_{(5)}}\right]$$

which yields

$$\Omega + r_{(5)}\partial_y\Omega = r_{(5)}\frac{k}{a}\Omega.$$

It is worth noting that $\partial_y\Omega = -r_{(5)}^{-1}\Omega$ at lowest order. We need to keep the next order term to get the $k-$dependence. Nevertheless, this term is still much larger than

$r_{(5)}k^2/a^2$. With the above result we rewrite the expression for Φ, Ψ and $\delta\rho_m$ as

$$\begin{aligned}
\Phi &= \frac{1}{2ar_{(5)}}\frac{k}{a}\Omega\left[1 - \frac{2r_{(5)}}{3}\frac{k}{a} + ...\right], \\
\Psi &= \frac{1}{2ar_{(5)}}\frac{k}{a}\Omega\left[1 - \frac{r_{(5)}}{3}\frac{k}{a} + ...\right], \\
\kappa^2\delta\rho_m &= -\frac{1}{ar_{(5)}}\frac{k^3}{a^3}\Omega\left[1 + 3\frac{a^2}{k^2}H\partial_t \ln \Omega a^{-1}\right].
\end{aligned} \tag{3.78}$$

We leave the evaluation of $\partial_t \ln \Omega a^{-1}$ for later (we expect it to be $\mathcal{O}[H]$). Moreover we do not need it to calculate $\bar{\beta}_1$ and $\bar{\gamma}_1$.

Combining the above expressions we get

$$\begin{aligned}
\Phi &= -\frac{4\pi G\rho_m}{H^2}\delta_m\left(\frac{aH}{k}\right)^2\left[1 - \frac{2r_{(5)}}{3}\frac{k}{a} - 3\left(\frac{aH}{k}\right)^2\frac{1}{H}\partial_t \ln \Omega a^{-1} + \dots\right], \\
\Psi &= -\frac{4\pi G\rho_m}{H^2}\delta_m\left(\frac{aH}{k}\right)^2\left[1 - \frac{r_{(5)}}{3}\frac{k}{a} - 3\left(\frac{aH}{k}\right)^2\frac{1}{H}\partial_t \ln \Omega a^{-1} + \dots\right].
\end{aligned} \tag{3.79}$$

This allows us to read off our coefficients $(\bar{\beta}_n, \bar{\gamma}_n)$ which are as follows

$$\begin{aligned}
\bar{\beta}_0 &= \bar{\gamma}_0 = 1, \\
\bar{\beta}_1 &= 2\bar{\gamma}_1 = -\frac{2}{3}.
\end{aligned} \tag{3.80}$$

As a bonus, we can also read off the coefficients (β_n, γ_n) which are

$$\begin{aligned}
\beta_0 &= \gamma_0 = 1, \\
\beta_1 &= \gamma_1 = 0, \\
\beta_2 &= \gamma_2 = -3H^{-1}\partial_t \ln \Omega a^{-1}.
\end{aligned} \tag{3.81}$$

Of course as expected, on cosmological scales, the corrections from the small scales is irrelevant.

For the sake of completeness it might seem useful to construct a two parameter expansion (lk/a) and (aH/k) as the expansion scales. Though, this is not too important since the small scale ($l \lesssim 0.1$mm) will have no effect on cosmological scales where linear perturbation theory in density is valid at late time. To make use of both scales one might have to go to the early universe. Another possibility is that dark matter alone feels this extra dimension in which the scale l can be as large as the galactic scale or cluster scale. This needs further consideration and is beyond the scope of this thesis.

In summary, we have calculated the matter metric-relation in braneworld models up to the leading correction to Poisson's equation. After discussing the importance of the Israel Junction conditions, we considered two models as examples: the DGP model modifies gravity on Hubble scales whereas the RS model does so on sub-millimeter scales. We have shown that the Israel junction condition leads to an odd power of k in the matter-metric relation, providing an exciting signature of braneworld models.

Bibliography 3

[1] Adam G. Riess et al. Observational evidence from supernovae for an accelerating universe and a cosmological constant. *Astron. J.*, 116:1009–1038, 1998.

[2] S. Perlmutter et al. Measurements of omega and lambda from 42 high-redshift supernovae. *Astrophys. J.*, 517:565–586, 1999.

[3] W. L. Freedman et al. Final results from the hubble space telescope key project to measure the hubble constant. *Astrophys. J.*, 553:47–72, 2001.

[4] S. W. Allen, R. W. Schmidt, and A. C. Fabian. Cosmological constraints from the x-ray gas mass fraction in relaxed lensing clusters observed with chandra. *Mon. Not. Roy. Astron. Soc.*, 334:L11, 2002.

[5] Max Tegmark et al. Cosmological parameters from sdss and wmap. *Phys. Rev.*, D69:103501, 2004.

[6] Adam G. Riess et al. Type Ia Supernova Discoveries at $z > 1$ From the Hubble Space Telescope: Evidence for Past Deceleration and Constraints on Dark Energy Evolution. *Astrophys. J.*, 607:665–687, 2004.

[7] Shaun Cole et al. The 2dF Galaxy Redshift Survey: Power-spectrum analysis of the final dataset and cosmological implications. *Mon. Not. Roy. Astron. Soc.*, 362:505–534, 2005.

[8] Daniel J. Eisenstein et al. Detection of the baryon acoustic peak in the large-scale correlation function of sdss luminous red galaxies. *Astrophys. J.*, 633:560–574, 2005.

[9] Pierre Astier et al. SNLS. *Astron. Astrophys.*, 447:31–48, 2006.

[10] D. N. Spergel et al. Wilkinson microwave anisotropy probe (wmap) three year results: Implications for cosmology. *Astrophys. J. Suppl.*, 170:377, 2007.

[11] Will J. Percival et al. Measuring the Baryon Acoustic Oscillation scale using the SDSS and 2dFGRS. *Mon. Not. Roy. Astron. Soc.*, 381:1053–1066, 2007.

[12] S. W. Allen et al. Improved constraints on dark energy from Chandra X-ray observations of the largest relaxed galaxy clusters. *arXiv:0706.0033 [astro-ph]*, 2007.

[13] A. Mantz, S. W. Allen, H. Ebeling, and D. Rapetti. New constraints on dark energy from the observed growth of the most X-ray luminous galaxy clusters. *arXiv:0709.4294 [astro-ph]*, 2007.

[14] E. Komatsu et al. Five-Year Wilkinson Microwave Anisotropy Probe (WMAP) Observations:Cosmological Interpretation. *arXiv:0803.0547 [astro-ph]*, 2008.

[15] Clifford M. Will. The confrontation between general relativity and experiment. *Living Reviews in Relativity*, 4(4), 2001.

[16] Planck-Collaboration. Planck: The scientific programme. *astro-ph/0604069*, 2006.

[17] David Rapetti, Steven W. Allen, Mustafa A. Amin, and Roger D. Blandford. A kinematical approach to dark energy studies. *Mon. Not. Roy. Astron. Soc.*, 375:1510–1520, 2007.

[18] Sean M. Carroll. The cosmological constant. *Living Rev. Rel.*, 4:1, 2001.

[19] Bharat Ratra and P. J. E. Peebles. Cosmological consequences of a rolling homogeneous scalar field. *Phys. Rev.*, D37:3406, 1988.

[20] Christian Armendariz-Picon. Could dark energy be vector-like? *JCAP*, 0407:007, 2004.

[21] Glennys R. Farrar and P. James E. Peebles. Interacting dark matter and dark energy. *Astrophys. J.*, 604:1–11, 2004.

[22] Sean M. Carroll, Vikram Duvvuri, Mark Trodden, and Michael S. Turner. Is cosmic speed-up due to new gravitational physics? *Phys. Rev.*, D70:043528, 2004.

[23] David I. Santiago, Dimitri Kalligas, and Robert V. Wagoner. Scalar-tensor cosmologies and their late time evolution. *Phys. Rev.*, D58:124005, 1998.

[24] Francesca Perrotta, Carlo Baccigalupi, and Sabino Matarrese. Extended quintessence. *Phys. Rev.*, D61:023507, 2000.

[25] Arthur Lue, Roman Scoccimarro, and Glenn Starkman. Differentiating between modified gravity and dark energy. *Phys. Rev.*, D69:044005, 2004.

[26] Mustapha Ishak, Amol Upadhye, and David N. Spergel. Probing cosmic acceleration beyond the equation of state: Distinguishing between dark energy and modified gravity models. *Phys. Rev.*, D74:043513, 2006.

[27] Sidney Bludman. Cosmological acceleration: Dark energy or modified gravity? *astro-ph/0605198*, 2006.

[28] Pengjie Zhang, Rachel Bean, and Scott Dodelson. A discriminating probe of gravity at cosmological scales. *arXiv:0704.1932 [astro-ph]*, 2007.

[29] Dragan Huterer and Eric V. Linder. Separating dark physics from physical darkness: Minimalist modified gravity vs. dark energy. *Phys. Rev.*, D75:023519, 2007.

[30] Shinji Tsujikawa. Matter density perturbations and effective gravitational constant in modified gravity models of dark energy. *arXiv:0705.1032 [astro-ph]*, 2007.

[31] Eric V. Linder and Robert N. Cahn. Parameterized beyond-einstein growth. *astro-ph/0701317*, 2007.

[32] Robert Caldwell, Asantha Cooray, and Alessandro Melchiorri. Constraints on a new post-general relativity cosmological parameter. *astro-ph/0703375*, 2007.

[33] Edmund Bertschinger. On the growth of perturbations as a test of dark energy. *Astrophys. J.*, 648:797–806, 2006.

[34] Luca Amendola, Martin Kunz, and Domenico Sapone. Measuring the dark side (with weak lensing). *arXiv:0704.2421 [astro-ph]*, 2007.

[35] Wayne Hu and Daniel J. Eisenstein. The structure of structure formation theories. *Phys. Rev.*, D59:083509, 1999.

[36] Sergei Bashinsky. Mapping cosmological observables to the dark kinetics. *arXiv:0707.0692 [astro-ph]*, 2007.

[37] Wayne Hu and Ignacy Sawicki. A parameterized post-friedmann framework for modified gravity. *arXiv:0708.1190 [astro-ph]*, 2007.

[38] Bhuvnesh Jain and Pengjie Zhang. Observational Tests of Modified Gravity. *arXiv:0709.2375 [astro-ph]*, 2007.

[39] Lam Hui and Kyle P. Parfrey. The Evolution of Bias - Generalized. *arXiv:0712.1162 [astro-ph]*, 2007.

[40] Edmund Bertschinger and Phillip Zukin. Distinguishing Modified Gravity from Dark Energy. *arXiv:0801.2431 [astro-ph]*, 2008.

[41] G. R. Dvali, Gregory Gabadadze, and Massimo Porrati. 4d gravity on a brane in 5d minkowski space. *Phys. Lett.*, B485:208–214, 2000.

[42] James M. Bardeen. Gauge invariant cosmological perturbations. *Phys. Rev.*, D22:1882–1905, 1980.

[43] C. Armendariz-Picon, Viatcheslav F. Mukhanov, and Paul J. Steinhardt. A dynamical solution to the problem of a small cosmological constant and late-time cosmic acceleration. *Phys. Rev. Lett.*, 85:4438–4441, 2000.

[44] Levon Pogosian and Alessandra Silvestri. The pattern of growth in viable f(R) cosmologies. *Phys. Rev.*, D77:023503, 2008.

[45] B. Boisseau, G. Esposito-Farese, D. Polarski, and Alexei A. Starobinsky. Reconstruction of a scalar-tensor theory of gravity in an accelerating universe. *Phys. Rev. Lett.*, 85:2236, 2000.

[46] Carlo Schimd, Jean-Philippe Uzan, and Alain Riazuelo. Weak lensing in scalar-tensor theories of gravity. *Phys. Rev.*, D71:083512, 2005.

[47] Rachel Bean. Perturbation evolution with a non-minimally coupled scalar field. *Phys. Rev.*, D64:123516, 2001.

[48] Shin'ichi Nojiri and Sergei D. Odintsov. Introduction to modified gravity and gravitational alternative for dark energy. *Int. J. Geom. Meth. Mod. Phys.*, 4:115–146, 2007.

[49] Yong-Seon Song, Wayne Hu, and Ignacy Sawicki. The large scale structure of f(r) gravity. *Phys. Rev.*, D75:044004, 2007.

[50] Thomas Faulkner, Max Tegmark, Emory F. Bunn, and Yi Mao. Constraining f(r) gravity as a scalar tensor theory. *astro-ph/0612569*, 2006.

[51] Rachel Bean, David Bernat, Levon Pogosian, Alessandra Silvestri, and Mark Trodden. Dynamics of linear perturbations in f(r) gravity. *Phys. Rev.*, D75:064020, 2007.

[52] Takeshi Chiba, Tristan L. Smith, and Adrienne L. Erickcek. Solar system constraints to general f(r) gravity. *Phys. Rev.*, D75:124014, 2007.

[53] Andrei V. Frolov. A Singularity Problem with f(R) Dark Energy. *arXiv:0803.2500 [astro-ph]*, 2008.

[54] Cedric Deffayet. On brane world cosmological perturbations. *Phys. Rev.*, D66:103504, 2002.

[55] Yong-Seon Song, Ignacy Sawicki, and Wayne Hu. Large-scale tests of the DGP model. *Phys. Rev.*, D75:064003, 2007.

[56] Cedric Deffayet, G. R. Dvali, Gregory Gabadadze, and Arkady I. Vainshtein. Nonperturbative continuity in graviton mass versus perturbative discontinuity. *Phys. Rev.*, D65:044026, 2002.

[57] Markus A. Luty, Massimo Porrati, and Riccardo Rattazzi. Strong interactions and stability in the DGP model. *JHEP*, 09:029, 2003.

[58] Christos Charmousis, Ruth Gregory, Nemanja Kaloper, and Antonio Padilla. DGP specteroscopy. *JHEP*, 10:066, 2006.

[59] Jacob D. Bekenstein. Relativistic gravitation theory for the mond paradigm. *Phys. Rev.*, D70:083509, 2004.

[60] Takeshi Chiba, Takahiro Okabe, and Masahide Yamaguchi. Kinetically driven quintessence. *Phys. Rev.*, D62:023511, 2000.

[61] Tomi Koivisto and David F. Mota. Dark energy anisotropic stress and large scale structure formation. *Phys. Rev.*, D73:083502, 2006.

[62] Edmund J. Copeland, M. Sami, and Shinji Tsujikawa. Dynamics of dark energy. *Int. J. Mod. Phys.*, D15:1753–1936, 2006.

[63] J. Anthony Tyson. Large synoptic survey telescope: Overview. *Proc. SPIE Int. Soc. Opt. Eng.*, 4836:10–20, 2002.

[64] Hu Zhan, Lloyd Knox, Anthony Tyson, and Vera Margoniner. Exploring large-scale structure with billions of galaxies. *Astrophys. J.*, 640:8–17, 2006.

[65] C. L. Reichardt et al. High resolution CMB power spectrum from the complete ACBAR data set. *arXiv:0801.1491 [astro-ph]*, 2008.

[66] Erminia Calabrese, Anze Slosar, Alessandro Melchiorri, George F. Smoot, and Oliver Zahn. Cosmic Microwave Weak lensing data as a test for the dark universe. *arXiv:0803.2309 [astro-ph]*, 2008.

[67] Yi Mao, Max Tegmark, Matthew McQuinn, Matias Zaldarriaga, and Oliver Zahn. How accurately can 21 cm tomography constrain cosmology? *arXiv:0802.1710 [astro-ph]*, 2008.

[68] R. E. Smith et al. Stable clustering, the halo model and nonlinear cosmological power spectra. *Mon. Not. Roy. Astron. Soc.*, 341:1311, 2003.

[69] Lisa Randall and Raman Sundrum. An alternative to compactification. *Phys. Rev. Lett.*, 83:4690–4693, 1999.

[70] Kazuya Koyama and Fabio P. Silva. Non-linear interactions in a cosmological background in the DGP braneworld. *Phys. Rev.*, D75:084040, 2007.

[71] Shinji Mukohyama. Gauge-invariant gravitational perturbations of maximally symmetric spacetimes. *Phys. Rev.*, D62:084015, 2000.

Chapter 4

Relativistic dark matter at the Galactic center

Mustafa A. Amin and Tommer Wizansky

Department of Physics, Stanford University, CA 94305, USA

accepted for publication in Phys. Rev. D. [arXiv:0706.3201 [hep-th]].

Abstract In a large region of the supersymmetry parameter space, the annihilation cross section for neutralino dark matter is strongly dependent on the relative velocity of the incoming particles. We explore the consequences of this velocity dependence in the context of indirect detection of dark matter from the Galactic center. We find that the increase in the annihilation cross section at high velocities leads to a flattening of the halo density profile near the Galactic center and an enhancement of the annihilation signal. For the models considered, the annihilation signal can be doubled. These models are typically undetectable by current experiments in spite of the enhancement.

4.1 Introduction

Indirect detection is one of the most promising avenues for the discovery of dark matter through its non-gravitational effects. Many efforts are underway and more are planned to detect the products of dark matter annihilations [1, 2, 3, 4, 5, 6, 7, 8, 9, 10]. The best places to look for the annihilation signal are regions where the density of dark matter is expected to be high, for example, centers of dark matter halos [11], center of stars [12, 13] and neighborhoods of compact objects [14].

We concentrate on the sub-parsec region around the super-massive black hole (SBH) at center of our galaxy ($M_{\rm bh} \approx 4 \times 10^6 M_\odot$ [15, 16]). Gondolo and Silk [17] argued that a sharp dark matter spike should form around the SBH leading to a large enhancement of the annihilation signal. Subsequent authors (for example [18, 19, 20, 21]) qualified this statement, pointing out several phenomena which would have the effect of smoothing and reducing the spike. The debate over the existence of a dark matter spike at the center of the galaxy has yet to be resolved. For the purpose of this paper, we assume that a spike does exist.

In this study we discuss a new correction to the predictions for the annihilation rate and halo profile around the SBH. We point out that near the black hole the dark matter particles will be moving sub-relativistically ($v/c \lesssim 0.2$). This is in contrast to the usual assumption whereby the dark matter is taken to be cold and slow. In fact, most previous calculations (see for example [17]) have been performed in the limit $(v/c) \rightarrow 0$ where v is the relative velocity between particles. For a certain class of supersymmetric dark matter models, the cross section for annihilation can be enhanced by several orders of magnitude in the vicinity of the SBH due a strong dependence on v. In the presence of a central dark matter spike this can produce a measurable correction to the observed annihilation signal. In addition, the enhanced cross section leads to depletion of the spike and a widening of the "annihilation core". We explore these two effects for a variety of halo profiles to account for the many astrophysical uncertainties regarding the nature of the density profile.

We find that the enhancements in the annihilation signals occur primarily in models for which the indirect detection signals are too small to be seen by current experiments. However, these models are quite plausible theoretically and are even preferred by some criteria. We can easily imagine a scenario in which particle physics experiments point to one of these theories as a correct description of nature. This will motivate dedicated gamma ray observations concentrating on objects where dark matter is likely to be concentrated. We will argue that, in this situation, the velocity-dependent enhancement of the annihilation cross section must be taken into account.

The rest of the paper is organized as follows. In Section 4.2 we give a brief review of supersymmetric dark matter and enumerate the circumstances whereby a strong enhancement to the annihilation cross section may arise. In Section 4.3 we estimate the corrections to the halo profile arising from the enhanced annihilation rate and calculate corrections to the annihilation signal. Our conclusions are presented in Section 4.4.

4.2 Supersymmetric dark matter

For the purpose of this study we restrict ourselves to the minimal supersymmetric standard model (MSSM). In this class of theories there exist four neutral fermionic mass eigenstates – the neutralinos. The lightest of these is often the lightest superpartner in the theory (LSP) and provides a good dark matter candidate. We are interested in describing the conditions under which the annihilation of the LSP to standard model particles exhibits a strong velocity dependence leading to an enhancement of the indirect detection signal.

A sample of the most important Feynman diagrams contributing to neutralino annihilations are depicted in Figure 4.1. First, a pair of neutralinos may exchange a fermion superpartner (sfermion), producing two standard model fermions. Fermions may also be produced through an s-channel exchange of a heavy scalar, in this case the A^0 Higgs boson. Notably, this diagram does not admit a p-wave component, a fact which will be important in the coming analysis. Finally, the neutralinos may annihilate to standard model gauge bosons. In Figure 4.1 we present the annihilation to two Z^0 bosons via the exchange of a heavier neutralino.

In the MSSM, neutralinos are Majorana particles. This leads to a well-known

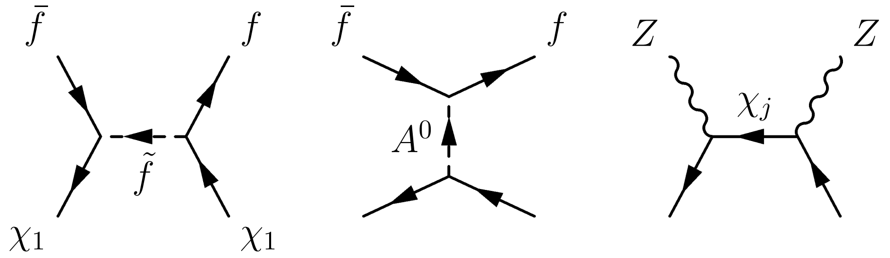

Figure 4.1: A typical set of Feynman diagrams contributing to the self annihilations of a neutralino into Standard Model particles. The LSP is denoted by χ_1, χ_j is a heavier neutralino and A^0 is the neutral CP-odd Higgs boson.

helicity suppression of the amplitude for pair annihilation into light fermions [22]. If χ denotes the dark matter particle and f the fermion, the s-wave cross section will be suppressed by a factor of

$$z^2 = m_f^2/m_\chi^2 \ .$$

For the annihilation of a 200 GeV neutralino to Standard Model leptons, z^2 is less than 10^{-4}. Consequently, the p-wave annihiliation, which is suppressed only by v^2/c^2, may dominate. We can therefore conclude that for models where the LSP annihilates primarily to fermions, the annihilation cross section will exhibit a strong velocity dependence. It is this effect which lies at the core of our present work. In the next few paragraphs, we review how these helicity-suppressed cross sections arise in the MSSM parameter space. A more complete description can be found, for example, in [23]. For an excellent review of the MSSM and supersymmetry in general see [24].

As mentioned, only annihilations to fermions undergo helicity suppression. We would like to identify the regions of parameter space for which the dominant annihilation channels do undergo helicity suppression and the resulting process is p-wave. It is this class of models which will exhibit a strong velocity dependence.

In the MSSM, each neutralino is a linear combination of the superpartners of two neutral gauge bosons and two neutral Higgs bosons. It is typically parametrized by

$$\chi_i = Z_{i1}\tilde{B}^0 + Z_{i2}\tilde{W}^0 + Z_{i3}\tilde{H}_1^0 + Z_{i4}\tilde{H}_2^0,$$

where χ_i is the i^{th} neutralino and tildes denote superpartners. The partners of the

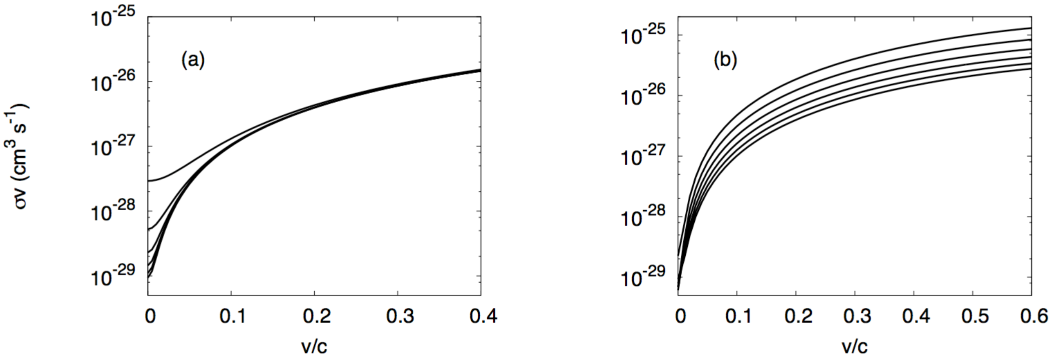

Figure 4.2: σv as a function of (v/c) for sample models from the $\tilde{\tau}$ coannihilation region. In (a) m_A is scanned, increasing from top to bottom, and in (b) $m_{\tilde{\tau}}$ is scanned, increasing from top to bottom.

B^0, W^0 and Higgs bosons are usually called wino, bino and Higgsino respectively. Of these four only the bino is a gauge singlet, meaning that it does not interact with gauge bosons. Thus, by making Z_{11} large compared to the other components, we can eliminate the third diagram in Figure 4.1, leaving only fermionic processes. The annihilation of Majorana particles through a scalar coupling can only take place in the s-wave. Thus, if the second diagram were to dominate over the first, the cross section would indeed be helicity suppressed but no strong velocity dependence would arise. To suppress this diagram we demand that the A^0 boson is significantly heavier than the fermion superpartners. We must also make sure that no resonance enhances the A^0 diagram, that is, m_A cannot be too close to $2m_\chi$.

We may now ask how generic are these constraints? The condition of large Z_{11} is quite generic. The theoretically compelling assumption of gauge unification naturally leads to a bino that is lighter than the wino by a factor of two [25]. In many classes of models, for example, minimal supergravity, the condition of electroweak symmetry breaking requires that the higgsinos are quite heavy. In these cases the LSP is mostly bino. The mass of the A^0 boson is, in principal, unconstrained and can easily be large enough to suppress the A^0 exchange diagram.

Thus, helicity-suppressed dark matter annihilation is quite likely in models of supersymmetry. This implies a strong dependence of the annihilation rate on the relative velocity of the incoming particles. In the following, we will consider sample MSSM models from this region of parameter space. We will choose models for which the predicted dark matter relic density agrees with value $\Omega_\chi h^2 \approx 0.1$ given by the WMAP experiment [26]. All cross sections and relic density calculations were performed using the DarkSUSY software package [27].

In Figure 4.2, we show the annihilation cross section times the velocity for the dark matter particle in several of these models. The strong velocity dependence is evident, enhancing the total cross section by several orders of magnitude over the value at $v = 0$. We show how the low and high velocity behaviors of the cross section can be tuned independently by varying different supersymmetric parameters. In Figure 4.2 (a) the mass of the the A^0 is scanned. As it is decreased the s-channel diagram in Figure 4.1 becomes increasingly important, the s-wave component of the amplitude increases, and the $v = 0$ cross section grows. In 4.2 (b) the mass of the stau is scanned. As this parameter is decreased the t-channel scalar exchange diagram is enhanced and the p-wave, velocity dependent, component of the cross section grows. Notably, we must vary the mass of the LSP along with the stau mass in order to maintain the correct relic abundance.

The curves in Figure 4.2 can be well fit by expressions of the form

$$\sigma v \approx (\sigma v)_0 + (\sigma v)_1 (v/c)^2 \tag{4.1}$$

where $(\sigma v)_0$ and $(\sigma v)_1$ are fit parameters. We use this approximation in the following sections.

4.3 Astrophysics

In the previous section we introduced a class of SUSY models for which the neutralino annihilation cross section shows a strong velocity dependence. In this section we explore the consequences for the density profile and the expected annihilation signal from the dark matter in the sub-parsec region around our Galactic center. To the best of our knowledge, this effect has been ignored in the literature. We find that neglecting this velocity dependence leads to an underestimation of the size of the annihilation core as well as the expected annihilation signal. In addition, we find that these corrections depend strongly on the density profile of the halo.

4.3.1 Density profile

The annihilation signal depends on the the density profile of dark matter. In particular, it is sensitive to the profile in the sub-parsec region around the central black hole where the density is expected to be quite high. Our first goal is to understand how the density profile changes in this region when we include the velocity dependence of the cross section.

The density profile depends on a number of physical processes such as the initial phase space distribution of the dark matter particles that collapsed to form the halo, the steepening of the profile due to the baryons, scattering by stars, loss to the central black hole, black hole or galactic merger history etc. A detailed calculation of the density profile is beyond the scope of this paper (see [28] for an excellent review). Following [29], we take the dark matter density profile to be given by

$$\rho(r) = \begin{cases} \rho(r_c) & 10r_g < r \leq r_c \\ \rho_0\,(r/r_\mathrm{b})^{-\gamma_\mathrm{sp}} & r_c < r \leq r_\mathrm{b}\ , \\ \rho_0\,(r/r_\mathrm{b})^{-\gamma_c} & r_\mathrm{b} < r\ , \end{cases} \tag{4.2}$$

In the above expression $r_g \approx 4 \times 10^{-7}\,\mathrm{pc}$ [15] is the Scwarzchild radius of the central black hole, r_b is the size of the spike, γ_c is the slope of the halo and γ_{sp} is the spike slope. r_c is the size of the annihilation core which will be discussed below.

The spike slope is related to γ_c and given by

$$\gamma_{sp} = 2 + 1/(4 - \gamma_c) \tag{4.3}$$

(see for example [17]). Due to the interactions of dark matter with baryons and scattering off stars, the size of the spike decreases with time. We follow the perscription given by [29] and set

$$r_b(\tau) = 0.2\, r_{\rm bh} \times \exp\left[-\frac{\tau}{2(\gamma_{\rm sp} - \gamma_{\rm c})}\right]$$

where $r_{\rm bh}$ is the radius of gravitational influence of the SBH and τ is the time since the formation of the black hole in units of the heating time $t_{\rm heat} \approx 10^9\,{\rm yrs}$ [30, 28]. In the following we take $\tau \approx 10$ [20]. It is important to note that the relation (4.3) also breaks down with time [20]. However, for short enough formation times it is approximately valid and for simplicity we continue using it throughout this paper.

For $r < 10r_g$ the density of dark matter particles decreases rapidly and vanishes at $r = 4r_g$ [17]. We set the normalization of the density profile, ρ_0, by extrapolating inwards from the solar radius:

$$\rho_0 = \rho_\odot \left(\frac{r_\odot}{r_b}\right)^{\gamma_c}.$$

The density at the solar radius $\rho_\odot = 0.3{\rm GeV/cm}^3$.

We now turn to the *core radius* r_c. As discussed above, the density profile is determined by self annihilation, scattering by stars, loss to the SBH etc. If the density gets too high, annihilation becomes efficient enough to prevent further rise in the density. This results in the formation of a flattened core near the galactic center. The radius at which the core starts forming is determined by

$$\Gamma_{\rm ann}(r_c) \approx (\tau\, t_{\rm heat})^{-1} \tag{4.4}$$

The annihilation rate $\Gamma_{\rm ann}(r) = \rho(r)\sigma v(r)/m$ where m is the mass of the dark matter particle. The position dependence of σv arises due to its velocity dependence. For a virialized halo, $(v/c)^2 \approx r_g/2r)$. Since the dark matter density is significant for $r > 10r_g$, the relavent velocities are bounded by $(v/c)^2 \lesssim 0.05$.

We consider a model taken from the stau coannihilation region of mSugra. The mass of the LSP $m = 166\,{\rm GeV}$ and the mass of the lightest stau is $173\,{\rm GeV}$. The relic density is $\Omega_{\rm dm}h^2 \approx 0.1$. In this model, $(\sigma v)_0 = 9 \times 10^{-30}\,{\rm cm^3s^{-1}}$ and $(\sigma v)_1 = 8.9 \times 10^{-26}\,{\rm cm^3s^{-1}}$ (see equation (4.1)). We will refer to this model as our fiducial

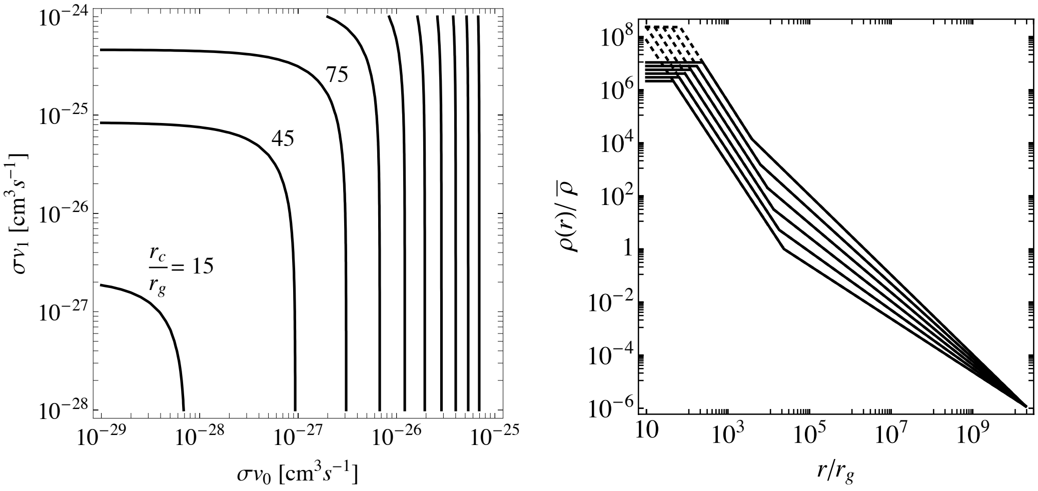

Figure 4.3: (a) The variation of the core radius with $(\sigma v)_0$ and $(\sigma v)_1$. Ignoring the $(\sigma v)_1$ leads to an underestimate of the core radius. (b) Spike profile for $\gamma_c = 1 - 1.5$, increasing from bottom to top. Note that for large values of $\gamma_{\rm sp}$, the radius of the annihilation core is also large. The dotted lines indicate the density profile when we set $(\sigma v)_1 = 0$.

model. Whenever a parameter is not explicitly defined or varied, its value is taken from this model.

For our fiducial model with $\gamma_c = 1$ (NFW profile), the core radius $r_c \approx 46 r_g$, with a core density of $\rho(r_c) \approx 2 \times 10^6\, \bar{\rho}$ where $\bar{\rho} = 6733\, \mathrm{M}_\odot\, \mathrm{pc}^{-3}$. If we ignore the velocity dependence, then we do not get a core. In Figure 4.3(a) we plot r_c for different $(\sigma v)_0$ and $(\sigma v)_1$ for the same density profile. We note that the size of the core is not independent of $(\sigma v)_1$ and ignoring it leads to an underestimation of the core size. If $(\sigma v)_1$ has a dominant contribution in determining the core radius r_c, it has to be significantly larger than $(\sigma v)_0$. This is because the factor $(v/c)^2 \approx r_g/2r$ in front of $(\sigma v)_1$ is small unless we are close to the central black hole.

Another important factor that determines the size and density of the core is the steepness of the density profile parametrized by γ_c. For the fiducial model, the size of the core as well as the density increases with increasing γ_c as shown in Figure 4.3(b). The dotted lines represent the density profiles for $(\sigma v)_1 = 0$.

4.3.2 Annihilation flux

The flux of photons (as observed by us) can be written as

$$\Phi = \frac{1}{2m^2} \int d^3\mathbf{r} \frac{N\sigma v(\mathbf{r})\rho^2(\mathbf{r})}{4\pi|\mathbf{d}+\mathbf{r}|^2} \tag{4.5}$$

where $\rho(\mathbf{r})$ is the dark matter density and $\sigma v(\mathbf{r})$ is the annihilation cross section times the typical relative velocity of the annihilating particles. In the above expression $\mathbf{d}$ is the vector joining the sun and the galactic center, m is the mass of the annihilating dark matter particles and N is the number of photons (above the detector thresh-hold) produced in the annihilation process. The integral is done over a solid angle which depends on the angular resolution of the detector. We take this to be $\Delta\Omega \approx 10^{-5}$sr which is the approximate angular resolution for GLAST. We remind the reader that the position dependence of $N\sigma v(\mathbf{r})$ arises from the position dependence of the velocity in a virialized halo. Due to this position dependence of the cross section, we cannot simply separate the particle physics and astrophysics aspects of the integral as is commonly done in the literature.

The annihilation signal depends on the cross section in two ways: Explicitly through $N\sigma v$ appearing in equation (4.5) and implicity through ρ which depends on σv as discussed in the Section 4.3.1.

For the fiducial model with $\gamma_c = 1$, the expected flux is enhanced by a factor of ~ 2 compared to the case when the velocity dependence is ignored. One should view this number with caution, since it does depend strongly on the parameters of the model.

In Figure 4.4(a), we plot the annihilation flux as a function of $(\sigma v)_0$ and $(\sigma v)_1$ with the same halo profile. In Figure 4.4(b) we plot the ratio of the fluxes, with and without the velocity dependence in the cross section : Φ/Φ_0 where '0' indicates that we set $(\sigma v)_1 = 0$. As expected, ignoring the velocity dependence of the cross section leads to an underestimation of the flux. The enhancement is large when $(\sigma v)_1/(\sigma v)_0$ is large.

Next, in Figure 4.5 we show the flux and enhancement as a function of γ_c. As seen in Figure 3(b), the core size increased with γ_c. Thus, the fraction of particles moving

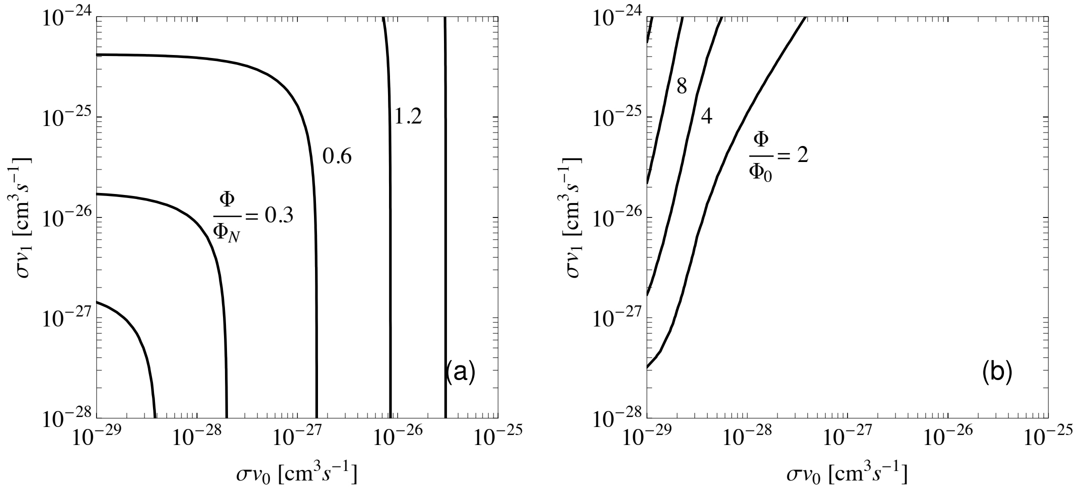

Figure 4.4: (a) The annihilation flux as a function of $(\sigma v)_0$ and $(\sigma v)_1$. $\Phi_N = 6 \times 10^{-10}\mathrm{cm}^{-2}\mathrm{s}^{-1}$ which is the (approximate) sensitivity of GLAST at an energy threshold of 1 GeV. (b) The ratio of annihilation fluxes Φ/Φ_0 where '0' refers to the flux calculated by setting $(\sigma v)_1 = 0$.

at relativistic velocities decreases and the enhancement to the signal is weakened.

We note that the enhancement of the signal occurs in models that are not detectable by current or planned experiments. For our fiducial model, the flux is two orders of magnitude below GLAST sensitivity (see for example [31]). This is mainly due to the small $(\sigma v)_0$ since it is $(\sigma v)_0$ that determines the annihilation flux in regions with $r \gtrsim 10^4 r_g$. It is tempting to explore the SUSY parameter space with the aim of finding models with a large $(\sigma v)_0$ and $(\sigma v)_1/(\sigma v)_0$, so that the flux is large to begin with and the velocity dependent enhancement provides a further boost. However, relic dark matter abundance constrains $(\sigma v)_1 (v/c)^2 \lesssim 10^{-26}\mathrm{cm}^3\mathrm{s}^{-1}$. Thus, for $(\sigma v)_1/(\sigma v)_0 \gtrsim 10^4$, $(\sigma v)_0$ is typically small leading to a small overall flux.

4.4 Discussion

In this paper we have discussed the consequences of relativistic dark matter near the black hole at the center of our galaxy. We have argued that, in general, the commonly used approximation whereby the relative velocity of dark matter particles is taken

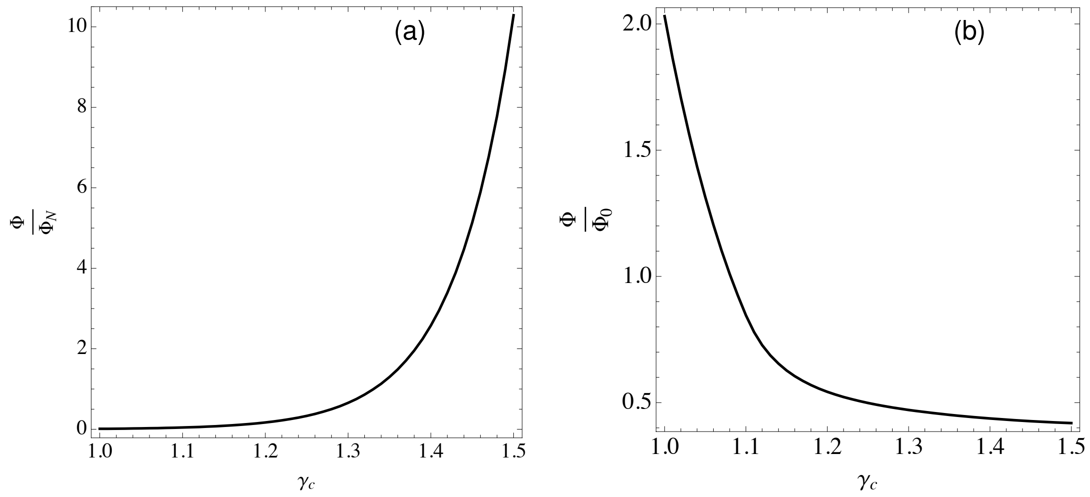

Figure 4.5: (a) Flux as a function of γ_c. $\Phi_N = 6 \times 10^{-10}\text{cm}^{-2}\text{s}^{-1}$ which is the (approximate) sensitivity of GLAST at an energy threshold of 1 GeV. (b) The ratio of the annihilation fluxes: Φ/Φ_0 as a function of γ_c. Φ_0 is the annihilation flux when we set $(\sigma v)_1 = 0$. As γ_c increases the core gets larger which results in a decrease in the relative fraction of of particles close to the galactic center. This in turn leads to a decrease in the enhancement

to vanish may be inapropriate. In regions very close to the black hole, the cold dark matter is no longer cold. If the dark matter has accumulated in a sharp spike around the black hole, this region may account for a large fraction of the expected signal. We presented a specific class of supersymmetric models in which the dark matter annihilation cross section is strongly dependent on the relative velocity of the incoming particles. In these theories, the expression for the annihilation flux no longer separates neatly into factors depending on the astrophysics and the particle physics. When the full velocity dependent cross section is considered, the annihilation flux receives up to an order of magnitude enhancement over the $v = 0$ value. In addition, we found that the enhanced cross section effects the halo profile close to the galactic center. The increased annihilations deplete the spike and widen the annihilation core.

We explored the change in the density profile and annihilation signal for annihilation cross sections of the form $\sigma v = (\sigma v)_0 + (\sigma v)_1 (v/c)^2$. We showed how the annihilation core size and the flux changed as a function of $(\sigma v)_0$ and $(\sigma v)_1$. To account for the astrophysical uncertainties in determining the dark matter density near the galactic centre, we presented our results for a variety of halo profiles.

None of the models we have considered are detectable by current or upcoming gamma ray observations. If the neutralino is the dominant component of dark matter and is produced thermally, the cross section at high velocity cannot be larger than about 10^{-26} cm^3/sec; otherwise the relic abundance would be too small. In most regions of the galaxy today, the neutralino velocity v/c would be very small, and the annihilation signal would be highly suppressed. However, if particle physics observations should indicate a scenario like those we have described, it would be worthwhile to mount dedicated gamma ray observations concentrating on the galactic center and the centers of nearby galaxies. Uniquely in those environments, in the neighborhood of the central black holes, the annihilation cross section would be enhance by the effect described in this paper.

Acknowledgments

We would like to acknowledge Roger Blandford, Robert Wagoner, Michael Peskin, Igor Moskalenko, Peter Michelson, Elliot Bloom, Edward Baltz and Teddy Cheung for illuminating discussions. MA is supported by a Stanford Graduate Fellowship. TW is supported by the US Department of Energy, contract DE–AC02–76SF00515.

Appendix

In this appendix we provide some analytic approximations to the flux integral, equation (4.5). We will assume that the velocity dependence of the cross section takes the form of equation (4.1), although this is not essential in the numerical calculations.

We split the flux integral into three parts; $\Phi = \Phi_{\rm core} + \Phi_{\rm spike} + \Phi_{\rm halo}$ bases on the density profile (4.2). In most cases, the largest contribution to the signal comes from the spike and core. However, the contribution from the halo is not always negligible. For example in the fiducial model, the spike, core and halo contribute $45, 54.5$ and 0.5

percent of the signal respectively for an angular resolution of $\Delta\Omega = 10^{-5}\text{sr}$, $\gamma_{\rm sp} = 7/3$ and $\gamma_c = 1$.

For the density profile, equation (4.2), we can calculate the core and spike parts of the integral analytically (since $r_c, r_{\rm bh} \ll d$). For the case when $\gamma_{\rm sp} \neq 3/2$ we have

$$
\begin{aligned}
\Phi_{\rm core} &\approx \frac{1}{6}\frac{(N\sigma v)_0}{d^2}\frac{\rho_c^2 r_c^3}{m^2}\left[1-\left(\frac{10r_g}{r_c}\right)^3\right]\left\{1+\frac{3}{4}\frac{(N\sigma v)_1}{(N\sigma v)_0}\frac{r_g}{r_c}\frac{\left[1-\left(\frac{10r_g}{r_c}\right)^2\right]}{\left[1-\left(\frac{10r_g}{r_c}\right)^3\right]}\right\} \\
\Phi_{\rm spike} &\approx \frac{1}{6-4\gamma_{\rm sp}}\frac{(N\sigma v)_0}{d^2}\frac{\rho_0^2 r_{\rm b}^3}{m^2}\left[1-\left(\frac{r_c}{r_{\rm b}}\right)^{3-2\gamma_{\rm sp}}\right]\times \\
&\qquad \left\{1+\frac{3-2\gamma_{\rm sp}}{4(1-\gamma_{\rm sp})}\frac{(N\sigma v)_1}{(N\sigma v)_0}\frac{r_g}{r_{\rm b}}\frac{\left[1-\left(\frac{r_c}{r_{\rm b}}\right)^{2(1-\gamma_{\rm sp})}\right]}{\left[1-\left(\frac{r_c}{r_{\rm b}}\right)^{3-2\gamma_{\rm sp}}\right]}\right\}
\end{aligned}
\tag{4.6}
$$

r_c and ρ_c depend on the cross section and $\gamma_{\rm sp}$.

Bibliography 4

[1] *http: // www-glast.stanford.edu/*, 2007.

[2] *http: // www.veritas.sao.arizona.edu/*, 2007.

[3] *http://www.mpi-hd.mpg.de/hfm/HESS/HESS.html/*, 2007.

[4] *http://wwwmagic.mppmu.mpg.de/*, 2007.

[5] *http://cossc.gsfc.nasa.gov/docs/cgro/cossc/egret/*, 2007.

[6] S. W. Barwick et al. The high-energy antimatter telescope (HEAT): An instrument for the study of cosmic ray positrons. *Nucl. Instrum. Meth.*, A400:34–52, 1997.

[7] *http://wizard.roma2.infn.it/pamela/*, 2007.

[8] *http://astrophysics.gsfc.nasa.gov/astroparticles/programs/bess/BESS.html*, 2007.

[9] *http://sci.esa.int/science-e/www/area/index.cfm?fareaid=21*, 2007.

[10] *http://agile.rm.iasf.cnr.it/publ02.html*, 2007.

[11] Piero Ullio, Lars Bergstrom, Joakim Edsjo, and Cedric G. Lacey. Cosmological dark matter annihilations into gamma-rays: A closer look. *Phys. Rev.*, D66:123502, 2002.

[12] P. Salati and J. Silk. A stellar probe of dark matter annihilation in galactic nuclei. *ApJ*, 338:24–31, March 1989.

[13] Igor V. Moskalenko and Lawrence L. Wai. Dark matter burners. *Astrophys. J.*, 659:L29–L32, 2007.

[14] Gianfranco Bertone and Malcolm Fairbairn. Compact Stars as Dark Matter Probes. *Phys. Rev.*, D77:043515, 2008.

[15] R. Genzel et al. The Stellar Cusp Around the Supermassive Black Hole in the Galactic Center. *Astrophys. J.*, 594:812–832, 2003.

[16] R. Schodel et al. Stellar dynamics in the central arcsecond of our galaxy. *Astrophys. J.*, 596:1015–1034, 2003.

[17] Paolo Gondolo and Joseph Silk. Dark matter annihilation at the galactic center. *Phys. Rev. Lett.*, 83:1719–1722, 1999.

[18] Piero Ullio, HongSheng Zhao, and Marc Kamionkowski. A Dark-Matter Spike at the Galactic Center? *Phys. Rev.*, D64:043504, 2001.

[19] David Merritt. Evolution of the Dark Matter Distribution at the Galactic Center. *Phys. Rev. Lett.*, 92:201304, 2004.

[20] Gianfranco Bertone and David Merritt. Time-dependent models for dark matter at the Galactic center. *Phys. Rev.*, D72:103502, 2005.

[21] David Merritt, Stefan Harfst, and Gianfranco Bertone. Collisionally Regenerated Dark Matter Structures in Galactic Nuclei. *Phys. Rev.*, D75:043517, 2007.

[22] H. Goldberg. Constraint on the photino mass from cosmology. *Phys. Rev. Lett.*, 50:1419, 1983.

[23] Kim Griest. Cross sections, relic abundance, and detection rates for neutralino dark matter. *Phys. Rev.*, D38:2357, 1988.

[24] Stephen P. Martin. A supersymmetry primer. 1997.

[25] Kenzo Inoue, Akira Kakuto, Hiromasa Komatsu, and Seiichiro Takeshita. Aspects of Grand Unified Models with Softly Broken Supersymmetry. *Prog. Theor. Phys.*, 68:927, 1982.

[26] D. N. Spergel et al. Wilkinson microwave anisotropy probe (wmap) three year results: Implications for cosmology. *Astrophys. J. Suppl.*, 170:377, 2007.

[27] P. Gondolo et al. DarkSUSY: Computing supersymmetric dark matter properties numerically. *JCAP*, 0407:008, 2004.

[28] Gianfranco Bertone and David Merritt. Dark matter dynamics and indirect detection. *Mod. Phys. Lett.*, A20:1021, 2005.

[29] Eun-Joo Ahn, Gianfranco Bertone, and David Merritt. Impact of astrophysical processes on the gamma-ray background from dark matter annihilations. *Phys. Rev.*, D76:023517, 2007.

[30] L. J. Spitzer and M. H. Hart. Random Gravitational Encounters and the Evolution of Spherical Systems. I. Method. *ApJ*, 164:399–+, March 1971.

[31] Gianfranco Bertone, Torsten Bringmann, Riccardo Rando, Giovanni Busetto, and Aldo Morselli. GLAST sensitivity to point sources of dark matter annihilation. 2006.

Chapter 5

Persistent geometric patterns in accretion discs

Mustafa A. Amin and Andrei V. Frolov

KIPAC/Department of Physics, Stanford University, CA 94305, USA

Mon. Not. Roy. Astron. Soc. Lett. 370 (2006) L42-L45 [arXiv:astro-ph/0603687].

Abstract We present a set of new characteristic frequencies associated with accretion disks around compact objects. These frequencies arise from persistent rotating patterns in the disk that are finite in radial extent and driven purely by the gravity of the central body. Their existence depends on general relativistic corrections to orbital motion and, if observed, could be used to probe the strong gravity region around a black hole. We also discuss a possible connection to the puzzle of quasi-periodic oscillations.

5.1 Introduction

Timing observations of accreting X-ray binary systems have revealed luminosity modulation at a number of characteristic frequencies. Phenomenology of these quasi-periodic oscillations (QPOs) is quite rich. For a detailed review, see [1] and references therein. Some of the features are rather puzzling, such as stability of high frequency QPOs in black hole binaries and that in some systems they appear in pairs at 3:2 frequency ratio.

QPOs in black hole systems are thought to arise from physical processes in accretion disks. Depending on where the oscillations reside, one can roughly divide models for QPOs in accretion disks into two classes: local and global. Local models tie down the oscillation frequency to a particular place in the disk (like an edge or a hot spot). In this case, the question of what determines that place has to be answered. One line of argument is that the location of the hot spot is determined by a resonance [2, 3, 4, 5]. This model has an attractive feature that the observed 3:2 frequency ratio can be explained by non-linear mode locking. A hot spot can give rise to luminosity variation, for example, due to Doppler beaming [6, 7]. However, a potential difficulty is to have a hot spot which is sufficiently bright. Achieving sufficient luminosity variation seems less problematic in global models, in which modes occupy a larger region of the disk. Linear perturbation analysis of the accretion disk in diskoseismology approach [8, 9, 10, 11] naturally solves the issue of spatial and frequency localization of modes. The 3:2 frequency ratio would be accidental for two fundamental diskoseismic modes, but it could arise from higher azimuthal g-modes which are nearly harmonic.

In this paper, we describe a set of new characteristic frequencies which might be present in accretion disks around compact objects. To the best of our knowledge, they have remained unnoticed in the literature. These frequencies arise from rotating patterns in the disk which are quasi-stationary, finite in radial extent, and driven purely by gravity of the central body. We neglect self-gravity and the hydrodynamics of the accreting matter. The main idea is similar to the notion of density waves that give rise to the spiral structure in galaxies [12, 13, 14], although these patterns depend on general relativity rather than a distributed matter source for their existence.

While it is tempting to identify the frequencies of these patterns with the source of QPOs, we cannot claim to have a complete model. The issues of how they are excited, how they translate to X-ray luminosity variation, and effects of pressure and viscosity need to be investigated in more detail. We will return to these points with some plausibility arguments in Section 5.4.

5.2 Accretion disk kinematics

A test particle in a circular equatorial orbit around a Kerr black hole has an orbital frequency [15]

$$\Omega = \frac{1}{r^{3/2} + a} \tag{5.1}$$

with respect to Boyer-Lindquist time t, where r is the orbit radius and a is the dimensionless black hole spin parameter ($a = cJ/GM^2$). We work in dimensionless units scaled by the black hole mass M (i.e., distances measured in units of GM/c^2, times measured in units of GM/c^3, etc.), and will further set $G = c = 1$. Here and later we will assume that particles co-rotate with the black hole.

If perturbed from the circular orbit, the particle will undergo radial and perpendicular oscillations with epicyclic frequencies κ and $\Omega_\perp$ respectively [16]

$$\kappa^2 = \Omega^2 \left(1 - \frac{6}{r} + \frac{8a}{r^{3/2}} - 3\,\frac{a^2}{r^2}\right) \tag{5.2}$$

and

$$\Omega_\perp^2 = \Omega^2 \left(1 - \frac{4a}{r^{3/2}} + 3\,\frac{a^2}{r^2}\right). \tag{5.3}$$

The factors multiplying Ω on the right-hand sides of these expressions are general relativistic corrections. They are absent in Keplerian mechanics, where both epicyclic and orbital frequencies are all the same ($\kappa = \Omega_\perp = \Omega$). The radial dependences of orbital frequency Ω and radial epicyclic frequency κ for a typical rotating black hole are illustrated in Figure 5.1. Circular orbits close to a black hole are unstable; the innermost stable circular orbit (ISCO) is located where κ^2 vanishes.

If orbital and epicyclic frequencies are the same, as they are for a Keplerian

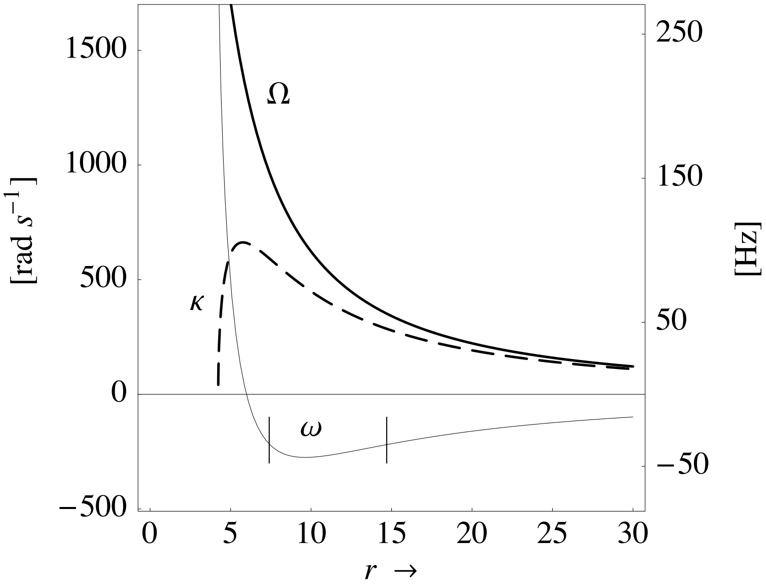

Figure 5.1: Orbital frequency Ω, radial epicyclic frequency κ, and precession frequency $\omega = \Omega - 2\kappa$ of a 2:1 orbit in an accretion disk around a Kerr black hole with $M = 10\,M_\odot$ and $a = 1/2$. Precession frequency exhibits a shallow negative minimum at $r_* \approx 9.64$. The radial extent of the rotating pattern with 20% deviation in frequency is marked by vertical bars.

potential, the orbits are closed. However, if the potential deviates from $1/r$ (either because of general relativity corrections, as in our case, or due to a distributed matter source, as happens in galaxies), the two frequencies will in general be different, and the orbits will precess. The condition for an orbit to close in a frame rotating with frequency ω is for the orbital and epicyclic frequencies to be commensurate, $m(\Omega - \omega) = n\kappa$, which gives the precession frequency

$$\omega = \Omega - \frac{n}{m}\,\kappa. \tag{5.4}$$

The integers n and m determine the shape of the precessing orbit, and from here on, we will use the abbreviation $n{:}m$ to refer to their values. Figure 5.2 shows the shape of 1:2 and 2:1 orbits, which are representative of the deformed and the self-intersecting orbit classes.

In general, precession frequency ω depends on r, and any pattern initially present

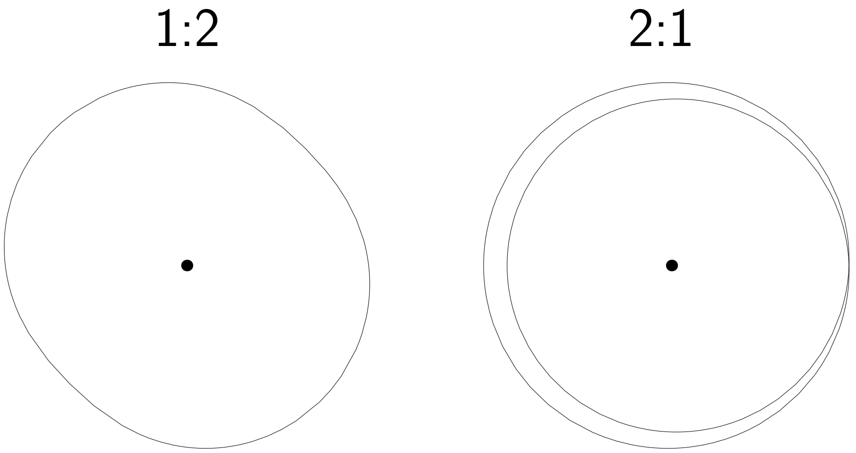

Figure 5.2: Sample closed orbits. 1:2 orbit (left) corresponds to 2 epicycles per 1 rotation around a central body, while 2:1 orbit (right) corresponds to 1 epicycle per 2 rotations.

will shear away as the disk rotates. However, if ω is approximately constant over some portion of the disk, collective orbit precession can lead to a nearly rigid pattern rotation. One example of this is the spiral structure in galaxies caused by the 1:2 mode [12, 13, 14]. The 1:1 mode in Keplerian disks gives rise to a static one-armed spiral pattern [17], which is seen in numerical simulations as well [18]. An attempt has been made to trap the 1:1 mode in the region of the strong gravity [19], but trapping depends strongly on the pressure distribution within the disk [20].

5.3 Persistent patterns in the disk

Our key observation is that for $n > m$, the precession frequency $\omega(r)$ develops a very shallow minimum at a radius $r = r_*$, as illustrated in Figure 5.1 for the 2:1 orbit. Collective excitation of particles on orbits precessing at the same rate would lead to a pattern occupying a sizable portion of the disk around r_* and rotating with little shear at a frequency $\omega_p = \omega(r_*)$. Somewhat unusual are the facts that the pattern is counter-rotating and that the orbit closes in several rotations rather than a single one.

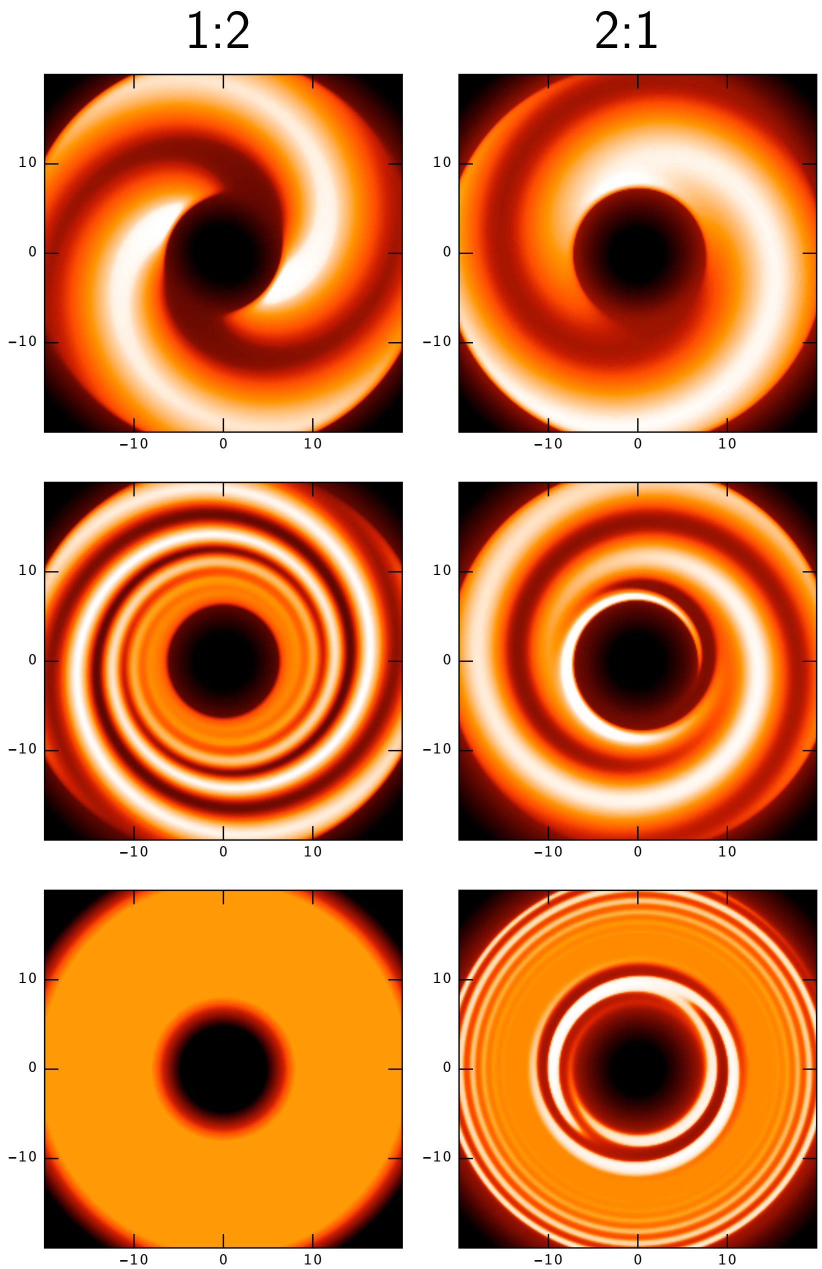

Figure 5.3: Evolution of density patterns obtained by distributing particles on stacked 1:2 (left) and 2:1 (right) orbits. Top row shows initial configuration, middle row - after one period of rotation of 2:1 pattern elapsed, bottom row - after twenty periods. Density contrast has been enhanced by histogram equalization.

In a real accretion disk, the collective particle motion would have to be excited by some dynamical mechanism. It might be complicated and could require numerical simulations of the disk to fully understand the driving process. In the present paper, we will be content with studying the kinematics only. We will set off a collective mode by selecting appropriate initial conditions (as described below) and follow the pattern evolution by tracing the motion of individual particles making up the disk. The purpose is to find out if there is a long-lived pattern that survives the differential rotation.

If perturbed from a circular orbit at $r = r_0$ by a small displacement ε in the radial direction, the trajectory of a test particle (to first order in ε) is

$$r(t) = r_0 + \varepsilon \sin(\kappa t + \chi), \tag{5.5}$$

$$\phi(t) = \varphi + \Omega t + \frac{2\Omega}{\kappa r}\,\Upsilon \varepsilon \cos(\kappa t + \chi), \tag{5.6}$$

where φ and χ are initial orbital and epicyclic phases, and

$$\Upsilon = \frac{1 - \frac{3}{r} + \frac{2a}{r^{3/2}}}{1 - \frac{2}{r} + \frac{a^2}{r^2}}\,\left(r^{3/2}\Omega\right) \tag{5.7}$$

is a relativistic correction factor (which, however, changes little in the region of the disk we are interested in). We populate the disk by spreading N particles uniformly on a $n{:}m$ orbit, with initial phases of a k^{th} particle

$$\varphi_k = \frac{2\pi n}{N}\,k, \quad \chi_k = \frac{2\pi m}{N}\,k, \tag{5.8}$$

while stacking the orbits in a radial direction at an angle α by giving the orbit located at r_j a phase offset

$$\varphi_{jk} = \varphi_k + \alpha r_j. \tag{5.9}$$

This particle distribution leads to a spiral structure in the disk. Figure 5.3 shows the surface density contrast (smoothed with a Gaussian kernel) for patterns obtained by distributing particles on stacked 1:2 (left) and 2:1 (right) orbits. The three rows of Figure 5.3 show a time-lapse sequence of pattern evolution. The top row shows the initial conditions, and the second and the third rows show patterns at $t = T_{2:1}$ and $t = 20\,T_{2:1}$ correspondingly. $T_{2:1} = 2\pi/\omega_{2:1}$ denotes a period of rotation of the 2:1 pattern.

The frequency of the 1:2 orbit precession depends monotonically on the radius, so one expects differential rotation to destroy the pattern. Indeed, at $t = T_{2:1}$, the spiral is seen to wind up, and by $t = 20\,T_{2:1}$, it is wound up so tightly that the smoothing removes all traces of structure. The evolution of the 2:1 pattern is markedly different. Signs of shear are clearly seen after a single rotation. However, even after twenty rotations, there is still a pattern present around $r_* \approx 9.6$ (which is exactly where the minimum of $\omega_{2:1}$ occurs). As this time span corresponds to almost 50 orbital rotations at r_*, the pattern is remarkably persistent.

5.4 Discussion

In the last section, we have shown that an accretion disk around a compact object can support persistent rotating patterns due to the collective excitations of particles in the disk. Their existence depends on general relativity effects and is sensitive to the parameters of the central body but not to the accretion rate. All the frequencies in the problem scale inversely proportionally to the central body mass. In addition, persistent pattern frequencies depend on the spin parameter. Figure 5.4 shows the rotation frequencies of the three lowest-order persistent patterns (2:1, 3:1, and 3:2) for a $10M_\odot$-mass black hole as the spin is varied. This dependence in principle could be used to measure the mass and spin of the central object, provided that the frequencies of two distinct modes are observed and identified correctly. One should note, though, that for multi-armed patterns (for example the 3:2 pattern which has two arms) modulation frequency could be a multiple of the rotation frequency.

Several different persistent patterns could coexist in the accretion disk; however, it is likely that the lowest-order ones are strongly selected based on geometrical considerations. Surface density modulation of the 2:1 pattern is second-order in particle displacement ε, while the 3:1 and 3:2 patterns are third-order. The cancellation of lower-order terms is directly caused by the multiple-fold geometry of the orbits with

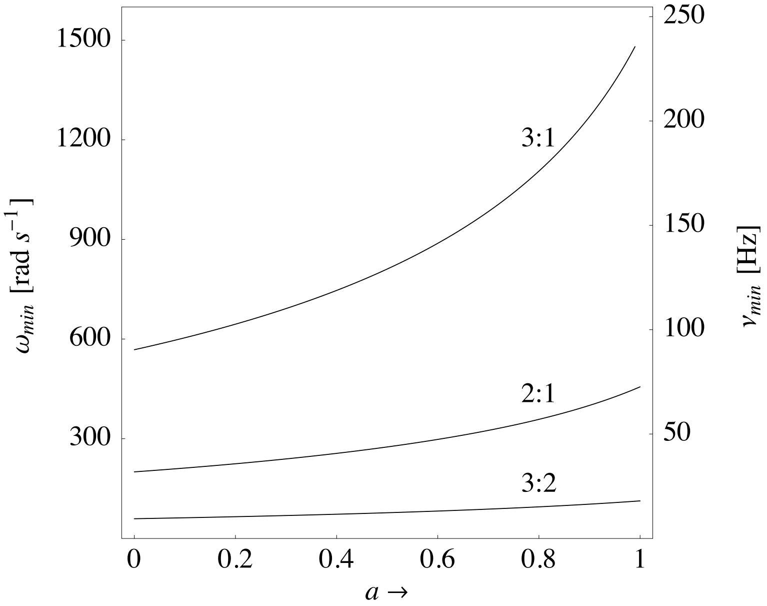

Figure 5.4: Persistent pattern frequencies of three lowest-order radial modes (2:1, 3:1, and 3:2) for a $10M_{\odot}$-mass black hole as a function of black hole spin parameter a.

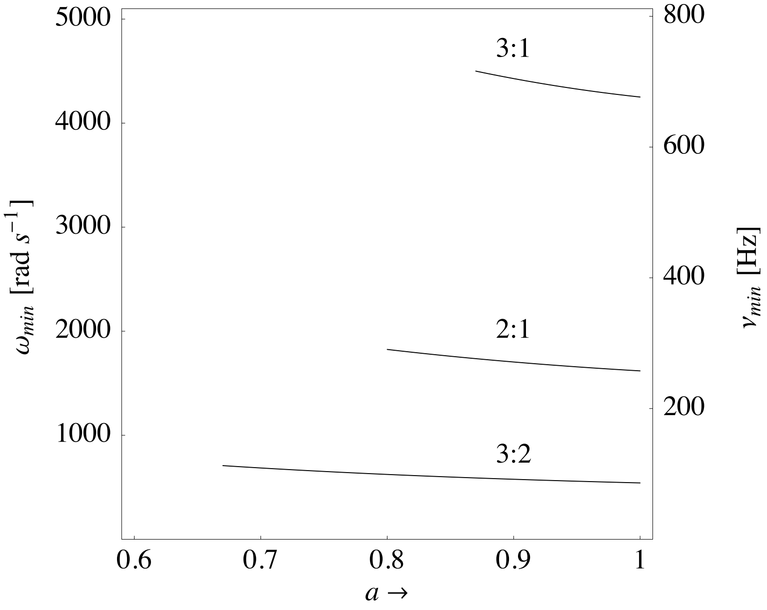

Figure 5.5: Persistent pattern frequencies of three lowest-order transverse modes (2:1, 3:1, and 3:2) for a $10M_{\odot}$-mass black hole as a function of black hole spin parameter a.

$n > 1$. Being higher-order could explain why these persistent patterns are not apparent in the linear perturbation analysis of [8]. Despite second-order scaling, the 2:1 pattern in Figure 5.3 (lower right) shows 1% amplitude of the surface density modulation for moderate displacement values ($\varepsilon/r_* \approx 0.022$). The radial extent of the 2:1 pattern ($\Delta r \sim 4$) also appears to be wider than that of a fundamental g-mode (the width of which is proportional to $c_s^{1/2}$ and is estimated as $\Delta r \sim 1$ by [8]).

In this paper, we focused on kinematics and neglected particle interactions and the hydrodynamics of the disk. The extent to which this approximation is justified should be further investigated. Of critical importance for the model is understanding the excitation mechanism. It is possible for the spiral waves to be driven from the outer edge of the disk [21, 22]; however, whether that is sufficient to cause persistent patterns to appear remains to be seen. Both questions could be answered by turning to numerical simulations of the accretion disk hydrodynamics. However, that is a much more complicated problem, and we feel that it is beyond the scope of this paper, the intent of which is merely to point out the existence of new characteristic frequencies in the disk.

It is plausible that the characteristic frequency of the collective motion will manifest itself in X-ray luminosity variation, but the exact mechanism responsible for the modulation is not clear to us. Density pattern in the accretion disk need not be a direct cause. Particles weaving in and out on self-intersecting orbits could lead to efficient gas heating, possibly due to shock formation, and create a temperature pattern in the accretion disk (in a sense, an extensive "hot spot"). The picture of temperature modulation of the disk causing X-ray luminosity variations is not entirely satisfactory as quasi-periodic oscillations are seen primarily in the hard non-thermal component of the emission [1]. That could indicate that the quasi-periodic emission is coming from a coronal region rather than from a disk [23]. It is possible that the transfer mechanism might involve a magnetic field threading the disk (Blandford, unpublished).

So far we have been talking about patterns arising from radial oscillations. It is worth mentioning that a similar thing could happen for transverse oscillations as well. The precession frequency $\omega_\perp = \Omega - \frac{n}{m}\Omega_\perp$ also has a minimum if $n > m$. However, the minimum lies inside an innermost stable circular orbit unless the black hole is spinning rapidly ($a > 0.8$ for 2:1 orbit). The frequencies of the three lowest-order transverse modes are shown in Figure 5.5. Transverse particle excitations would lead to a corrugated accretion disk rather than a surface density pattern.

To summarize, we have found a set of new characteristic frequencies associated with accretion disks around compact objects. Although many questions remain, it might be interesting to pursue this idea further and see if it could lead to a model of quasi-periodic oscillations in X-ray binaries. In particular, the numerical values of our characteristic frequencies and their independence of the accretion rate suggest an application to high-frequency QPOs in black hole binaries.

Acknowledgments

We would like to thank Andrei Beloborodov, Roger Blandford, Steven Fuerst, Wlodek Kluzniak, and Robert Wagoner for helpful discussions. AF is supported in part by the Stanford Institute for Theoretical Physics.

Bibliography 5

[1] J. E. McClintock and R. A. Remillard. Black Hole Binaries. *ArXiv Astrophysics e-prints*, June 2003.

[2] M. A. Abramowicz and W. Kluźniak. A precise determination of black hole spin in GRO J1655-40. *Astron. Astrophys.*, 374:L19–L20, August 2001.

[3] G. Török, M. A. Abramowicz, W. Kluźniak, and Z. Stuchlík. The orbital resonance model for twin peak kHz quasi periodic oscillations in microquasars. *Astron. Astrophys.*, 436:1–8, June 2005.

[4] W. Kluźniak. High frequency QPOs, nonlinear oscillations in strong gravity. *Astronomische Nachrichten*, 326:820–823, November 2005.

[5] M. A. Abramowicz. QPO as the Rosetta Stone for understanding black hole accretion. *Astronomische Nachrichten*, 326:782–786, November 2005.

[6] J. D. Schnittman and E. Bertschinger. The Harmonic Structure of High-Frequency Quasi-periodic Oscillations in Accreting Black Holes. *ApJ*, 606:1098–1111, May 2004.

[7] J. D. Schnittman. Interpreting the High-Frequency Quasi-periodic Oscillation Power Spectra of Accreting Black Holes. *ApJ*, 621:940–950, March 2005.

[8] R. V. Wagoner, A. S. Silbergleit, and M. Ortega-Rodríguez. "Stable" Quasi-periodic Oscillations and Black Hole Properties from Diskoseismology. *ApJ Lett.*, 559:L25–L28, September 2001.

[9] C. A. Perez, A. S. Silbergleit, R. V. Wagoner, and D. E. Lehr. Relativistic Diskoseismology. I. Analytical Results for "Gravity Modes". *ApJ*, 476:589–+, February 1997.

[10] A. S. Silbergleit, R. V. Wagoner, and M. Ortega-Rodríguez. Relativistic Diskoseismology. II. Analytical Results for C-modes. *ApJ*, 548:335–347, February 2001.

[11] M. Ortega-Rodríguez, A. S. Silbergleit, and R. V. Wagoner. Relativistic Diskoseismology. III. Low-Frequency Fundamental p-Modes. *ApJ*, 567:1043–1056, March 2002.

[12] B. Lindblad. On the possibility of a quasi-stationary spiral structure in galaxies. *Stockholms Observatoriums Annaler*, 5, 1963.

[13] C. C. Lin and F. H. Shu. On the Spiral Structure of Disk Galaxies. *ApJ*, 140:646–+, August 1964.

[14] C. C. Lin and F. H. Shu. On the Spiral Structure of Disk Galaxies, II. Outline of a Theory of Density Waves. *Proceedings of the National Academy of Science*, 55:229–234, February 1966.

[15] J. M. Bardeen, W. H. Press, and S. A. Teukolsky. Rotating Black Holes: Locally Nonrotating Frames, Energy Extraction, and Scalar Synchrotron Radiation. *ApJ*, 178:347–370, December 1972.

[16] A. T. Okazaki, S. Kato, and J. Fukue. Global trapped oscillations of relativistic accretion disks. *Publ. Astron. Soc. Japan*, 39:457–473, 1987.

[17] S. Kato. Low-frequency, one-armed oscillations of Keplerian gaseous disks. *Publ. Astron. Soc. Japan*, 35:249–261, 1983.

[18] K. Hayasaki and A. T. Okazaki. One-armed spiral structure of accretion discs induced by a phase-dependent mass transfer in Be/X-ray binaries. *MNRAS*, 360:L15–L19, June 2005.

[19] S. Kato. Trapped one-armed corrugation waves and QPOs. *Publ. Astron. Soc. Japan*, 42:99–113, February 1990.

[20] S. Kato and F. Honma. Trapping of one-armed corrugation waves revised. *Publ. Astron. Soc. Japan*, 43:95–111, February 1991.

[21] H. C. Spruit. Stationary shocks in accretion disks. *Astron. Astrophys.*, 184:173–184, October 1987.

[22] H. C. Spruit, T. Matsuda, M. Inoue, and K. Sawada. Spiral shocks and accretion in discs. *MNRAS*, 229:517–527, December 1987.

[23] L. Titarchuk and R. Fiorito. Spectral Index and Quasi-Periodic Oscillation Frequency Correlation in Black Hole Sources: Observational Evidence of Two Phases and Phase Transition in Black Holes. *ApJ*, 612:988–999, September 2004.